Karlsruhe Institute of Technology

Adsorption of gaseous tritium on gold coated beryllium investigated with TRIADE

Master's thesis
of

Manuel Klein

Institute of Experimental Nuclear Physics
at the Department of Physics
of the Karlsruhe Insitute of Technology (KIT)

Reviewer:	Prof. Dr. G. Drexlin
Second reviewer:	Prof. Dr. B. Holzapfel
Advisors:	Dr. B. Bornschein
	Dipl.-Phys. M. Röllig

Karlsruhe, 31 March 2015

Version history

Print version is version 1.0 from 30 March 2015.

This is version 1.1 from 31 March 2015:

- A version history is introduced
- An empty double page is inserted after the front page and after chapter 5
- In figure 2.5, the x-axis label is changed from *Photon energy (keV)* to *photon energy (keV)*
- The introduction to section 4.2 is rewritten corresponding to the order of subsections
- In the caption of figure 4.7, the phrase *The empty diamonds estimate the dosage, which might deviate by a factor of about 2.5 (see section 4.2.5) from the real value.* is replaced by *The empty diamonds estimate the dosage, displayed without gas correction factor (see section 4.2.5).* The division of the caption into paragraphs is removed.
- The height of figures 4.3 and 4.7 is reduced from 10 cm to 8 cm
- The height of figure 4.5 is reduced from 10 cm to 8.5 cm
- In section 4.7.3, two phrases were corrected: The word *dirft* was corrected to *drift* in the phrase *This would cause for the BIXS monitors at the KATRIN rear wall a linear drift.* And the word *be* was inserted in the phrase *The time estimate for stable measurement conditions deduced above can thus be applied to these surfaces more appropriately.* Also, the separation of paragraphs before the phrase *Also, the pressure at the rear wall...* was removed.

Contents

List of Figures

List of Tables

Introduction

Tritium adsorption occurs as an undesired effect in tritium processing [Nak98]. At the Tritium Laboratory Karlsruhe (TLK), this concerns the development of fusion technology [Nis92] and the Karlsruhe Tritium Neutrino (KATRIN) experiment [Bab12]. Adsorbed tritium is lost for the actual processing purpose [Nak98]. By diffusion, radioactive tritium may further be released into the environment, which is a safety issue [Nis06]. Therefore, distinct knowledge about tritium adsorption is required.

Tritium monitoring is a consequence to determine the distribution of adsorbed tritium inside the processing facility [Nis06]. Tritium monitoring can be realised with Beta Induced X-ray Spectrometry (BIXS) [Wes60]. This method is applied for example in the KATRIN experiment [Bab12]. The detector of a BIXS system needs to be separated from the gaseous tritium by an X-ray transparent window. The window commonly consists of gold coated beryllium [Röl13], [Bab12], [Roe15a]. Tritium adsorption on the window can cause a background to the measurement. Accounting for this background requires to know the tritium coverage of gold after a certain time at a given pressure.

Adsorption occurs at the interfaces of gases and solids [Zan88] [Lüt97] [Iba06]: a particle from the gas phase is bound to the solid surface by mutual interaction. The coverage of the sample with gas particles can change its mechanical and electrical properties [Zan88]. Surface science knows other so termed sorption processes, which emanate from the adsorbed state: for example desorption, the inverse process of adsorption, and diffusion of the adsorbed particles into the bulk.

Tritium adsorption on gold coated beryllium is meanwhile not well investigated. This is despite the importance of this process for tritium processing and the ubiquity of adsorption. To the knowledge of the author, no information about tritium adsorption on gold at room temperature exists in the literature.

For this reason, the Tritium Adsorption Desorption Experiment (TRIADE) was set up within the scope of a Master's thesis at the TLK [Sch13]. It allows the investigation of tritium adsorption on arbitrary solid samples. The sample can be exposed to gaseous tritium in the high vacuum pressure range. The activity on the sample surface is then monitored with a BIXS system. The detector count rate is proportional to the tritium coverage of the sample. Thus, TRIADE allows the time resolved monitoring of tritium adsorption on arbitrary solid samples.

Tritium adsorption on a gold coated beryllium sample is investigated with the TRIADE setup in the scope of this work. These are the first adsorption measurements with TRIADE, allowing a statement about the performance of the setup. The experimental conditions fit those of the BIXS monitoring system in the KATRIN experiment. With respect to its demands, the four specific questions to the tritium adsorption measurements on gold coated beryllium are:

- Does tritium adsorb on a sample of gold coated beryllium?
- If so, which is the saturation coverage?
- After which time is the saturation coverage reached?
- In case of adsorption, how can the sample best be decontaminated?

Investigation of tritium adsorption requires a general knowledge about sorption processes. This is provided in chapter 1. Chapter 2 explains the BIXS method, which is fundamental to the TRIADE setup outlined in chapter 3. The four specified questions to tritium adsorption on gold coated beryllium are finally investigated in chapter 4. Chapter 5 summarises the answers and gives an outlook on future investigations with TRIADE.

1 Theory of sorption processes at interfaces of gases and solids

Adsorption of gaseous tritium on gold coated beryllium is a sorption process. Sorption processes occur at the interfaces of gases and solids and induce a coverage of the solid surface with atoms from the gas phase [Lüt97].

The investigation of adsorption requires a general understanding of sorption processes. Accordingly, an overview of them is given in section 1.1. Based on surface interactions, section 1.2 provides models for dissociative adsorption and time dependence of the surface coverage. Expectations for tritium adsorption on gold are derived from hydrogen measurements in section 1.3. In this work, hydrogen denotes the isotope ^{1}H.

The importance of a good understanding of tritium adsorption in science and technology is demonstrated in section 1.4. There is however only scarce knowledge about tritium adsorption, which is summarised in section 1.5. The four main objectives for the investigation of tritium adsorption in this work are concretised in section 1.6.

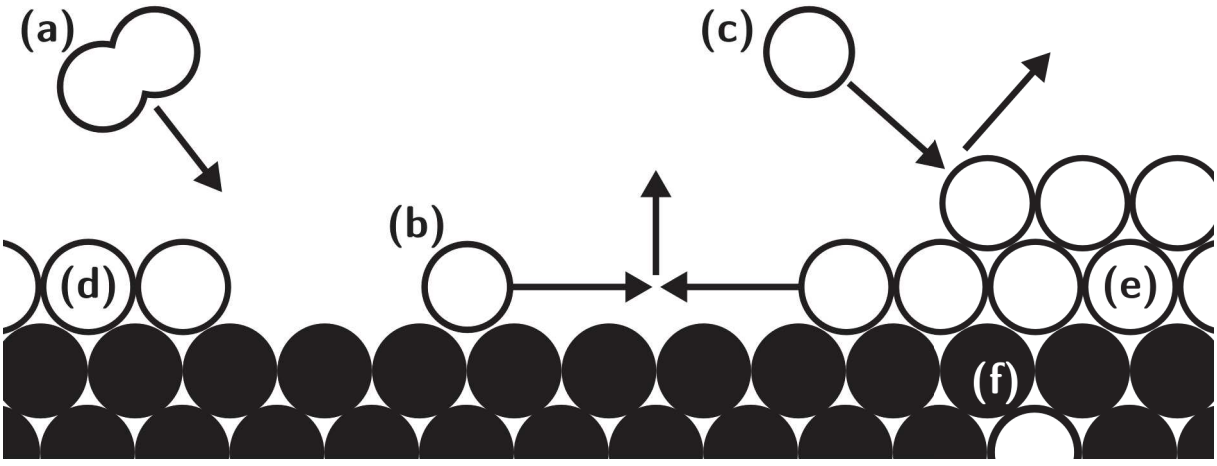

Figure 1.1: Sorption processes at gas / solid interfaces: (a) Impinging atoms from the gas phase adsorb on the substrate surface as adatoms and form the adsorbate. They may do so associatively as molecular compound or as dissociated atoms. The reverse process is called desorption: (b) Adatoms diffusing over the surface may reassociate and desorb via Langmuir-Hinshelwood mechanism. (c) An adatom can also associate with an impinging gas particle via Eley-Rideal mechanism. Those processes can be catalytic. Adsorption may occur in (d) monolayers or in (e) multilayers. (f) Adatoms can further be absorbed in the bulk and permeate through it.

1.1 Sorption fundamentals

At te interfaces of gases and solids, interactions occur between atoms or molecules in the gas phase and the solid surface [Lüt97]. Particles from the gas phase impinge on the solid surface and may scatter back or stick to it after losing energy to the solid [Zan88]. This sticking is due to surface interactions described in the subsequent section. The process of accumulation of gas particles on the solid surface is called adsorption. Adsorbed atoms are called adatoms and constitute the adsorbate. The solid surface is named substrate in the scope of this work.

If the adsorbed atoms have sufficient energy, they can diffuse on the surface [Zan88]. They may cluster [Atk06] or assume a structured pattern [Bar11], depending on their mutual interaction. Adsorbed species may further dissolve into the bulk, thus being absorbed [Lou75]. Permeating through the bulk [Röh76], they might desorb from its opposite side.

The reverse process of adsorption is called desorption [Zan88]: If gas compounds dissociated upon adsorption, two adatoms may recombine in the Langmuir-Hinshelwood mechanism. Also, an adatom can associate with an impinging particle from the gas phase, both leaving the surface in the Eley-Rideal mechanism. If new species are formed in the process, this is a catalytic reaction. Within the scope of this work, all those processes mentioned before are called sorption processes.

On the substrate, distinct binding sites are determined by the minima of the total potential of adsorbate and substrate [Zan88]. Further, adatom diffusion is influenced by surface steps and defects [Atk06]. Therefore, adsorption behaviour varies for different kinds of substrates [Zan88].

Adsorption depends on the temperature of the gas phase: To be trapped in the adsorption well, the gas particles need to lose some kinetic energy by interaction with the surface [Zan88]. Therefore, the probability for adsorption rises with declining temperature if no adsorption barrier exists. In vacuum technology, cryopumps make use of this effect [Jou08]: In cryosorption, a low-boiling gas binds for example to a refrigerated solid adsorption material.

Adsorption can occur in multiple layers [Bar11]. Multilayer adsorption is always because of so called physisorption. Monolayer adsorption may be due to physisorption or so called chemisorption.

The distinction of physisorption and chemisorption may be made with respect to adsorption enthalpy [Bar11]. However, physisorption and chemisorption will be distinguished based on their fundamental interactions in the following sections.

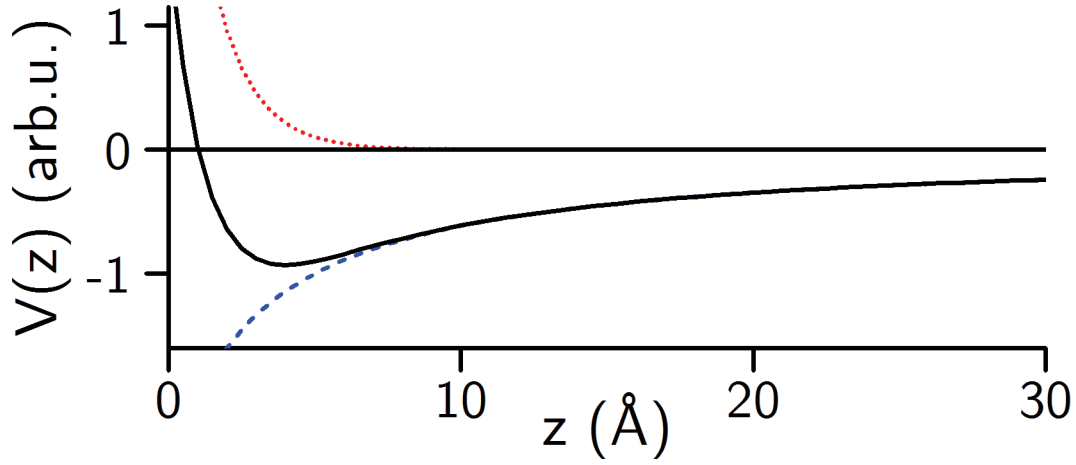

Figure 1.2: Van der Waals potential [Zan88]. At far distances, dipole fluctuations in the charge distribution of the gas atom induce an attractive potential with the surface (dashed blue). At close distances, Pauli repulsion between surface and adatom prevails (dotted red). The resulting potential (black curve) has its minimum typically between 3Å and 10 Å [Lüt97].

1.2 Sorption models

Sorption processes can be classified by the underlying interaction: Physisorption is based on van der Waals interaction and causes considerably weak binding [Zan88] (section 1.2.1). Chemisorption is based on ionic and covalent bonds, which are strong enough to split up molecules [Zan88] (section 1.2.2). Combining these two mechanisms, a model for dissociative adsorption of molecules is presented in section 1.2.3. Also, a model for the time dependence of the surface coverage from adsorption is presented in section 1.2.4.

1.2.1 Physisorption

Physisorption occurs due to van der Waals interaction between the substrate and adatoms. Figure 1.2 shows the van der Waals potential [Zan88]. It consists of an attractive part $\propto |z-z_0|^{-3}$, depending on the distance between the location of the particle $()z$) and the surface $()z_0$): Dipolar fluctuations in the atomic charge distribution are attracted to their image charges in the polarisable solid. Closer to the surface, this is outweighed by Pauli repulsion due to its exponential growth [Iba06]. Adatoms are bound in minima of the van der Waals potential, which are at 3 Å to 10 Å from the surface [Lüt97].

In general, physisorption potentials show small binding energies of 10 meV to 100 meV [Lüt97]. Since at room temperature $kT \approx 25$ meV, physisorption appears only at low temperatures. Its study also requires the absence of strong chemical bondings as from chemisorption. Compared to chemical interactions, physisorption is of long range [Zan88] and with all atoms of the surface [Iba06].

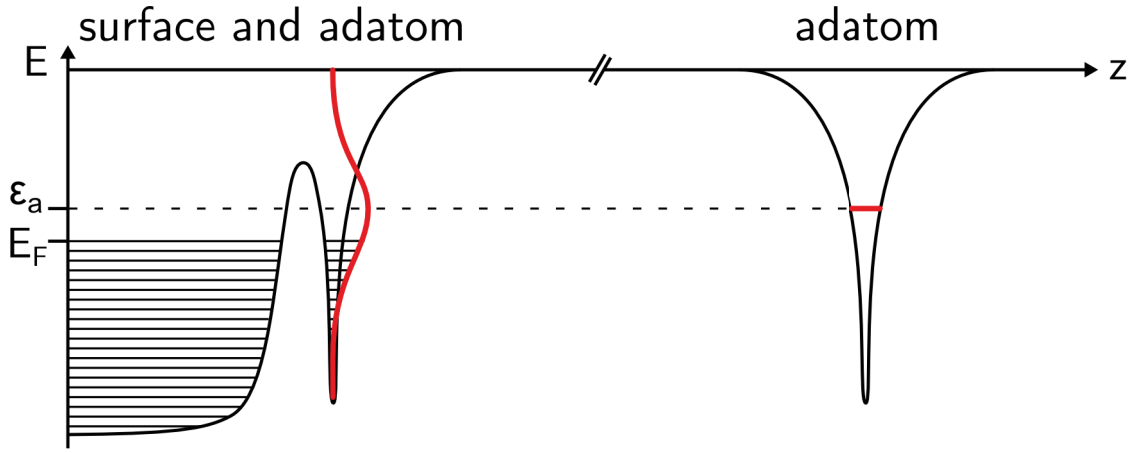

Figure 1.3: The resonant level model allows a simplified description of chemisorption bonds on metal substrates. understanding of the The atom is represented by a potential well (right) with a single electronic energy level at ϵ_a (bold red). The surface is approximated with free electrons in a uniform positive charge. When the atom approaches the surface, their eigenstates mix (left). The sharp energy level of the adatom's electron is broadened into a resonance. In this depiction, a shift of ϵ_a due to the mixing of the eigenstates is not considered. The nature of the bond derives from the distance between ϵ_a and the Fermi level E_F of the substrate: If $|E_F - \epsilon_a|$ is large, an ionic bond ensues. If $|E_F - \epsilon_a|$ is small, adsorbate and substrate share electrons in a covalent bond. Figure according to [Zan88].

1.2.2 Chemisorption

Chemisorption is based on a strong, short range force causing a chemical bond of the adsorbate to the substrate [Zan88]. It is characterised by a relatively high binding energy of several eV [Lüt97]. The general equilibrium separation distance between adatom and substrate is 1 Å to 3 Å.

The nature of the chemical bond can be described with the resonant level model, see figure 1.3: The adatom is considered as a potential well containing a single bound state. The substrate is represented by free electrons in a uniform positive charge, that fill half of space. When the atom approaches the surface, its free elecron's wave function overlaps with the surface charge density. Their eigenstates mix and the atomic level is broadened into a resonance, that can tunnel into the metal. For transition metals as gold, the model has to be expanded to account for their electron structure.

The resonant level model yields two limiting cases for the nature of the surface bond. It is determined by the distance between the energy ϵ_a of the resonant level and the Fermi energy E_F of the substrate. In the limit of large $|E_F - \epsilon_a|$, an ionic bond ensues: As the resonance lies above (below) E_F, charge transfer occurs from the adsorbate (substrate) to the substrate (adsorbate). In the limit of small $|E_F - \epsilon_a|$, adsorbate and substrate share electrons in a covalent bond. For a detailed picture, the electronic structure of the adsorbate-substrate system needs to be examined.

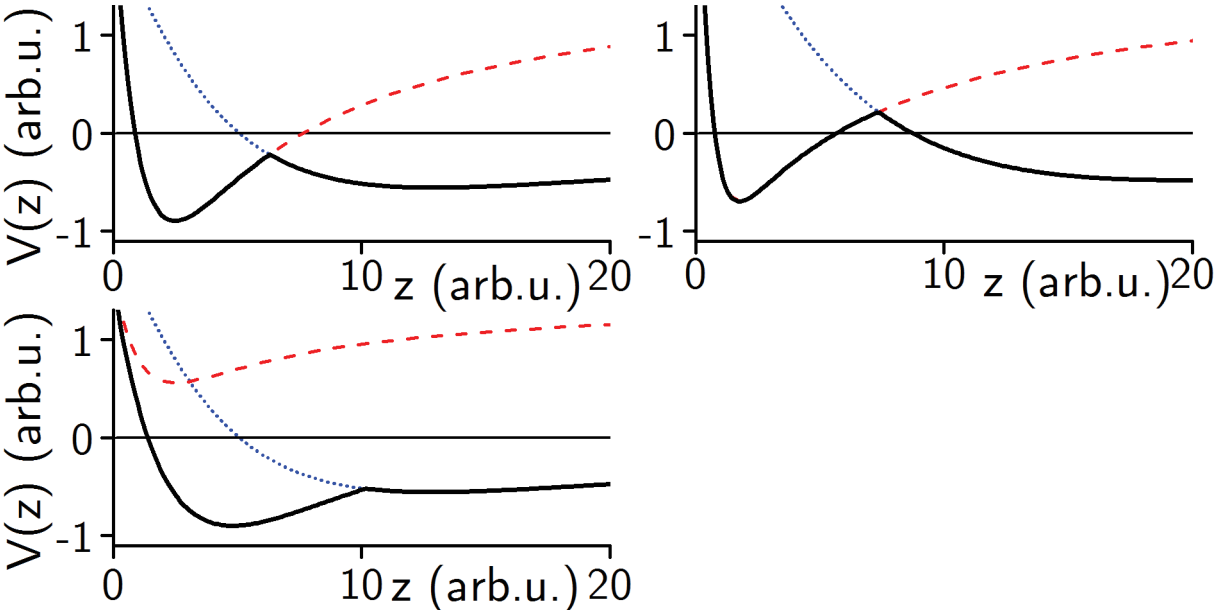

Figure 1.4: Dissociative adsorption in the Lennard-Jones model. Dotted blue: physisorption potential of molecule and surface depending on their mutual distance z. Dashed red: potential of dissociate atoms from physisorption and chemisorption. Bold black: their minimum is the adsorbate potential. Dissociative chemisorption occurs (top left) if their crossing point lies below zero, i.e. the molecular potential for large z. If it lies above, molecular physisorption ensues initially (top right). From this precursor state, the adsorbate will eventually be carried thermally to the minimum of dissociated chemisorption. Non-dissociative, molecular chemisorption (bottom left) introduces an additional minimum to the molecular potential. Also, it must always be smaller than the potential of the dissociate atoms. Figure and model according to [Zan88].

1.2.3 Molecular dissociation upon adsorption

Upon adsorption, a molecule from the gas phase can be split into its constituent atoms. On the surface, this requires two empty nearest-neighbour sites [Iba06].

Dissociative adsorption can be explained qualitatively by a model of Lennard-Jones [Zan88]. It considers the potential of surface and gas particle as function of their mutual distance. For molecules which do not chemisorb, the potential displays only a physisorption minimum. The potential of the separated atoms must lie above the molecular potential far from the surface. Approaching the surface, it develops a minimum from physisorption and chemisorption. The true adsorbate potential is the minimum of both curves. Their crossing point determines the adsorption behaviour.

Figure 1.4 shows three examples of the Lennard-Jones model: Dissociative chemisorption, molecular physisorption with a precursing physisorbed state and direct molecular chemisorption. The latter requires chemisorption of the molecule to the surface, however. Other possibilities might be multiple precursor states and direct competition between atomic and molecular chemisorption.

1.2.4 Time dependence of the surface coverage

The time dependence of the coverage θ can be described using a thermodynamic approach. Basically, θ is determined by the rates of adsorption $\dot{\theta}_{\mathrm{ad}}$ and desorption $\dot{\theta}_{\mathrm{des}}$ [Lüt97].

The adsorption rate is the amount of adsorbing particles per unit time and surface area [Lüt97]:

$$\left(\frac{\mathrm{d}\theta}{\mathrm{d}t}\right)_{\mathrm{ad}} = S(\theta) \cdot J. \tag{1.1}$$

Gas phase of pressure p is supposed to be in thermal equilibrium with the solid of temperature T. Both influence the flux J of impinging particles and on the particles' mass m:

$$J = \frac{p}{\sqrt{\text{const. } m\ T}}. \tag{1.2}$$

Their probability to stick to the surface is the sticking coefficient $S(\theta) \leq 1$ [Atk06] given by [Lüt97]:

$$S(\theta) = \sigma\ f(\theta)\ \exp\left(-\frac{E_{\mathrm{act}}}{kT}\right). \tag{1.3}$$

The condensation coefficient σ accounts e.g. for energy transfer from adatom to substrate and molecular mobility on the surface. The exponential term depends on the activation barrier for chemisorption of energy $E_{\mathrm{act}} = E_{\mathrm{des}} - E_{\mathrm{B}}$. Here, E_{B} is the binding energy and E_{des} is the desorption energy of the adatom. The occupation factor $f(\theta)$ considers the probability of an impinging atom to hit an adsorption site. For non-dissociative adsorption, it is:

$$f(\theta) = 1 - \theta. \tag{1.4}$$

Dissociative adsorption requires two neighbouring empty sites. In the regime of low coverages and high mobility of adatoms, it can be approximated by:

$$f(\theta) \approx (1 - \theta)^2. \tag{1.5}$$

The desorption rates are of negative sign, as they decrease the number of adsorbed surface atoms. They depend on the reaction partners of the desorption process.

Two limiting cases exist: Two chemisorbed species associate and leave the surface by the so called Langmuir-Hinshelwood mechanism [Zan88]. Because of the two involved atoms, the occupation factor is of second order. In the other limit, a chemisorbed species reacts with an impinging gas particle. The compound then leaves the surface by so called Eley-Rideal mechanism [Zan88]. It depends on the surface coverage only in first order, as only one reaction partner is located on the surface.

1.3 Sorption of hydrogen on gold

Tritium is one of three hydrogen isotopes. Experimentally, the adsorption of the hydrogen isotope ^{1}H protium on gold has been well investigated The results are presented in this section as a reference for tritium sorption (see section 1.5). Section 1.3.1 summarises some basics about hydrogen adsorption on gold. Then, models for the time dependence of the surface coverage are presented: for adsorption on an initially clean gold sample (section 1.3.2); for desorption under constant evacuation (section 1.3.3); and for simultaneous adsorption and desorption (section 1.3.4).

1.3.1 Fundamentals of hydrogen sorption on gold

Molecular hydrogen does not chemisorb on surfaces because H_2 has no Highest Occupied Molecular Orbit (HOMO) or Lowest Unoccupied Molecular Orbital (LUMO) near the Fermi level of substrates[Iba06]. Due to the small polarisability of the hydrogen molecule, physisorption interaction is also weak.

Contradictory information exists about dissociative H_2 adsorption on gold (see figure 1.4): [Iba06] states spontaneous dissociation of H_2 on transition metals without significant activation barrier. [Lis87] observed dissociative hydrogen adsorption only on unsintered gold films deposited at 78 K. No dissociative adsorption was observed on gold films deposited at temperatures above 320 K. [Sto94] derives an activation barrier for adsorption of H_2 on gold from measurements at 78 K corresponding to at least 3,000 K thermal energy.

Atomic hydrogen was found to adsorb on about 70 nm thin gold films at 78 K [Sto92]. Its bonding to surfaces is local and covalent [Iba06]. A single hydrogen adatom prefers adsorption sites with a high number of neighbouring surface atoms [Iba06]. At coverages above $\theta \cong 0.01$, another, weakly bound hydrogen adspecies was found [Sto92]. This species is supposed to be a compound of two hydrogen atoms. Such dimers could form due to the low binding energy and high mobility of hydrogen atoms on the surface. The bond between the hydrogen atoms would weaken their bond to the surface.

Adsorbed hydrogen is known to diffuse into the bulk [Ich84]. It also changes electronic properties of the surface like the work function [Mil06].

For later purposes, the surface density n of adsorption sites on gold may be estimated. It is assumed to be equal to the number of surface atoms due to the fcc structure of gold [Hof13]. With the lattice constant $g_{\mathrm{Au}} = 4.08$ Å [Foi86], this yields [Sch13]:

$$n \approx \frac{1}{g_{\mathrm{Au}}^2} = 6.0 \cdot 10^{18} \ \frac{1}{\mathrm{m}^2}. \tag{1.6}$$

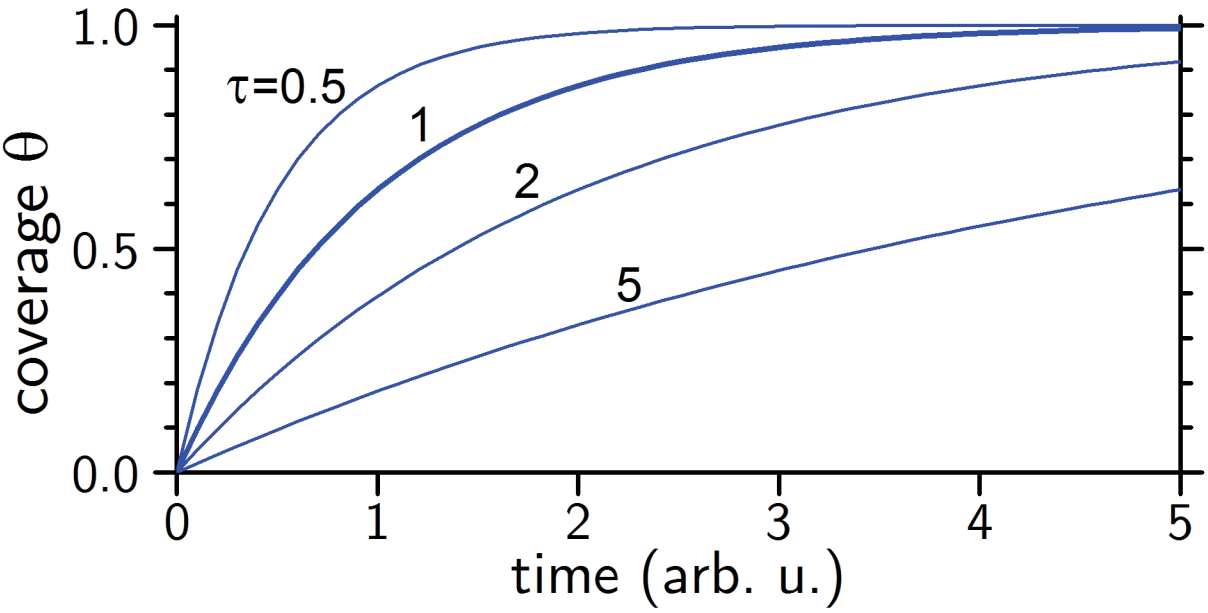

Figure 1.5: Time dependence of the hydrogen coverage θ on an initially clean gold surface due to adsorption according to equation 1.9. It derives from an experimentally justified differential equation for the adsorption rate [Sto92]. The time constant τ is varied in an arbitrary time unit.

1.3.2 Hydrogen coverage on gold due to adsorption

Hydrogen adsorption was investigated on a gold film of about 70 nm [Sto92]. The gold was deposited with a rate of about 1 mg Au / min at 78 K, which suggests a monocrystalline surface. However, subsequent sintering at 420 K for about 30 min may have altered the crystal structure of the surface. On this sample, hydrogen adsorption was investigated at $\approx 2.6 \cdot 10^{-3}$ mbar and 78 K. The adsorption rate was found to fulfill the general model from section 1.2.4:

$$\left(\frac{\mathrm{d}\theta}{\mathrm{d}t}\right)_{\mathrm{ads}} = (1-\theta)/\tau, \tag{1.7}$$

with the time constant τ:

$$\frac{1}{\tau} = \frac{S_0\ J_H}{N_{\max}}. \tag{1.8}$$

J_H is the total impinging hydrogen stream. S_0 is the initial sticking probability on a clean surface. $N_{\max}$ is the saturation coverage.

A solution to differential equation 1.7 can be found with an integration ansatz as shown in appendix A.1. For an initially clean sample with $\theta_0 = 0$ and with the choice $t_0 = 0$, figure 1.5 shows the time dependence of the coverage:

$$\theta(t) = 1 - \mathrm{e}^{-t/\tau}. \tag{1.9}$$

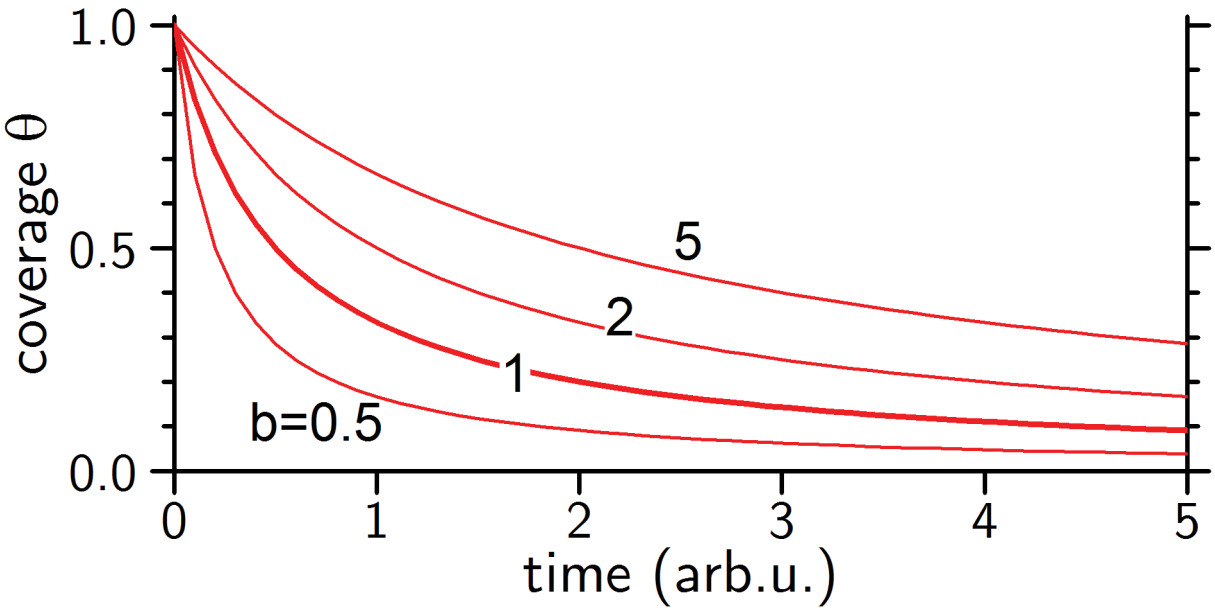

Figure 1.6: Time dependence of the hydrogen coverage θ on gold due to Langmuir-Hinshelwood desorption according to equation 1.11. It derives from the assumption, that desorption is only possible by recombination of two surface atoms. The desorption rate is then proportional to θ^2. The constant b comprises an exponential and preexponential factor given in equation 1.10. It is varied in arbitrary units of time.

1.3.3 Hydrogen coverage on gold under evacuation

If the impinging hydrogen stream $J_H \to 0$, only desorption of the adsorbed hydrogen atoms can occur. In the limiting case of the Langmuir-Hinshelwood (LH) mechanism, two adsorbed species associate and leave the surface (see section 1.2.4). As two adatoms are involved, θ enters the desorption rate in second order. The desorption rate is assumed to follow [Mil06] [Lüt97]:

$$\left(\frac{\mathrm{d}\theta}{\mathrm{d}t}\right)_{\mathrm{LH}} = -\nu \, \exp\left(\frac{-E_a}{kT}\right) \cdot \theta^2, \tag{1.10}$$

Due to the negative sign, the coverage decreases. ν is a preexponential factor to $\exp(-E_a/kT)$, which describes the activation barrier for desorption. It includes the activation energy E_a, the Boltzmann constant and the temperature T of solid and gas.

The Bernoulli equation 1.12 can be solved according to appendix A.2. Choosing $t_0 = 0$, figure 1.6 shows the development of the coverage:

$$\theta(t) = \left(\theta_0^{-1} - b\ t\right)^{-1}. \tag{1.11}$$

θ_0 is the initial coverage. b comprises the exponential and preexponential factor in equation 1.10.

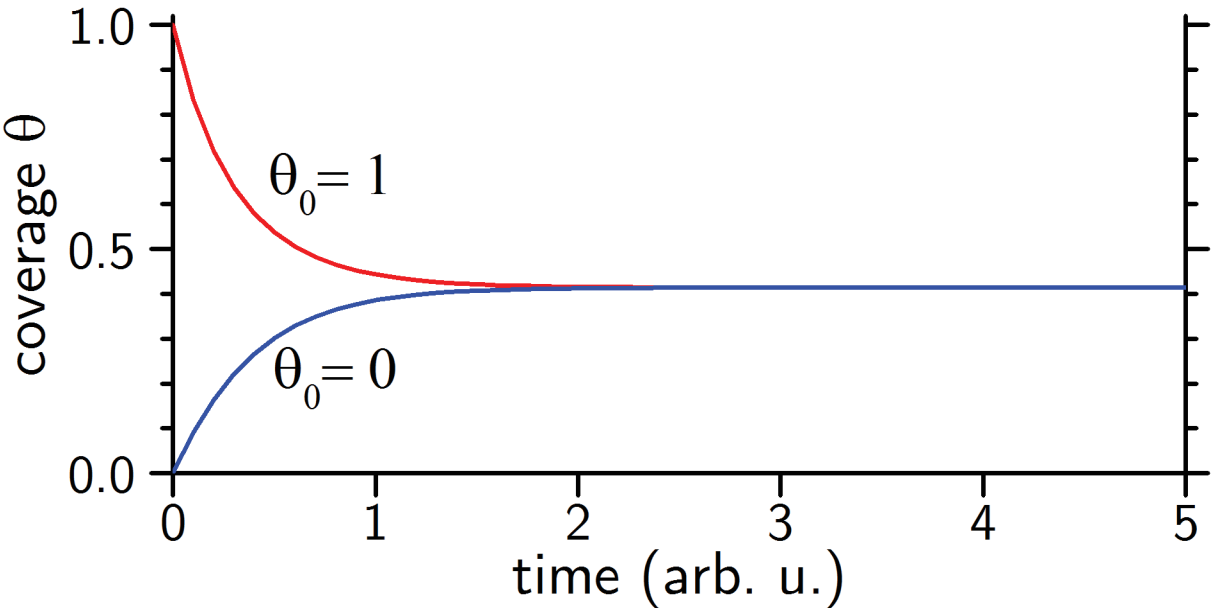

Figure 1.7: Time dependent hydrogen coverage on gold due to adsorption and desorption according to equation 1.16. It derives from a Riccati equation that was obtained as a superposition of adsorption and desorption rates. For an initially clean sample with $\theta_0 = 0$, the coverage increases with time. If all adsorption sites are occupied initially with $\theta_0 = 1$, the coverage will decrease. In both cases, coverage reaches the equilibrium value θ_{eq} given in equation 1.17. It depends on the experimental conditions like gas pressure and temperature.

1.3.4 Hydrogen coverage on gold due to adsorption and desorption

In the two previous sections, models for the surface coverage due to adsorption and desorption were introduced. Desorption was only considered in the Langmuir-Hinshelwood limit. In the Eley-Rideal limit, an adsorbed particle leaves the surface after association with an impinging particle. Under the experimental conditions described in section 1.3.2, it was found to fulfill [Sto92]:

$$\left(\frac{\mathrm{d}\theta}{\mathrm{d}t}\right)_{\text{ER}} = -J_H\ \gamma \cdot \theta. \tag{1.12}$$

Due to the negative sign, the coverage decreases. J_H is the impinging hydrogen stream J_H. γ describes the probability for Eley-Rideal desorption.

For a non vanishing stream of impinging hydrogen atoms J_H, adsorption and desorption effects occur. The total change of the coverage is determined by the superposition of the previously discussed adsorption and desorption rates:

$$\left(\frac{\mathrm{d}\theta}{\mathrm{d}t}\right)_{\text{tot}} = \left(\frac{\mathrm{d}\theta}{\mathrm{d}t}\right)_{\text{ads}} + \left(\frac{\mathrm{d}\theta}{\mathrm{d}t}\right)_{\text{LH}} + \left(\frac{\mathrm{d}\theta}{\mathrm{d}t}\right)_{\text{ER}} \tag{1.13}$$

This yields a Riccati equation for θ [Bro08]. The rates of adsorption, LH and ER desorption are abbreviated with a, b and c. With the initial coverage θ_0 follow the definitions:

$$\gamma = \frac{1}{4}(a+c)^2 + ab, \tag{1.14}$$

$$A = \frac{1}{bN_{\max}}, \qquad B = \sqrt{\gamma} + \frac{a+c}{2}, \qquad D = 2\sqrt{\gamma}, \tag{1.15}$$

the coverage follows the law displayed in figure 1.7:

$$\theta(t) = -AB - \frac{AD}{u_0 D\ \mathrm{e}^{-D\ (t-t_0)} - 1}. \tag{1.16}$$

After long times $t \to \infty$, the equilibrium coverage θ_{eq} is reached:

$$\theta_{\mathrm{eq}} = A\ (D - B). \tag{1.17}$$

The integration constant u_0 can be expressed by the requirement to the initial coverage $\theta(t = t_0) \stackrel{!}{=} \theta_0$:

$$u_0\ D = 1 - \frac{D}{\theta_0/A + B}. \tag{1.18}$$

For $\theta_0 > \theta_{\mathrm{eq}}$, the integration constant has a positive sign and the coverage decreases. For $\theta_0 < \theta_{\mathrm{eq}}$, the sign becomes negative and the coverage increases.

1.4 Tritium sorption in science and technology

The radioactive hydrogen isotope tritium plays a key role in several fields of science and technology. However, undesirable sorption effects occur at surfaces exposed to tritium in gas form. The consequences for tritium processing are shown at three examples: the Tritium Laboratory Karlsruhe (TLK) (section 1.4.1); fusion technology (section 1.4.2); and the Karlsruhe Tritium Neutrino (KATRIN) experiment (section 1.4.3).

1.4.1 The Tritium Laboratory Karlsruhe (TLK)

The Tritium Laboratory Karlsruhe (TLK) at the Karlsruhe Institute of Technology (KIT) is a tritium research facility [Sch91]. Its two missions are the development of fusion technology and the KATRIN experiment, described in the subsequent sections.

Tritium sorption was observed at the TLK e.g. in the the tritium test of pump (TriToP) [Pri13]. Tritium was pumped in a closed loop at 10 mbar to 10^{-5} mbar and at room temperature. The tritium throughput decreased by about 10% during the first week. Also, methanes appeared in the gas stream. This was attributed to tritium isotope exchange, catalytic reactions and diffusion effects. Each might have occurred with the polymer seals of the pump or the stainless steel walls of the setup. Such loss of tritium for its designated purpose due to sorption processes is termed the *system effect* [Nak98].

At the TLK, the TRitium Activity Chamber Experiment (TRACE) is being developed [Roe15a] to monitor gaseous tritium at pressures < 0.9 bar. It contains an X-ray detector, which is placed behind an X-ray transparent beryllium window coated with gold. The recipient is likewise gold coated to minimise tritium adsorption in the field of view of the detector. Despite, tritium adsorption was observed when exposing the recipient to tritium at a static pressure of about 0.7 mbar for about 6 days[1]: the background count rate of the detector rose from (5.58 ± 0.03) cps to (8.14 ± 0.07) cps. This memory effect needs to be considered for tritium monitoring. Ideally, the tritium coverage of the window and recipient is known at every time for a given pressure and temperature.

1.4.2 Fusion technology

The fusion reactors under development will process around 1,000 kg of tritium each year in their fuel systems for 1 GW electric output [Nis06]. Plant operation requires monitoring of the tritium amount and distribution inside the fuel system [Nis06]. This can be achieved e.g. with the TRACE system mentioned in the previous section or with ionisation chambers

[1] David Walter: *Charakterisierung eines BIXS-Systems zur Bestimmung der Tritiumkonzentration in Prozessgasen mittels statischen und dynamischen Messungen*, Bachelor's thesis at the KIT (ITEP-TLK), 2014

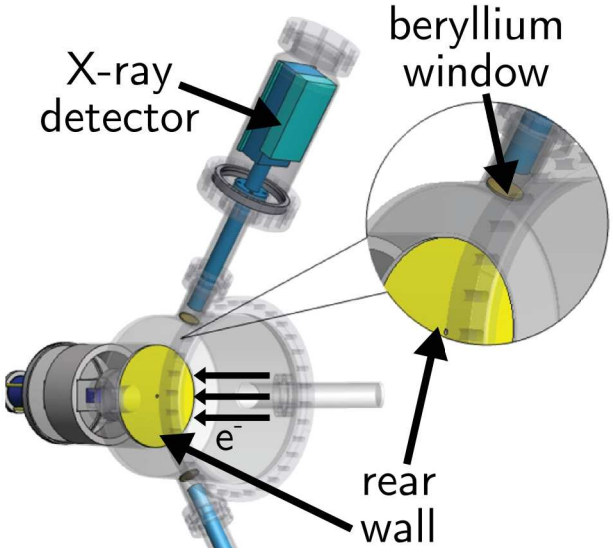

Figure 1.8: Activity monitoring of the KATRIN tritium source with two BIXS systems (see section 2). The two X-ray detectors are mounted in front of the rear wall of the tritium source. They measure secondary radiation from the tritium decay electrons impinging on the rear wall. Each detector is separated from the tritium plasma by an X-ray transparent beryllium window coated with gold. Tritium adsorption on the windows can cause a memory effect and thus a systematic background.

[Mat85]. To reduce chamber contamination by tritium adsorption or isotope exchange effects, gold plating their inside was found favourable [Mat85].

Tritium fuel is supposed to be bred by the fusion plant itself in dedicated blankets [Kos02]. The necessary cooling system could be realised with tubes of F82H steel [Kos02]. Tritium can adsorb on these tube walls, diffuse through them and desorb on the opposite site into the cooling liquid [Hol95]. The tritium is then lost for the fusion process and produces radioactive waste in form of contaminated cooling water. As tritium excess exposure to the outside must be avoided, tritium accountancy is required [Nis06].

1.4.3 The KArlsruhe TRitium Neutrino (KATRIN) experiment

The KArlsruhe TRitium Neutrino (KATRIN) experiment aims for the determination of the neutrino mass [Ang05]. It measures the kinetic energy spectrum of electrons from tritium β decay with a total systematic uncertainty of $\sigma_{\mathrm{sys}}(m_\nu) < 0.13\ \mathrm{eV/c^2}$. This makes special demands to the Windowless Gaseous Tritium Source (WGTS). The WGTS contains a tritium plasma at $5 \cdot 10^{-5}$ mbar to 10^{-3} mbar and at about 30 K with an annual tritium throughput of 10 kg [Bab12].

The start potential of the β electrons is defined by the WGTS [Ang05]. Its potential is required to be stable to $\Delta U < 10$ meV. It depends on the work function ϕ of the WGTS

walls, which can be altered by tritium adsorption. Especially designed to define the WGTS potential, the rear wall of the WGTS consists of a gold coated material [Bab12]. It was observed that hydrogen adsorption on Au(111) causes $\Delta\phi = -160$ meV [Fer12]. Such an influence needs still to be investigated for tritium adsorption on gold. Also, tritium adsorption can change the work function of the steel walls along the inside of the WGTS. A simulation[2] for $\Delta\phi = 1$ eV showed a systematic shift of the neutrino mass: $\Delta m_\nu = 0.040$ eV/c^2. Compared to the allowed $\Delta m_\nu = 0.014$eV/c^2 for WGTS potential variations, this shift needs to be accounted for. This requires knowledge of the saturation coverage of tritium on the steel surface. Corrections based on the saturation coverage also require to know the time after which stable measurement conditions are reached.

The column density ρd of the tritium plasma inside the WGTS is required to fulfill $\Delta\rho d/\rho d < 2 \cdot 10^{-3}$ [Ang05]. It is therefore constantly monitored using its relation to the source activity $a = \epsilon_\mathrm{T} \cdot \rho d$. Measurements of the isotopic content ϵ_T contribute to $\Delta\rho d$. This leaves a requirement $\Delta a/a \sim 1 \cdot 10^{-3}$ for the BIXS system at the rear wall (see figure 1.8) [Bab12]. For the expected count rate of the X-ray detectors of $6.6 \cdot 10^3$ cps follows a maximal uncertainty of 6.6 cps. Background can build up by tritium adsorption on the X-ray transparent beryllium windows coated with gold, which separate detectors and tritium [Bab14]. To account for the consequent shift of the count rate, the saturation coverage of tritium on gold coated beryllium needs to be known.

[2]Nico Werling: *Einflsse von Variationen der Austrittsarbeit innerhalb des WGTS Strahlrohres auf die Neutrinomassen-Sensitivitt des KATRIN-Experiments*, Bachelor's thesis at the KIT, 2015

1.5 Sorption of tritium on gold: state of knowledge

Concerning the adsorption of highly concentrated gaseous tritium on gold surfaces at room temperature, no experimental knowledge exists. As a first approximation, it is assumed to behave similar to that of ^{1}H. However, isotope effects are expected due to the three times higher mass and the radioactivity of tritium.

A first hint to isotope effects comes from the comparison of adsorbed ^{1}H and deuterium on thin gold films at 78 K. Deuterium showed stronger interactions between the adatoms than ^{1}H [Sto96]. This resulted in a lower desorption barrier for deuterium, see figure 1.4.

Due to their small mass, hydrogen isotopes can be described as quantum wave packets. This enables the adatoms to tunnel through the activation barrier for diffusion [Zan88]. On a tungsten substrate at low coverages, diffusion was observed to increase with the mass of the adsorbed isotope. This can be explained with vibrational excitations of the adatoms inside their chemisorption via substrate phonons. Excitation levels of the adatoms depend on their mass. The smaller the mass difference between adatom and substrate, the less phonons are required, the more probable the excitation. Compared to ^{1}H, tritium should have much higher mobility on the surface at room temperature. This should increase probability for Langmuir-Hinshelwood desorption and decrease equilibrium coverage.

An additional isotope effect may arise from the radioactivity of tritium. In tritium decay, an electron is produced, leaving a $^3_2$He ion in the gas phase (see section 2.2). This may evoke radio-chemical effects.

Even samples of a certain material differ in the structure of their surface. Sample preparation like sintering can change the grain size or the crystallographic structure of the surface [Lis87]. This induces specific adsorption sites like kinks and needles, which may influence the sorption behaviour of the adatoms. Those imperfections can further influence the electronic structure of the surface. Accordingly, even samples of the same material show different sorption behaviour. This allows predictions for tritium adsorption only on gold surfaces similar to the investigated sample.

1.6 Objectives of this work

No experimental knowledge about tritium adsorption on gold at room temperature is known to the author. Results for hydrogen sorption from section 1.3 may be not transferable due to isotope effects. Nonetheless, the applications described in section 1.4 require a detailed knowledge of tritium adsorption.

However, the investigation of tritium adsorption faces several difficulties. Primarily, special precautions have to be made in tritium handling [Sch91]: No methods can be applied which require direct surface contact, e.g. gravimetry [Atk06] or elastic neutral atom scattering [Zan88]. Due to the system effect (see section 1.4.1), the flow method [Atk06] is hampered. Thermal desorption spectroscopy [Iba06] is not fit to return information about the time dependence of adsorption. The noninvasive method of Beta Induced X-ray Spectrometry (BIXS) has proved to work for tritium adsorption [Zhe12] [Mat02] and absorption measurements [Mat98]. Therefore, it is chosen for the investigation of tritium adsorption on gold in this work.

At the TLK, a BIXS system was set up for the investigation of tritium adsorption and desorption on arbitrary materials: the Tritium Adsorption Desorption Experiment (TRIADE) [Sch13]. The objective of this work is to perform first tritium adsorption measurements with TRIADE for a sample of gold coated beryllium. The experimental conditions will be fit to those of the activity monitors in the KATRIN experiment described in section 1.4.3.

The four specific questions to those measurements are:

- Does tritium adsorb on a sample of gold coated beryllium?
- If so, which is the saturation coverage?
- After which time is the saturation coverage reached?
- In case of adsorption, how can the sample best be decontaminated?

The interpretation of the measurement results requires a general understanding of the BIXS method. This is provided in the following section.

2 Tritium activity monitoring by beta induced X-ray spectrometry (BIXS)

Beta Induced X-ray Spectrometry (BIXS) meets best the demands of tritium adsorption measurements (see section 1.6). The Tritium Adsorption Desorption Experiment (TRIADE) is based on this method. It is explained by this chapter.

Section 2.1 outlines the working principle and the fundamental interactions BIXS is based on. Section 2.2 treats the beta decay of tritium. The subsequent interactions with matter of the decay electrons and their secondary radiation are treated in sections 2.3 and 2.4. Section 2.5 presents a BIXS spectrum measured with a precursor experiment of TRIADE.

2.1 Working principle of a BIXS system

The working principle of the BIXS method is illustrated in figure 2.1. Electrons from β^- decay receive some of the released energy as kinetic energy. During absorption in the surrounding matter, they produce Bremsstrahlung and characteristic X-rays. This can be measured with an X-ray detector. The X-ray intensity is proportional to the activity of the observed beta source. Being placed behind an X-ray transparent window, the detector is not contaminated.

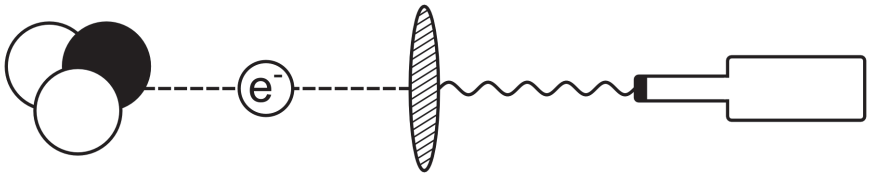

Figure 2.1: Working principle of the BIXS method from left to right: through β^- decay, a nucleus produces an electron with a certain kinetic energy. It interacts with surrounding matter and produces Bremsstrahlung. This can be measured with an X-ray detector. From the measured X-ray intensity, the activity of the source can be deduced.

2.2 The tritium beta decay

BIXS can basically be used to detect any β^- decaying element with a reasonably short half-life. For tritium, it is $T_{1/2} = 12.3$ y [Dem10]. Tritium consists of one proton and two neutrons and decays via:

$$^3_1\mathrm{H} \;\rightarrow\; ^3_2\mathrm{He} + \mathrm{e} + \bar{\nu}. \tag{2.1}$$

Here, T denotes the tritium atom, He the daughter helium atom, e an electron and $\bar{\nu}$ an anti-electron neutrino.

The energy liberated in the tritium decay is $E_0 = 18.590$ keV [Nag06]. Due to energy conservation, it is distributed between the electron and the neutrino, neglecting the recoil energy and excitation of the helium atom. The energy spectrum ϕ of the electrons follows from Fermi's golden rule [Ott08]. Setting the speed of light $c = 1$, the spectrum can be calculated as shown in figure 2.2:

$$\begin{aligned}\phi(\epsilon) = \text{const.}\; & F(E, Z+1) \cdot (E_0 + m - \epsilon) \cdot \sqrt{(E_0 + m - \epsilon)^2 - m^2} \\ & \times \sum_{ij} |U_{ei}|^2 \; P_j \cdot (\epsilon - V_j) \cdot \sqrt{(\epsilon - V_j)^2 - m_i^2} \cdot \Theta\left(\epsilon - V_j - m_i^2\right),\end{aligned} \tag{2.2}$$

where $\epsilon = E_0 - E$ with the kinetic energy E of the electrons. m is the mass of the electron. The sum runs over the three neutrino mass eigenstates m_i with their respective probability $|U_{ei}|^2$. It also runs over the excitation energies V_j of the electronic final states of the daughter atom with their probability P_j. The spectrum depends further on the Fermi function $F(E, Z+1)$ with the Sommerfeld parameter η:

$$F(E, Z+1) = \frac{2\pi\eta}{1 - \exp\left(-2\pi\eta\right)}, \qquad \eta = \frac{\alpha\,(Z+1)}{\beta}, \tag{2.3}$$

where α is the fine structure constant and Z denotes the atomic number of the mother atom. $\beta = v/c$ is the fraction of the electron velocity v and the speed of light c.

2.3 Interactions of tritium beta electrons and matter

Electrons lose energy interacting with the matter they traverse. Two processes are of special interest for BIXS. The production of characteristic X-rays by ionisation and Bremsstrahlung by scattering.

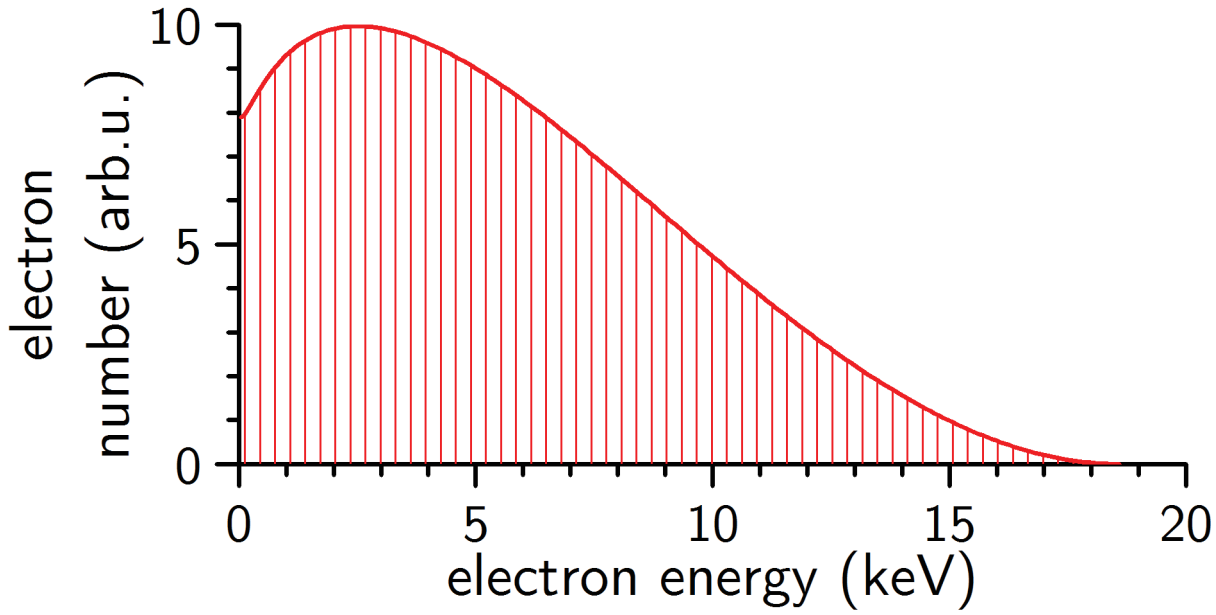

Figure 2.2: Energy spectrum of electrons from the tritium beta decay. It is calculated using Fermi's golden rule according to equation 2.2 [Ott08]. Contributions of electronic excitations and the neutrino mass have been neglected. The maximum of the spectrum is at about 2.5 keV. The spectral end point is at $E_0 = 18.590$ keV [Nag06].

2.3.1 Ionisation and characteristic X-rays

Electrons lose energy by inelastic collisions and ionisation of the atoms in a traversed material. The energy lost can be described by [Dem10]:

$$\left(\frac{\mathrm{d}E}{\mathrm{d}x}\right)_{\mathrm{col}} \approx \text{const.}\ \frac{n_e}{m_e v^2} \cdot \ln \frac{m_e v^2}{2\langle E_b \rangle}, \tag{2.4}$$

where n_e is the electron density of the target material, m_e the mass of the electron and v its speed. $\langle E_b \rangle$ is the average binding energy of the target electrons.

The shell of an ionised atom can be refilled with an electron from a higher shell. The difference in electron binding energy is released by the emission of a characteristic X-ray photon. It can be calculated with Moseley's law [Gru08]:

$$E = R\ (Z-1)^2\ \left(\frac{1}{n^2} - \frac{1}{m^2}\right). \tag{2.5}$$

$R = 13.6$ eV is Rydberg's constant. Z is the atomic number of the ionised element. n and m are the principal quantum numbers denoting the initial and final shell of the electron. The emitted radiation is called characteristic X-ray, as its energy is characteristic for each element and transition. This property can be used for detector calibration or elemental analysis of material samples. The angular distribution of the emission of characteristic X-rays is isotropic [Kri12].

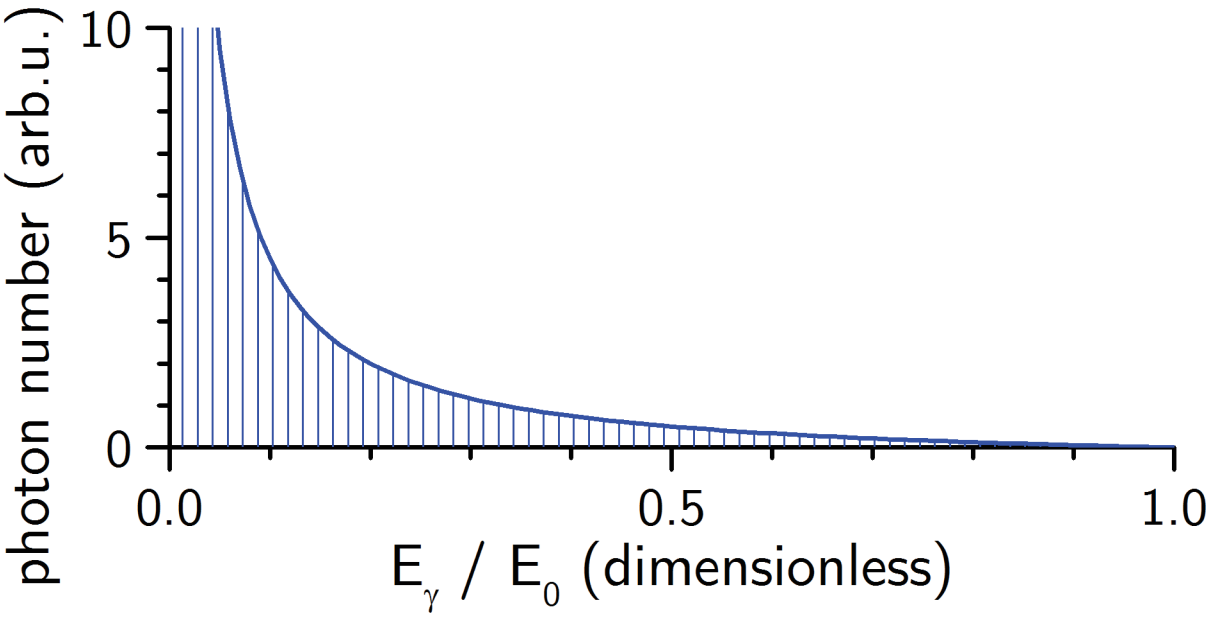

Figure 2.3: Spectral distribution of Bremsstrahlung according to Kramers' rule [Kra23]. It is induced in matter traversed by an electron of incident energy E_0.

2.3.2 Bremsstrahlung

Electrons might also lose energy being inelastically scattered inside the Coulomb field of the nuclei of the traversed material [Gru08]. The energy of the emitted radiation can be described by [Dem10]:

$$\left(\frac{\mathrm{d}E}{\mathrm{d}x}\right)_{\mathrm{rad}} = \text{const. } n_a \; Z^2 \; E_c \cdot \ln \frac{a(E)}{Z^{1/3}}, \tag{2.6}$$

where n_a is the atomic density and E_e denotes the kinetic energy of the incident electron. $a(E)$ is a numeric factor related to the impact parameter.

The energy loss due to Bremsstrahlung rises with the atomic number. So materials with high Z are favorable for the X-ray inducing elements inside a BIXS setup. In contrast to ionisation, the energy loss of Bremsstrahlung rises also proportionally with the electron energy. This leads to Bremsstrahlung being the dominating process at high energies. The critical energy E_c, for which the energy losses of both effects equate, can be approximated for solids by [Gru08]:

$$E_c = \frac{610 \text{ MeV}}{Z + 1.24}. \tag{2.7}$$

For gold with $Z = 79$ [Atk06], $E_c = 7.6$ MeV. So for electrons from tritium decay, the energy loss due to ionisation will prevail. As practice shows, characteristic X-rays about of the same intensity as the continuous spectrum of Bremsstrahlung.

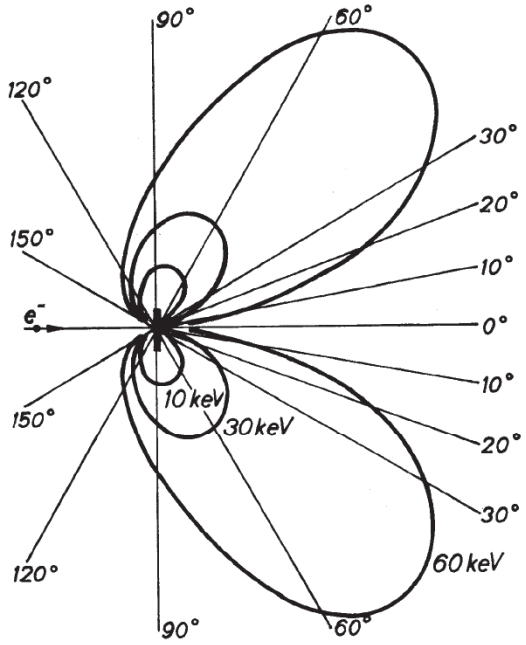

Figure 2.4: Angular distribution of Bremsstrahlung for a thin Wolfram target ($Z = 74$). The major part of the beta electrons has an energy below 10 keV. They induce Bremsstrahlung in the shape of a dipole. Figure from [Kri12].

The energy spectrum ϕ of the induced photons was calculated by [Kra23][1]:

$$\phi(E) = \text{const. } IZ \left(\frac{E_0}{E} - 1 \right), \tag{2.9}$$

where E_0 is the energy of the incident electrons of current I. It is shown in figure 2.3.

The angular distribution of Bremsstrahlung correlates with the energy and direction of the incident electron [Kri12]. For a thin target and an electron of $E_e = 10$ keV, it will however almost take the shape of a dipole. As figure 2.4 shows, the maximal emission probability points away from the incident electron direction by almost 90°.

[1] According to [Kra23], the total energy of the induced Bremsstrahlung with wavelength ν is:

$$I_\nu \propto IZ \ (\nu_0 - \nu), \tag{2.8}$$

with the energy of the incident electron $E_0 = h\nu_0$ and the Planck constant h. This can be written depending on $E = h\nu$. To find the number of radiated photons, the distribution needs to be divided by the individual photon energy E.

2.4 Interaction of X-rays and matter

X-rays from interactions of tritium decay electrons and matter will interact themselves with matter even before being detected. This leads to their deviation and an attenuation of the X-ray intensity. The two dominant interaction processes are the photoelectric effect and Compton scattering.

2.4.1 Attenuation of photons and matter

Interactions between photons and matter lead to an exponential attenuation of a photon beam with the intensity I [Gru08]:

$$I(x) = I_0 \; e^{-\mu x}. \tag{2.10}$$

Here, $x = \rho \cdot s$ is an area density with the unit g/cm^2. It can also be espressed using the density ρ of the material and the covered distance s. The factor μ is the mass attenuation coefficient, which is given by:

$$\mu = \frac{N_A}{A} \sum_i \sigma_i, \tag{2.11}$$

where N_A is the Avogadro number and A is the atomic weight. The atomic cross sections σ_i for all interaction processes i are summed up.

The cross section indicates the probability of an interaction process. It depends on the energy of the photon and material properties. Gold is of special interest, as it is well suited for the production of Bremsstrahlung due to its high atomic number Z (see section 2.3.2). The probability for photon interactions in gold in the energy range of the tritium beta decay are shown in figure 2.5. Two effects occur, which change the photon energy spectrum: the photoelectric effect dominates by at least three orders of magnitude over Compton scattering [Ber10].

Besides being attenuated, photons will be deviated by scattering on matter. This is important for applications of the BIXS method, which rely on the geometry of their setup.

2.4.2 Photoelectric absorption

Photons can be completely absorbed through scattering with an orbital electron, which in turn will leave the shell [Gru08]. This is called the photoelectric effect. For photons below 100 keV, the cross section for this process with one atom is given by the non relativistic Born approximation [Dem10]:

$$\sigma_\mathrm{p} \approx \text{const.} \cdot Z^5 \; / \; E_\gamma^{7/2}. \tag{2.12}$$

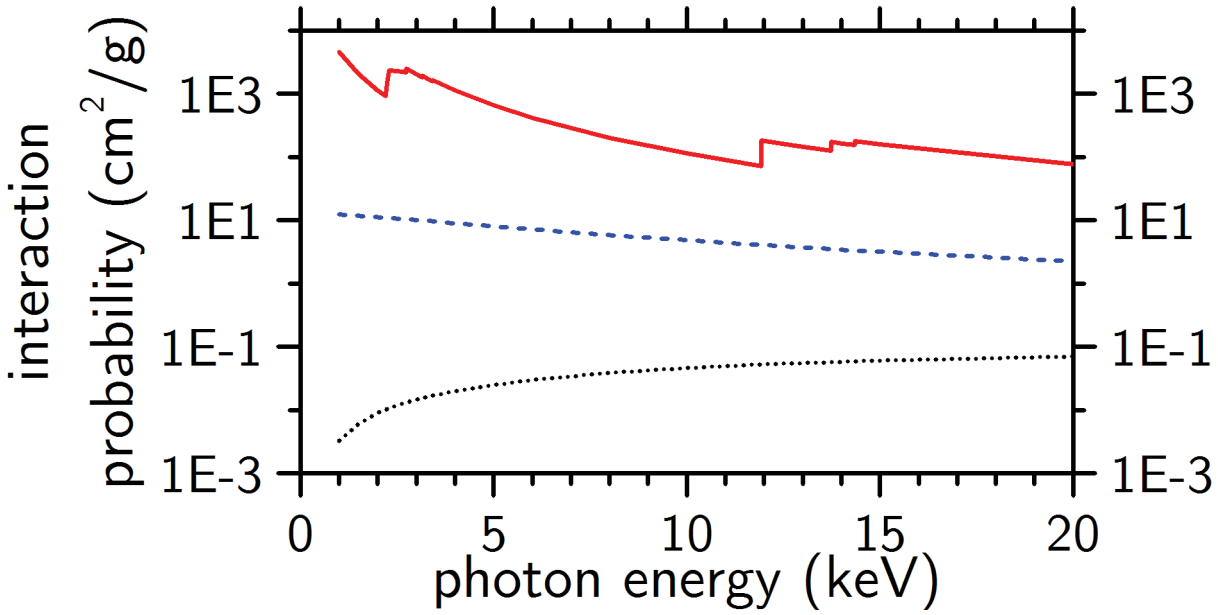

Figure 2.5: Interaction probabilities for photons from tritium decay [Ber10]. Photoelectric absorption (red continuous), coherent Rayleigh scattering (blue dashed) and incoherent Compton scattering (black dotted). Only absorption and Compton scattering change the energy spectrum of the photon [Dem10]. The absorption probability shows absorption edges at the binding energies of gold shell electrons. Pair production is only possible over the threshold energy of about 1 MeV [Kri12]. For beryllium ($Z = 4$), the probability of Compton scattering surpasses that of absorption only for $E > 10$ keV [Ber10].

The probability for the photoelectric effect decreases with rising photon energy E_γ. However, it dominates at energies in the range of the tritium BIXS spectrum. It further rises strongly with the atomic number Z. Hence, the way of photons through materials with high Z should be minimised to avoid their absorption.

2.4.3 Compton scattering

Photons can also scatter on orbital electrons without being absorbed [Gru08]. This process between photons and those quasi-free electrons is called Compton scattering. For photons in the energy range of the tritium beta decay, the cross section for scattering on one atom can be approximated by [Dem10]:

$$\sigma_\mathrm{c} = \mathrm{const} \cdot Z \ \left(1 - 2\epsilon + O(\epsilon^2)\right), \tag{2.13}$$

where $\epsilon = E_\gamma/(m_e c^2)$ is the reduced photon energy with the electron mass m_e and the speed of light c.

The probability of Compton scattering decreases with rising photon energy E_γ and increases with the atomic number Z. However, the influence of Z on photon attenuation

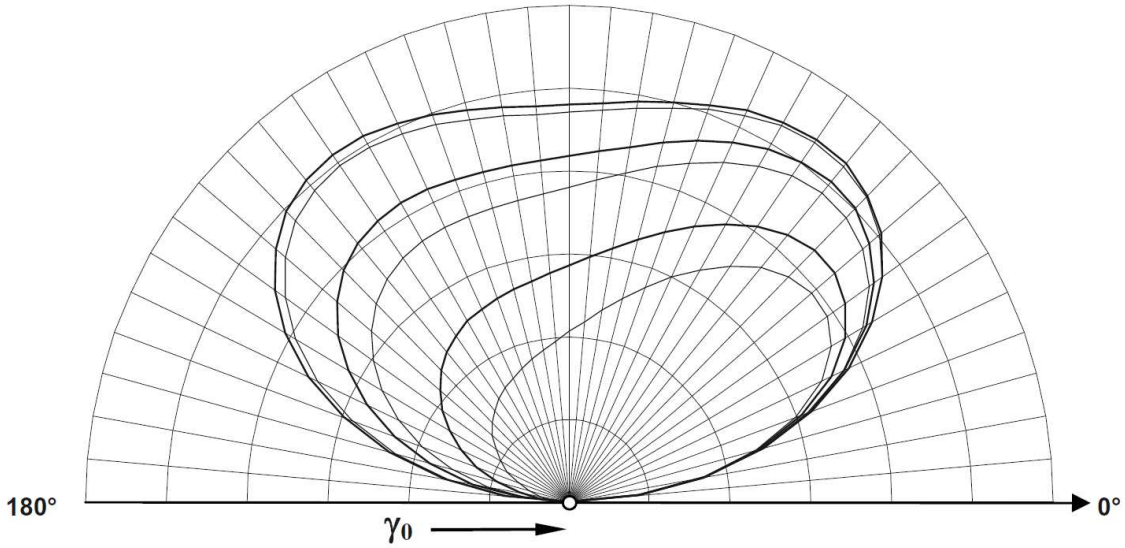

Figure 2.6: Angular distribution of photons after Compton scattering. It is symmetric around the direction of the incident photon γ_0, coming in from the left. The distributions of photons with 10, 50 and 200 keV are shown (from outside). Besides the angular distribution (bold line), the energetic distribution is drawn (thin line). The unit in radial direction is $5 \cdot 10^{-26}$ cm^2/sr for each ring. Figure from [Kri12].

in matter by the Compton effect is small. This is due to the rough proportionality of $Z \sim A$ [Kri12] and equation 2.11.

The energy loss by single scattering of a photon with final energy E'_γ is given by the fraction [Gru08]:

$$f_e = \frac{E'_\gamma}{E_\gamma} = \frac{1}{1 + \epsilon\ (1 - \cos\theta_\gamma)}. \tag{2.14}$$

Here, θ_γ is the scattering angle of the photon in the laboratory system.

The angular distribution of the scattered photons can be obtained from the Klein-Nishina formula [Kri12]:

$$\frac{\mathrm{d}\sigma_\mathrm{c}}{\mathrm{d}\theta_\gamma} = \text{const.}\ f_e \sin\theta_\gamma \cdot \left(1 + f_e^2 - f_e \sin^2\theta_\gamma\right) \tag{2.15}$$

A graphical representation is given in figure 2.6. As it shows, photons in the relevant energy range will preferably be scattered in a wide angle to their incident direction.

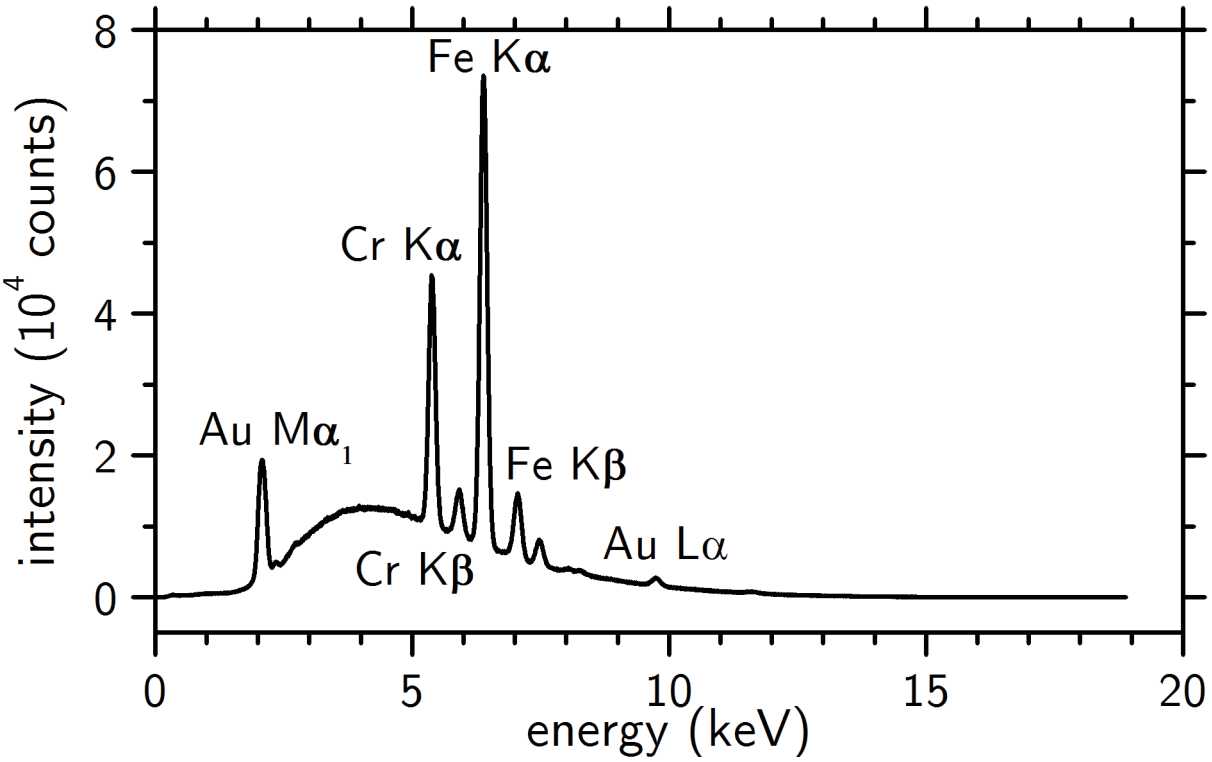

Figure 2.7: Example of a BIXS spectrum measured with the TriReX experiment [Röl13]. The measurement was performed with tritium gas of a total activity of $(6.43 \pm 0.49) \cdot 10^9$ Bq. The BIXS spectrum consists of continuous Bremsstrahlung which is superimposed by characteristic X-rays peaks. The materials in which they were produced can be deduced from the peak energy. Figure from [Röl13].

2.5 Exemplary BIXS spectrum measured with a precursor experiment of TRIADE

The X-rays produced by tritium decay electrons can be measured using an X-ray detector setup. An example of such a BIXS spectrum is given in figure 2.7. It shows the continuous Bremsstrahlung and characteristic X-ray peaks.

The spectrum was measured with the tritium rear wall experiment (TriReX[2]) [Röl13] at the TLK. To separate the detector from the gaseous tritium, it uses a gold coated beryllium window. The gold coating of 100 nm thickness ($Z = 79$ [Atk06]) offers a high probability for the production of Bremsstrahlung. It then traverses the beryllium ($Z = 4$ [Atk06]) with minimal attenuation. A window of the same composition was used for the BIXS setup of the tritium adsorption desorption experiment (TRIADE).

[2]Marco Röllig: *Studien zu einem Röntgendetektorsystem zur Bestimmung der Aktivität in der KATRIN Tritiumquelle*, Diploma thesis at the KIT (ITEP-TLK), 2011

3 The Tritium Adsorption Desorption Experiment (TRIADE)

The Tritium Adsorption Desorption Experiment (TRIADE) was set up at the TLK to investigate tritium adsorption on arbitrary solid samples. Figure 3.1 provides an overview of its working principle.

TRIADE relies on the BIXS method introduced in the previous chapter. Details of the BIXS setup of TRIADE are provided in section 3.1. It also quantifies the contributions to the X-ray detector signal. The measurement conditions are controlled with the vacuum setup, which is described in section 3.2. Section 3.3 gives an overview of the data acquisition and analysis tools. An exhaustive description of the TRIADE hardware and commissioning can be found in the Diploma thesis of Fabian Schneck [Sch13].

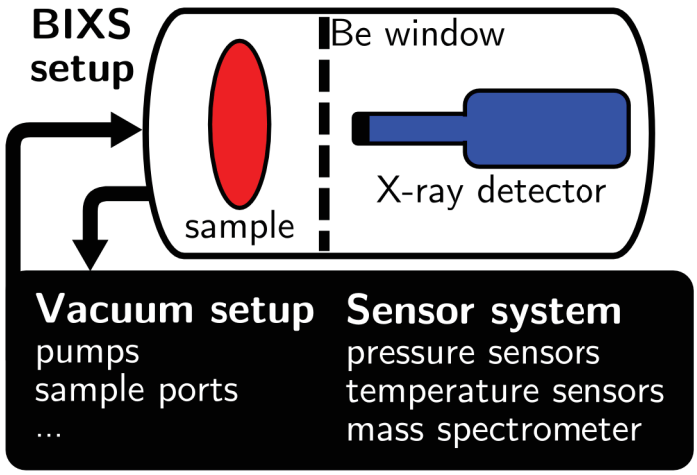

Figure 3.1: Working principle of TRIADE. An arbitrary solid sample is exposed to gaseous tritium in a ultra high vacuum capable DN100CF cross piece serving as recipient. Tritium adsorption is measured by monitoring the activity on the sample (red) with the BIXS method. Behind an X-ray transparent beryllium window (dashed line), the X-ray detector is placed (blue). The measurement conditions are controlled with the vacuum setup. It comprises a sample port to fill and pumps to evacuate the recipient, as well as a sensor system to monitor the conditions. This includes pressure and temperature sensors as well as a mass spectrometer. Compare figure 3.4 for the BIXS setup and figure 3.5 for the vacuum setup.

3.1 The BIXS setup of TRIADE

The BIXS setup of TRIADE as shown in figure 3.2 allows the investigation of tritium adsorption on arbitrary samples. Its core components in the recipient and the X-ray detector are detailed in sections 3.1.1 and 3.1.2. Heavily depending on their geometry is the measurement principle of the TRIADE BIXS system, described in section 3.1.3. Section 3.1.4 quantifies different contributions to the BIXS spectrum based on a simulation.

3.1.1 Core components in the recipient

Although TRIADE allows the investigation of arbitrary samples, only one is used for this work: a substrate of $\geq 99\%$ pure beryllium, sputter coated with 100 nm gold on one side and provided by Materion Electrofusion[1].

The sample is mounted in the recipient on a sample holder with the gold coated side facing the detector. The inner walls of the recipient and the sample holder are also gold coated, too. This is to minimise tritium adsorption and avoid radiation background. The temperature of the sample holder can be controlled with a cold gas system or a heating sleeve. This allows measurements between $T = -150°\mathrm{C}$ and 200°C.

For BIXS monitoring, the recipient contains an X-ray transparent window in front of the sample holder. It consists of 100 µm beryllium with an adhesive layer of 10 nm titanium, sputter coated with 100 nm gold. It was provided by Materion Electrofusion like the sample.

As section 2.4 showed, the attenuation probability for photons in the energy range of interest is dominated by photoelectric absorption. Its cross section $\sigma_\mathrm{p} \propto Z^5$, with the atomic number Z of the material. Therefore, beryllium with $Z_\mathrm{Be} = 4$ [Atk06] was chosen as window substrate. To reduce tritium adsorption on its surface, it was sputter coated with gold with high $Z_\mathrm{Au} = 79$ [Atk06]. To minimise X-ray attenuation in the coating, its thickness was minimised. The contribution of the titanium layer to the X-ray attenuation is small compared to that of gold. This is due to its smaller thickness and lower $Z_\mathrm{Ti} = 22$ [Atk06], neglecting influences of the densities.

Due to the high $Z = 79$ [Atk06] of gold, it also enhances the probability for Bremsstrahlung production. Tritium adsorbed on the window will therefore contribute to the BIXS signal. The same provider of sample and window suggests similar surface structures and tritium adsorption properties. This can be used to investigate systematic effects in the TRIADE setup from tritium adsorption on the X-ray transparent window.

[1] 44036 S Grimmer Blvd, Fremont, CA 94538-6346, USA

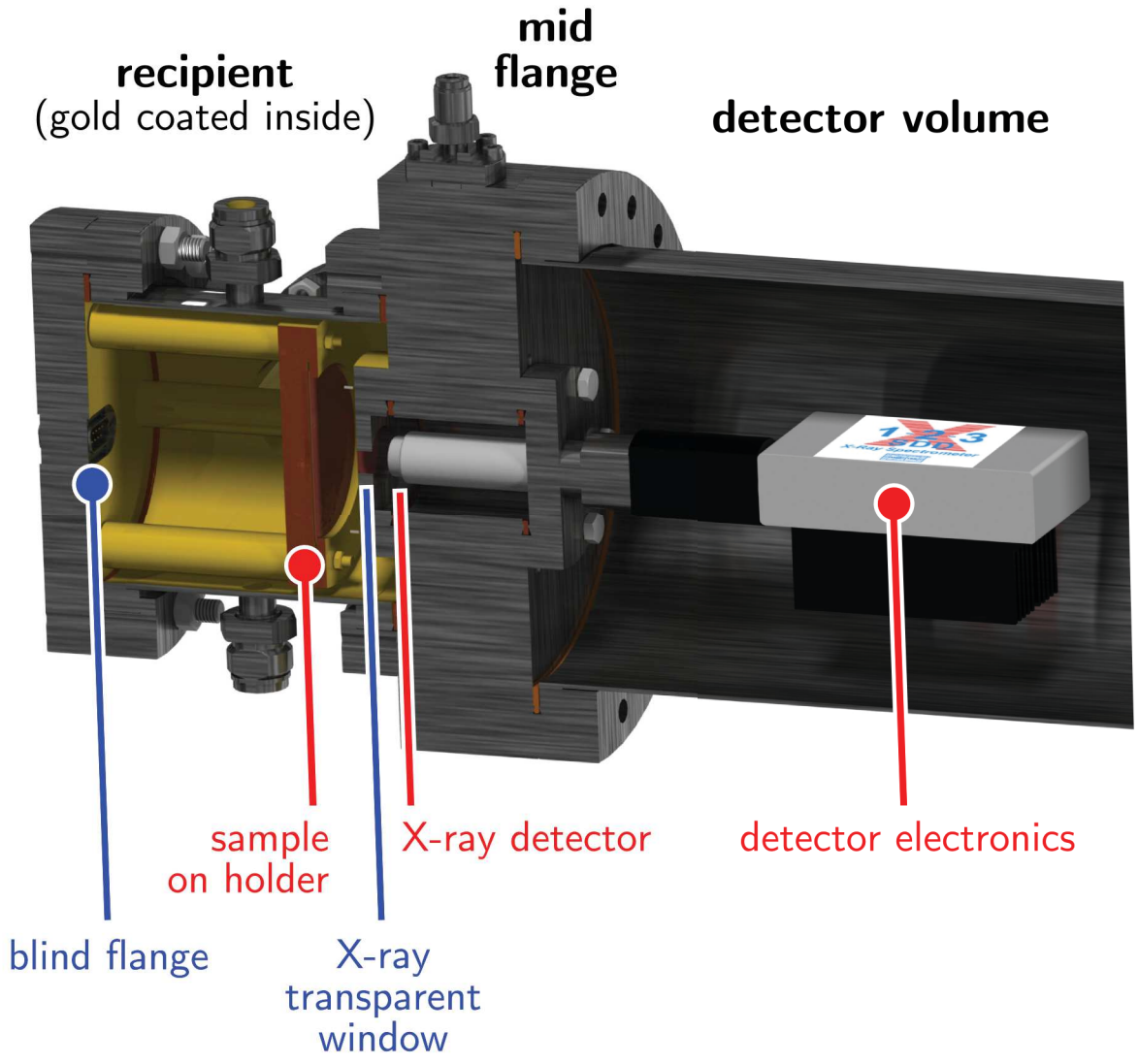

Figure 3.2: CAD drawing of the TRIADE BIXS setup. It consists of a vacuum setup with three volumes. The recipient on the left is blind flanged on its backside. The blind flange contains a feedthrough for a temperature sensor at the sample holder. The temperature of the sample holder can be controlled, if required. Also, the pressure can be controlled inside the ultra high vacuum capable DN100CF cross piece serving as recipient. Recipient and sample holder are gold coated to minimise tritium adsorption and possible subsequent background.
In front of the sample is an X-ray transparent window of gold coated beryllium. On its opposite site, the X-ray detector is installed. It is placed in a mid flange, which is continually evacuated to reduce the mechanical load on the beryllium window. As the detector is not vacuum capable, it is placed in the third volume at 1,000 mbar.

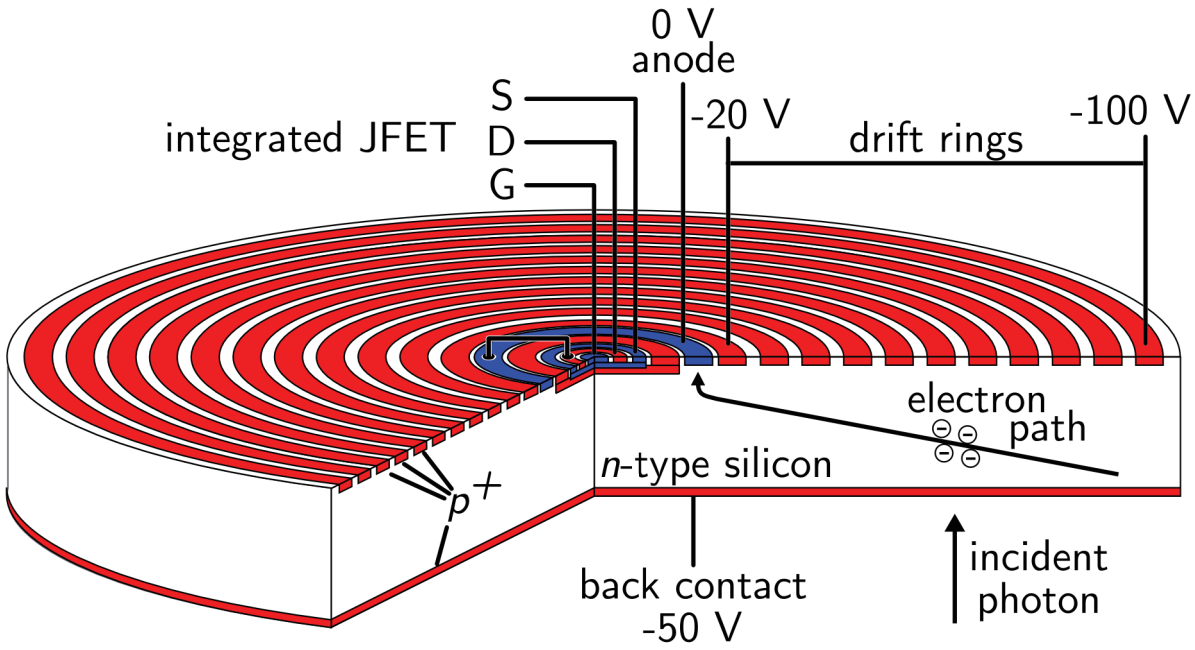

Figure 3.3: Physical layout of a silicon drift detector. The n-type substrate is depleted by a n^+ anode. The large-area back contact and the circular drift electrodes on top are of p^+-type. This creates an electric field in the substrate. Electrons released by incident photons travel alongside it to the anode. Embedded in the anode is a junction gate field-effect transistor (JFET) with the connections source (S), drain (D) and gate (G). It is isolated from the substrate by a p^+ layer. The anode is connected via a bridge to the JFET, which serves as preamplifier in the detector readout.

3.1.2 The X-ray detector: a silicon drift detector (SDD)

The detector used in the TRIADE BIXS setup is a silicon drift detector (SDD). Figure 3.3 shows its physical layout [Egg04]. The n-type silicon substrate is depleted by a small n^+ anode. Electrodes in form of p^+ junctions are applied on the front and rear side. On the rear, this forms one large-area p-n junction. On the front, several drift rings are laid concentrically around the anode. Their voltage becomes gradually more negative towards the outside. This induces an electrical field parallel to the surface. Alongside it, electrons released in the depletion zone by ionising radiation drift towards the anode. The holes drift to the $p+$ junction and are not measured.

Because of the small anode, the output capacitance of the SDD is very small. Also, a junction gate field-effect transistor (JFET) is integrated inside the ring shaped anode. It serves as pre-amplifier to the detector readout and has a good capacitive matching with the SDD. Due to this overall small output capacitance of the SDD, its noise level is very low.

The detector used in the TRIADE BIXS setup is an Amptek X-123 SDD. Its digital pulse processor Amptek DP5[2] digitises the signal from the preamplifier. It then applies digital pulse shaping in two channels with a long and short peaking time respectively. The slow channel is optimised to obtain accurate pulse heights. The fast channel is optimised to obtain timing information for pulse selection. The multichannel analyser finally combines the results of both channels to create a binned energy spectrum. It is read out via USB to a computer.

Calibration measurements were performed [Sch13] to minimise the noise level and the energy resolution. Several parameters as the gain, the peaking times and the energy thresholds of the slow and fast channel were chosen. They can be found in appendix B.3. Out of the 8192 channels of each spectrum, a given channel n is then related to the photon energy with the following calibration:

$$E(n) = a + b \cdot n, \qquad a = (-41.175 \pm 7.871)\ \text{eV}, \tag{3.1}$$

$$b = (2.504 \pm 0.002)\ \text{eV}. \tag{3.2}$$

Using this calibration, the peak resolution of 60.44 channels can be expressed as energy resolution:

$$\Delta E = (151.34 \pm 0.98)\ \text{eV} \qquad @\ 6.2\ \text{keV}. \tag{3.3}$$

Besides the choice of calibration parameters, the noise level is reduced by Peltier cooling the SDD to 220 K:

$$f_{\text{noise}} = (4.11 \pm 0.13)\ \text{cps}. \tag{3.4}$$

[2]The DP5 is described in Amptek, Inc.: *X-123, Complete X-Ray Spectrometer with CdTe Detector, User Guide and Operating Instructions*

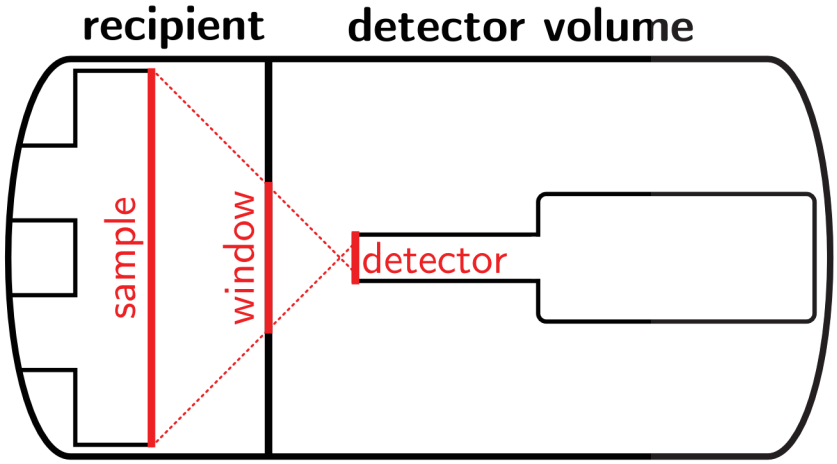

Figure 3.4: Measurement principle of the TRIADE BIXS setup. The sample is mounted on the sample holder in the recipient. The recipient walls contain an X-ray transparent window. Behind it, the X-ray detector is installed. The window acts as a collimator for the detector, restricting its field of view to the sample surface in a 90° angle.
The heights and distances of sample, window and active detector surface are drawn true to scale. The heights are 50 mm for the sample, 20 mm for the window and 7 mm for the detector. Between sample and window lie 15 mm. Window and detector are 12.5 mm apart.

3.1.3 Measurement principle of the BIXS setup

The TRIADE BIXS setup allows for the investigation of tritium on arbitrary solid samples. The sample is mounted on the sample holder in the recipient. The recipient is then filled with gaseous tritium at $p = 5 \cdot 10^{-9}$ mbar to 1,013 mbar, which adsorbs on the sample.

The activity of the adsorbed tritium is monitored with the X-ray detector. As figure 3.4 shows, its field of view is restricted to the sample by the window, which acts as a collimator. Only X-rays from the sample and the X-ray transparent window are detected, as well as from residual gaseous tritium between the both.

Tritium adsorbed outside the detector's field of view could contribute to the signal. As shown in section 2.4, X-rays can be deviated by coherent or incoherent scattering. This could guide photons from the sample holder or the recipient walls to the detector. However, the gap between sample and window is narrow compared to the sample surface. Even more, the surfaces of the sample holder and the recipient walls are gold coated to reduce tritium adsorption. Therefore, this background is deemed neglectable.

The detected X-ray intensity might further be influenced by absorption in residual gas between the sample and window. However, simulations showed no significant absorption effect for pressures below 10 mbar [Roe15b]. For the measurements presented in this work, absorption effects are therefore neglected.

3.1.4 Quantification of BIXS signal contributions by simulation

To interpret the measured X-ray intensity, it needs to be related to the adsorbed amount of tritium on the sample. This is achieved with Monte Carlo simulations.

As a reference, the surface activity a_{ML} of one tritium monolayer on a gold surface is estimated. The surface density n of adsorption sites on gold was calculated in equation 1.6. Together with the tritium half-life $T_{1/2} = 12.3$ y [Dem10], this yields:

$$a_{\mathrm{ML}} = n \, \frac{\ln 2}{T_{1/2}} = 1.07 \cdot 10^{10} \, \frac{\mathrm{Bq}}{\mathrm{m}^2}. \tag{3.5}$$

As discussed in the previous section, only three sources can contribute to the signal measured with the TRIADE BIXS setup. The sample, the X-ray transparent window and residual gas between the both. The expected detector count rate was simulated [Sch13] with PENELOPE 2008 [Sal06]. According to equation 3.5, a surface activity of one monolayer of tritium was assumed for the sample and the beryllium window. For the simulation of the signal from residual gaseous tritium, a pressure of 10^{-8} mbar was assumed. Table 3.1 shows the results. The contribution from residual gas can safely be neglected as can the experimentally determined detector noise. Accordingly, the measurement is only influenced by sorption processes on sample and window.

Table 3.1: Simulated contributions of the TRIADE BIXS signal for one monolayer of adsorbed tritium. The dominating contributions come from the gold coated beryllium sample and window. The contribution of residual tritium gas at 10^{-8} mbar can be neglected. The same goes for the experimentally determined detector noise. From the diploma thesis of Fabian Schneck.

Signal contributor	Simulated signal (cps)
1 monolayer of tritium on the window	4.21 ± 0.08
1 monolayer of tritium on the sample	3.40 ± 0.21
residual gaseous tritium at 10^{-8} mbar	$(2.50 \pm 0.36) \cdot 10^{-6}$
detector noise (experimentally)	$(4.11 \pm 0.13) \cdot 10^{-3}$

3.2 Vacuum setup and sensor system

To control the measurement conditions in the recipient, the TRIADE vacuum setup and sensor system are used. It allows measurements in a parameter range of at least $p = 5 \cdot 10^{-9}$ mbar to 1.013 mbar and $T = -100°C$ to 200°C.

The recipient pressure is regulated with the vacuum setup shown in figure 3.5. Each connection was leak tested to less than 10^{-10} mbar $\cdot$ l/s. Gas samples can be expanded into the system via two sample ports, one of which is used exclusively for tritium samples. All connections between this port and the recipient, as well as the recipient itself are bakeable up to 200°C.

The measurement conditions are monitored with the sensor system. It comprises pressure and temperature sensors at several points of the setup. The pressure in the recipient is monitored with four sensors covering a pressure range of 10^{-10} mbar to 10^{3} mbar. In the range of 10^{-10} mbar to 10^{-3} mbar, pressure monitoring relies on a gas species dependent cold cathode MKS 903[3]. calibrated on nitrogen. A MKS MicroVision Plus quadrupole mass spectrometer allows for gas species analysis at the outlet of the recipient. A photo of the setup is shown in figure 3.6.

3.3 Data acquisition and analysis

The BIXS spectra and mass spectra are both recorded using software of the manufacturer. The X-ray detector comes with DppMCA[4] from Amptek; the mass spectrometer is supplied with MKS Process Eye[5]. Both allow to control the measurement parameters, display the recorded data and save them to disk in their own file format.

The voltage signal of the pressure and temperature sensors is digitised using 14 and 16 bit analog digital changers (ADCs). This is read out with a LabVIEW[6] program and converted individually into units of pressure or temperature. The results are displayed for constant monitoring of the measurement conditions and logged to disk.

The analysis relies completely on Origin[7]. To match the BIXS spectra and sensor data, the analysis software for the investigation of adsorption (ASIA) was written in Origin C. ASIA identifies the measurement phases described in section 4.1 based on the pressure in the recipient. Spectra taken during certain measurement phases can thus be evaluated exclusively. The results are presented in the following chapter.

[3] Inverted Magnetron Transducer (IMT) cold cathode ionisation vacuum sensor MKS 903

[4] Amptek, Inc.: *DppMCA Digital Acquisition Software*, Version 1.0.0.11, 1998-2012

[5] MKS Instruments Spectra Products: *Process Eye Professional, Easy View AddIn*, Version 5.71.0.1000, 1999-2003

[6] National Instruments: *LabVIEW*, Version 8.5.1, 2008

[7] OriginLab Corporation: *OriginPro*, Version 9.1 Sr3, 1991-2014

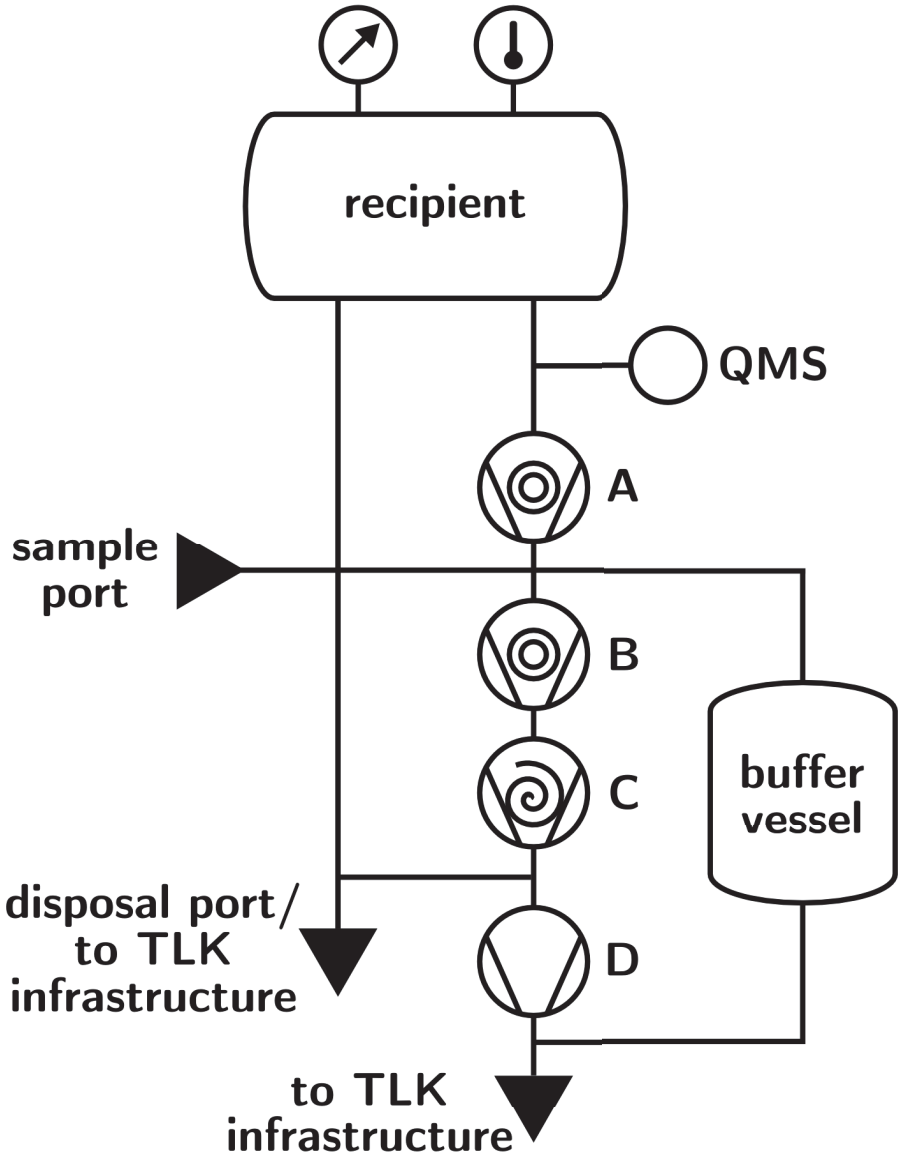

Figure 3.5: Simplified diagram of the TRIADE vacuum setup. Tritium gas can be inserted via the sample port and be expanded directly into the recipient. The connections to the recipient as itself can be baked up to 200°C.
During measurements, the recipient can be locked up by valves on both sides of it. Valves are not included in this diagram as are most of the sensors. Pressure and temperature sensors exist in the recipient to monitor measurement conditions. At the outlet of the recipient, gas species composition can be determined with a Quadrupole Mass Spectrometer (QMS).
To evacuate the recipient, two turbo molecular pumps (A and B) and a scroll pump (C) are cascaded. The ultimately reachable pressure in the recipient is at least $5 \cdot 10^{-10}$ mbar. A metal bellows type pump (D) is used to store system gas in the buffer vessel. It is also used for gas disposal to the infrastructure of the TLK. Alternatives include a disposal port, by which also atmospheric air can be inserted into the recipient.
For further details about the TRIADE vacuum setup, see [Sch13].

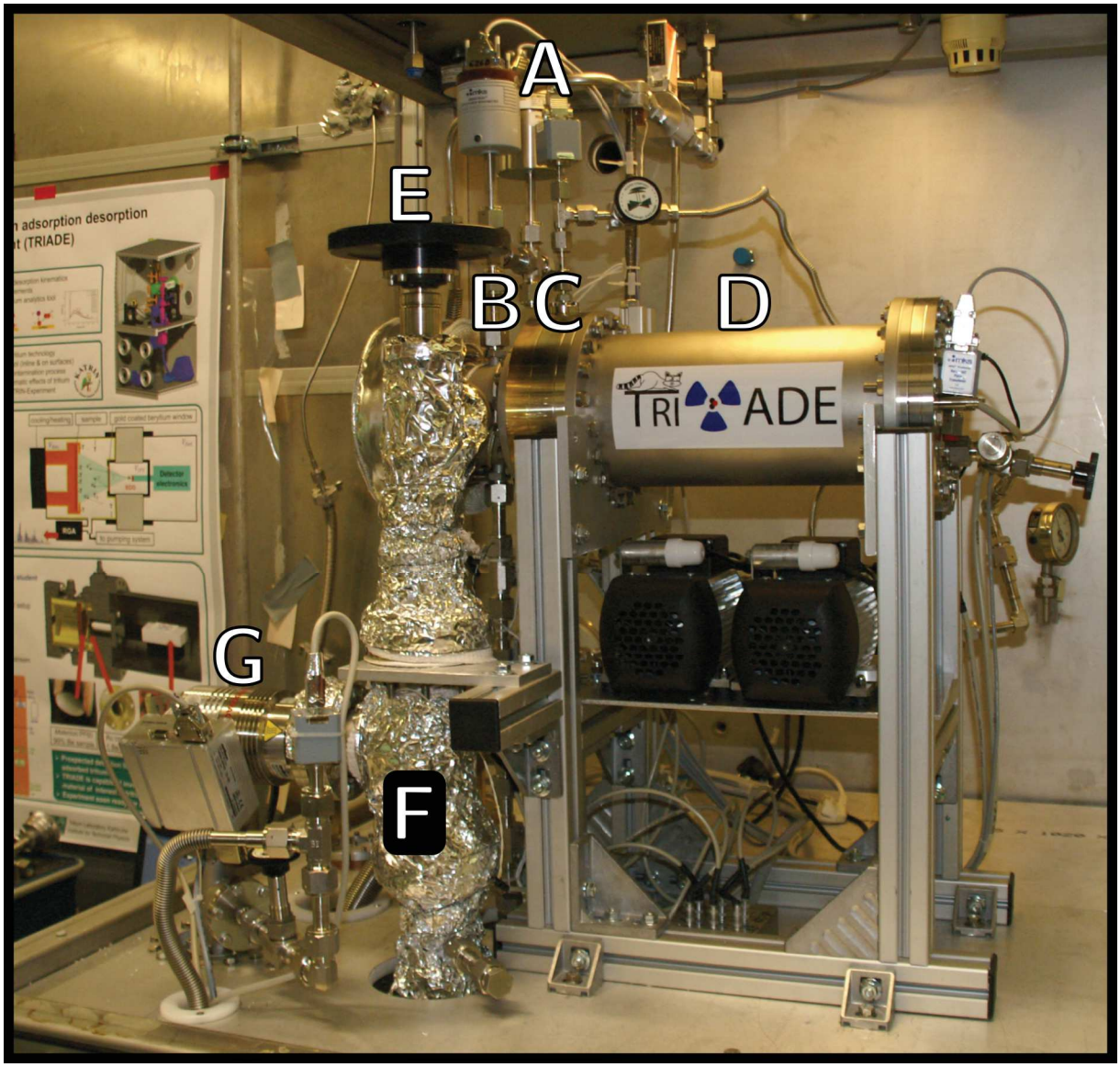

Figure 3.6: Photo of the TRIADE setup. It shows the upper part of the glove box, the experiment is located in. The most important visible components are: (A) the pressure instrumentation of (B) the recipient, (C) the mid flange volume with the detector, (D) the volume of the detector electronics, (E) the valve between recipient and vacuum pumps, (F) the volume of the Quadrupole Mass Spectrometer (QMS) and (G) the first of the two cascaded Turbo Molecular Pumps (TMP). The sample port can not be seen in this photo. In the lower part of the box are the second TMP, the scroll pump, the metal bellows type pump, the buffer vessel and the electronics of the QMS. The photo was taken by Fabian Schneck during the assembling of the experiment before the box setup was closed.

4 Investigation of tritium adsorption on gold coated beryllium

The TRIADE setup was used to investigate tritium sorption on gold coated beryllium. To this subject, four specific questions have been raised in section 1.6:

- Does tritium adsorb on a sample of gold coated beryllium?
- If so, which is the saturation coverage?
- After which time is the saturation coverage reached?
- In case of adsorption, how can the sample best be decontaminated?

Five measurement campaigns have been performed to answer these questions. The measurement procedure is described in section 4.1. The systematic and statistic uncertainties are discussed in section 4.2. Evidence for tritium adsorption is reported in section 4.3. The saturation coverage is determined in section 4.4. Section 4.5 investigates the time dependence of tritium adsorption on the sample. The decontamination of the sample after the measurements is treated in section 4.6. Section 4.7 summarises and discusses the results, including the consequences for the KATRIN experiment.

Table 4.1: Key parameters of the five measurement campaigns. Campaigns c4.1 and c4.2 were performed on consecutive days. In repeated runs, the sample was exposed to tritiated gas at a nominal exposure pressure p_{exposure}.

date	7.8.14	27.8.14	16.9.14	29.10.14	30.10.14
campaign	c1	c2	c3	c4.1	c4.2
number of runs	17	15	15	15	12
p_{exposure} (mbar)	$5 \cdot 10^{-5}$	$5 \cdot 10^{-5}$	$1 \cdot 10^{-3}$	$1 \cdot 10^{-3}$	$1 \cdot 10^{-3}$

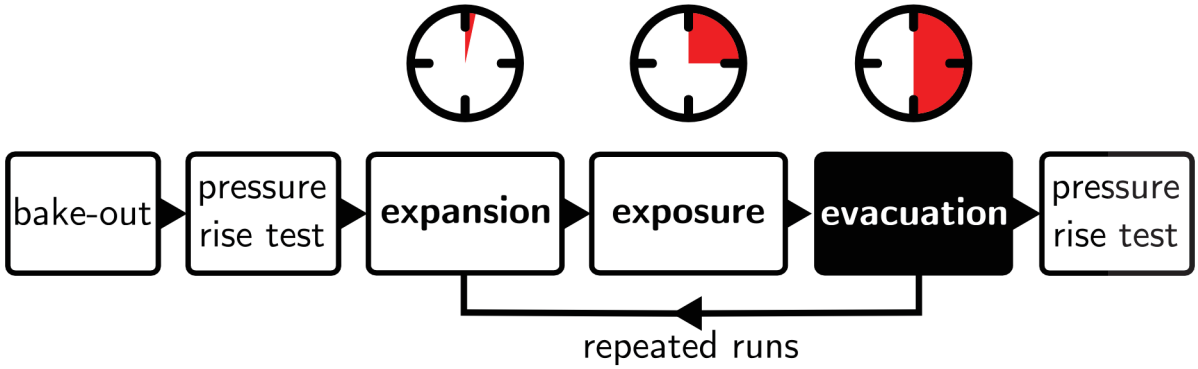

Figure 4.1: Overview of the measurement procedure. Before each campaign, sample and recipient were decontaminated. This included a bake-out of at least five days at 200°C. Before and after each campaign, a pressure rise test was performed by closing up the recipient for about 20 min. After the initial pressure rise test, the background count rate of the BIXS system was determined. Each campaign consists of at least 12 repeated runs which in turn consist of three phases. First, tritiated gas is expanded into the recipient to the nominal exposure pressure. Then, the sample is exposed to the expanded gas for 15 min. Finally, the recipient is evacuated for 30 min. Without significant background from residual gas, the sample surface activity can be determined in this time with the BIXS method.

4.1 Description of the measurement procedure

The evaluation of tritium adsorption on gold coated beryllium in this chapter is based on five measurement campaigns. An overview of the campaigns is given in section 4.1.1. Section 4.1.2 describes the preparation of sample and recipient before each campaign. Before and after each campaign, a pressure rise test was performed, see section 4.1.3. The campaigns consisted of repeated runs, which were subdivided in three phases: expansion of the tritiated gas into the recipient (section 4.1.4); exposure of the sample to the tritiated gas (section 4.1.5); and finally evacuation of the recipient (section 4.1.6).

4.1.1 Overview of the measurement campaigns

Five measurement campaigns have been performed with TRIADE to investigate tritium adsorption on the gold coated beryllium sample. During each campaign, the sample was exposed repeatedly to tritiated gas at a nominal measurement pressure, see figure 4.1. Then, the activity on the sample was measured with the TRIADE BIXS system.

The campaigns were performed at two different measurement pressures: For the first two campaigns designated with c1 and c2, it was up to $5 \cdot 10^{-5}$ mbar. For the campaigns c3, c4.1 and c4.2, the nominal measurement pressure was $1 \cdot 10^{-3}$ mbar. All campaigns were

performed after a standardised measurement plan on a single day. The key parameters of the campaigns are summarised in table 4.1.

4.1.2 Measurement preparations

The tritiated gas for each campaign was obtained from the tritium purification facility CAPER[1] at the TLK. This ensures a high tritium concentration of the tritiated gas. An estimation of the tritium concentration is done in section 4.2.2. Up to the campaign, the tritiated gas was stored in a sample cylinder. The sample cylinder of 10 cm^3 was filled in case of c1, c2 at 1 mbar and in case of c3, c4 at 5 mbar. It was connected to the setup via a sample port. From there, the tritiated gas was expanded into the system on the measurement day.

Before each campaign, sample and recipient were decontaminated. This always included exposure to atmospheric air for at least 30 min with at least 40 mbar. A bake-out at 200°C was performed for at least five days. The temperature was chosen to remove water from the system. The baking time was minimised to avoid damaging the sample surface and so changing its adsorption behaviour [Lis87]. Bake-outs always included the connection between recipient and sample port. At least one day of bake-out was performed after the sample cylinder was connected. When the recipient was not baked or exposed to atmospheric air, it was evacuated constantly. The effectiveness of these decontamination methods will be compared in section 4.6. The final measurement conditions are investigated with a mass spectrometer in section 4.2.1.

4.1.3 Pressure rise tests before and after each campaign

Before and after each campaign, the recipient was closed up for about 20 min to perform a pressure rise. The leak rate and outgassing rate of the recipient can be determined from the pressure development, as discussed in section 4.2.3. However, also effects of adsorption and desorption were observed during the tests. The recipient pressure during all tests is displayed in figures D.1, D.2, D.3 and in figure 4.5. Both pressure rise test was performed before c1.

After the initial pressure rise test before each campaign, the BIXS background count rate was measured during a 2,000 s interval. In case of c1, the start point of the interval was chosen manually. The resulting background count rates will be shown in table 4.2. While the count rate rose only slightly from c1 to c3, it more than doubled after c3. This memory effect will be discussed in section 4.6.6.

[1] CAPRICE PermCat, with CAPRICE: Catalytic Purification Experiment

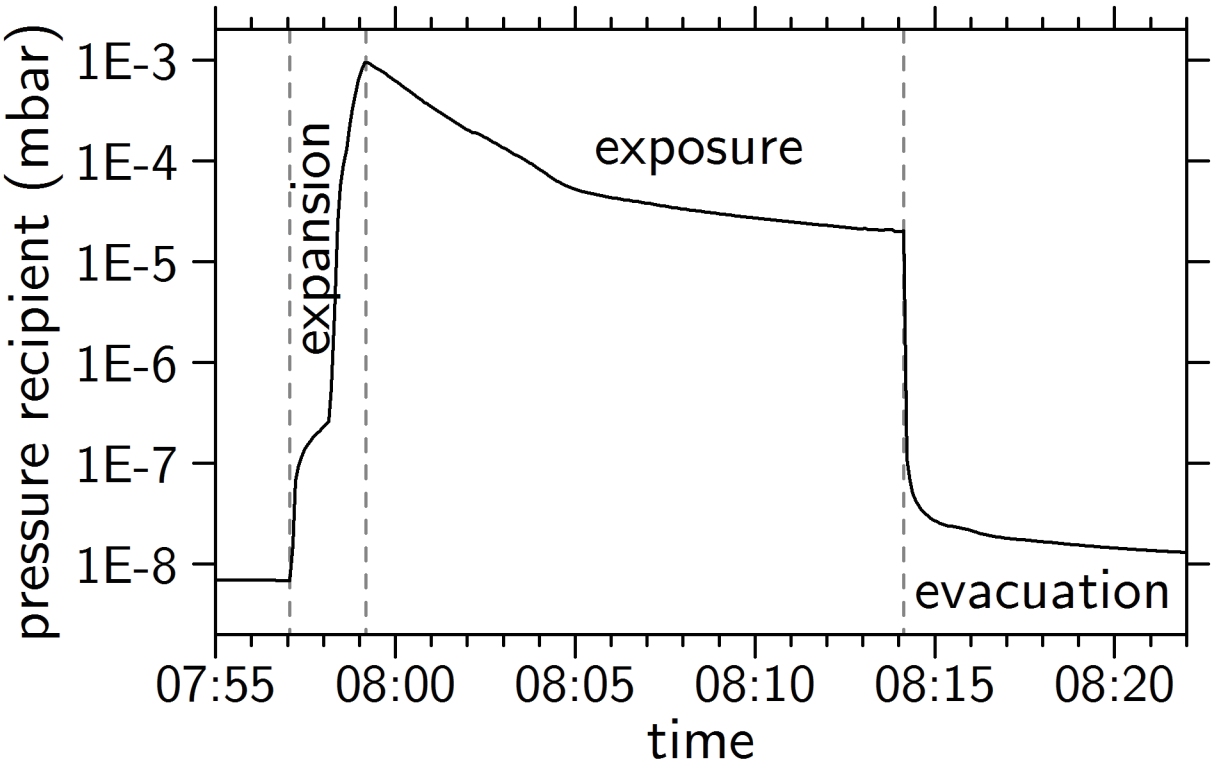

Figure 4.2: Recipient pressure during one measurement run consisting of expansion, exposure and evacuation. The graph displays the first run of campaign c4.1. Tritiated gas is expanded into the recipient. The kink of the pressure rise indicates the manual pressure regulation to the nominal peak pressure. The recipient is then closed and the sample is exposed to the tritiated gas for 15 min. During this time, the pressure decreases by several magnitudes. This is attributed to adsorption of tritiated gas on the inner recipient surfaces. The pressure decreases with at least two different slopes, which is attributed to adsorption on different surfaces. The final exposure pressure rises during certain campaigns. Finally, the recipient is evacuated for 30 min. In this time, the activity on the sample is measured with the BIXS system.

4.1.4 Expansion of tritiated gas into the recipient

At the begin of each run, the tritiated gas was expanded manually over a valve from the sample port into the recipient. A typical expansion phase is shown in figure 4.2. It shows a kink due to manual pressure regulation.

Also, the peak pressure of expansion varied due to the manual regulation. The nominal measurement pressure of campaigns c1 and c2 is $5 \cdot 10^{-5}$ mbar. The actual peak pressures ranged between $(4.5 \ldots 5.6) \cdot 10^{-5}$ mbar. In c1, the peak pressure of runs 1, 2 and 11 even reached pressures up to $9.1 \cdot 10^{-5}$ mbar. The nominal measurement pressure of c3 and c4 is $1 \cdot 10^{-3}$ mbar. The actual peak pressure lay between $(9.4 \ldots 10.7) \cdot 10^{-4}$ mbar. However, these values are based on measurements with the cold cathode ionisation vacuummeter. Its missing calibration on tritium is discussed in section 4.2.4.

Also due to the manual regulation, the expansion phase varied between 1 minute and 3 minutes. This adds to the exposure time, which was monitored with an accuracy of 1 min as described in the next section.

4.1.5 Exposure of the sample to the tritiated gas

The sample was exposed to the tritiated gas for about 15 min. During this time, the pressure decreased by several magnitudes as shown in figure 4.2. This is attributed to adsorption of the tritiated gas on the inner recipient surfaces. The strength of the decrease varied between campaigns and between runs as will be explained in section 4.4.1.

The nominal measurement pressure can not account for the change in the measurement conditions during exposure phase. For this reason, the dosage [Lüt97] is calculated which integrates over $p \cdot t$ for the whole measurement interval. The significance of the dosage is limited however due to the missing tritium calibration of the main pressure sensor. The effect of the pressure decrease on the measurement conditions will further be discussed in section 4.2.5.

4.1.6 Evacuation of the recipient and BIXS measurements

After the exposure phase, the recipient is evacuated for 30 min to about 10^{-8} mbar. This allows to measure the sample surface activity without significant background from residual gaseous tritium (see section 3.1.4).

Only spectra measured completely during the evacuation phase are regarded for the BIXS measurements of each run. The begin and end of the phase is determined by a threshold of 10^{-7} mbar from the recipient pressure. Additionally, a limit of 2,000 s after the begin of evacuation is set. This applies especially to the final pressure rise test. The net measurement times vary, however, as discussed in section 4.2.6.

4.2 Statistical and systematic uncertainties of the measurement data

Various sources of statistical and systematic uncertainties to the adsorption measurements have been identified. Most of them can be discussed only qualitatively.

The measurement conditions depend on the decontamination of the recipient before the campaign, as discussed in section 4.2.1. They also depend on the composition of the tritiated gas, see section 4.2.2. This composition might be altered during the exposure phase by leaked atmospheric air, see section 4.2.3. The exposure pressure is monitored with the main pressure sensor, which is not calibrated on tritium as explained in section 4.2.4. Nevertheless, it allows to observe a pressure decrease during the exposure phase in section 4.2.5. The BIXS measurement were influenced by variations of the measurement time (section 4.2.6) and detector noise peaks (section 4.2.7).

The influence of evacuation on the measurement campaigns will be discussed later on in section 4.6.2. Also, a memory effect over the course of the campaigns is discussed in section 4.6.6.

4.2.1 Measurement conditions: decontamination of sample and recipient

Before each measurement, the recipient is decontaminated by evacuation, bake-out and exposure to moist atmospheric air (see section 4.6). The effect of the decontamination methods can be judged by mass spectra of the residual gas in the recipient before each campaign. In all spectra, the by far dominant peak was from water. However, its partial pressure was found below 10^{-5} mbar for all campaigns. The initial exposure pressure were at least 10^{-5} mbar for all campaigns. Therefore, the residual water in the recipient is deemed negligible.

4.2.2 Tritiated gas: tritium concentration

The tritiated gas for the measurements was obtained from the CAPER[2] facility inside the TLK. The tritium concentration was measured two times from each gas, see appendix E. The tritium concentrations in table 4.2 are calculated as their arithmetic mean according to appendix C.1. This returned statistical uncertainties up to 5%, which is applied to all results. At this uncertainty, the minor correction for tritium decay with a half-life of 12.3 y [Dem10] was neglected.

[2]CAPRICE PermCat, with CAPRICE: Catalytic Purification Experiment

Table 4.2: Measurement conditions of the five measurement campaigns. For the tritium concentration C_{tritium} of the tritiated gas, see section 4.2.2. The nominal exposure pressure decreased over time. As an indicator of the actual measurement conditions, the dosage $p \cdot t$ [Lüt97] was calculated by integrating over the measurement pressure (see section 4.2.5). The BIXS background count rate was measured before the first run of each campaign. It shows a memory effect (see section 4.6.6). Based on the background count rate, the offset *Delta*mdl is calculated. Adding it to the background gives the limit for the count rate, above which tritium adsorption is detected with 95% probability. This limit is termed in this work the minimum detection limit mdl. The temperature is stable during each of the five campaigns. It is therefore not considered in the evaluation.

campaign	c1	c2	c3	c4.1	c4.2
number of runs	17	15	15	15	12
C_{tritium} (%)	94 ± 5	94 ± 5	77 ± 5	98^{+2}_{-5}	98^{+2}_{-5}
exposure pressure (mbar)	$5 \cdot 10^{-5}$	$5 \cdot 10^{-5}$	$1 \cdot 10^{-3}$	$1 \cdot 10^{-3}$	$1 \cdot 10^{-3}$
dosage $p \cdot t$ (mbar·h)	$(1.6 \pm 0.1) \cdot 10^{-4}$	$(9.1 \pm 0.8) \cdot 10^{-5}$	$(5.5 \pm 0.5) \cdot 10^{-3}$	$(7.7 \pm 0.7) \cdot 10^{-3}$	$(8.3 \pm 0.8) \cdot 10^{-3}$
BIXS background (cps)	0.77 ± 0.03	0.89 ± 0.02	0.97 ± 0.02	2.12 ± 0.04	5.35 ± 0.06
Δmdl	0.132 ± 0.005	0.107 ± 0.003	0.112 ± 0.003	0.188 ± 0.004	0.262 ± 0.003
mdl	0.90 ± 0.03	1.00 ± 0.02	1.08 ± 0.02	2.31 ± 0.04	5.60 ± 0.06
temperature T (°C)	33.3…34.0	32.3…32.9	32.4…32.9	32.0…32.4	32.0…32.7

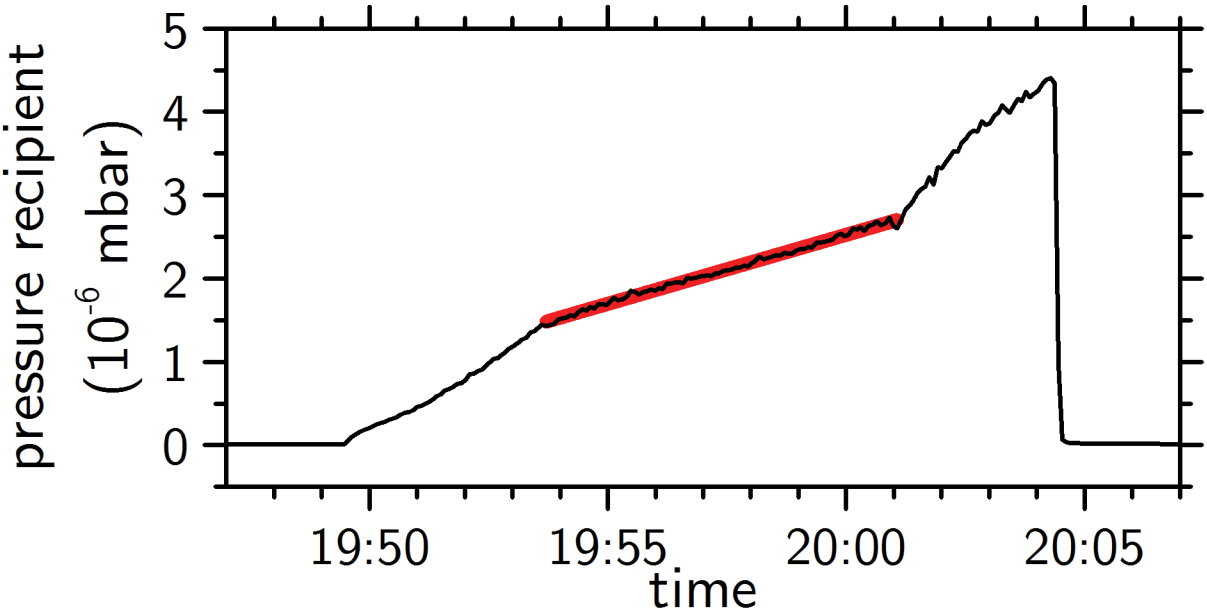

Figure 4.3: Determination of the leak rate from pressure rise test after campaign c1. The pressure inside the recipient first rises exponentially during the pressure rise test. No explanation can be given for this. It then rises linearly. A linear fit (red line) to the region returns a slope corresponding to a leak rate of $2.76 \cdot 10^{-9}$ mbar l/s. Afterwards, the pressure increases again exponentially towards a saturation value as expected from a desorption effect. The effect must have started after the begin of the pressure rise test, according to its slope.

4.2.3 Tritiated gas: leaked gas contribution during exposure phase

Before and after each campaign, a pressure rise test was performed for 20 min (see section 4.1.3) to determine the leak rate of the recipient. No test was performed before c1. A leak to the outside of the recipient can be recognized as a linear pressure rise. In most of the pressure rise tests, the pressure is dominated by adsorption and desorption effects as discussed in section 4.3.2. Therefore, no statement about the adsorption rate can be made from these tests.

A linear increase of the pressure was only observed during the test after c1, displayed in figure 4.3. The pressure shows exponential behaviour before and after the linear rise. This raises doubts about its origin from a leak. However, the fit of this pressure increase with Origin[3] returns a slope corresponding to a leak rate of $(2.76 \pm 0.02 \cdot 10^{-9}$ mbar l/s. The volume of the recipient is approximated with 1 l.

If not due to a leak, this value is an estimate for the maximum leak rate. It corresponds to the expectation, as each individual connection at the recipient was leak test to below $1 \cdot 10^{-3}$ mbar. It fulfills by far the requirements for the integral leak rate

[3]OriginLab Corporation: *OriginPro*, Version 9.1 Sr3, 1991-2014

of a primary system for tritium processing at the TLK[4]: this may not be more than $\leq 1 \cdot 10^{-8}$ mbar l/s.

However, such a leak influences the measurement conditions during the campaigns. At the end of the 900 s long exposure phase, $2.49 \cdot 10^{-6}$ mbar atmospheric air has entered the recipient. At the end of the exposure phase of the campaigns c1 and c2, the recipient pressure is of the same magnitude, see figure 4.8. The leaked air then contributes up to 100% of the gas, the sample is exposed to. Water from the air interacts with adsorbed tritium by isotope exchange effects [Nis92] and removes it. Also, water adsorbs on the sample surface. It incorporates adsorption sites, decreasing the saturation value of tritium adsorption. However, it might even increase adsorption of tritium by isotope exchange of adsorbed water and gaseous tritium. Thus, the effect of adsorbed water is unknown and impairs the measurements of campaigns c1 and c2.

For campaigns c3, c4.1 and c4.2, the final exposure pressure lies always 10^{-5} mbar (figures 4.9 and 4.10). It even lies above 10^{-4} mbar from run 7, 5 and 1 onwards, respectively. But still here, the contribution from atmospheric air is about 10% during the first runs. Thus, an effect on the tritium adsorption measurements of campaigns c3, c4.1 and c4.2 is not excluded either.

4.2.4 Main pressure sensor: repeatability, gas correction factor for tritium

The recipient pressure below 10^{-5} mbar relies on the cold cathode MKS 903 (see section 3.3). The repeatability for the MKS 903 is specified in its manual as about 5%. Further, the MKS 903 is calibrated on nitrogen. For most considerations, the measured pressure values are displayed and discussed unprocessed in this work. To consider absolute pressures of other gases, the measured value must be corrected with a gas correction factor (see section B.4). This is required for the dosage.

4.2.5 Exposure pressure: decrease during exposure phase, calculation of the dosage

The 15 min duration of the exposure phase was monitored with an accuracy of 1 min. Always, the expansion phase of 1 min to 3 min added to the exposure time. In case of run 8 of campaign c1, the exposure phase lasted only about 7 min. These variations cause unequal conditions during the runs for adsorption on the sample. An indicator of the real measurement conditions is the dosage $p \cdot t$ [Lüt97]. In this evaluation, it is calculated

[4] *Technische Liefer- und Abnahmebedingungen, TLA-Nr. 01, Ausgabe - Nr. 11*, tritium laboratory Karlsruhe at the KIT, 2014

by integrating the pressure $p(t)$ inside the recipient during exposure phase from t_0 to t_1:

$$\text{dosage} = \int_{t_0}^{t_1} p(t)\ \mathrm{d}t. \tag{4.1}$$

Because no gas correction factor for tritium exists, the value is interpolated from those for deuterium and helium. The arithmetic mean of both factors and its statistical uncertainty are calculated according to appendix C.1. The result is:

$$c = 0.265 \pm 0.112\ \text{stat.} \tag{4.2}$$

By this correction factor, the dosage obtained from integrating the pressure of each individual run is divided. Its uncertainty is estimated by the borders of the interpolation interval. This systematic uncertainty is combined with the 5% uncertainty from repeatability according to appendix C.2.

The total dosage of each campaign displayed in table 4.2 is obtained by adding up the dosage of the individual runs. Their systematic errors are added quadratically. The average dosage for the runs in campaigns c3, c4.1 and c4.2 is calculated as the arithmetic mean of the individual runs. Their statistical (appendix C.1) and systematic (appendix C.2) uncertainties are added quadratically. This results in the average dosage:

$$\text{average dosage}_{\text{c3,c4.1,c4.2}} = (5.1 \pm 3.0) \cdot 10^{-4}. \tag{4.3}$$

As described in section 4.1.5 and seen in figure 4.2, $p(t)$ decreases during the exposure phase. It does so by about one magnitude and even by about two magnitudes at the beginning of c3 and c4.1. The final exposure pressures can be seen in figures 4.8, 4.9 and 4.10. For c3, c4.1 and the begin of c4.2, they rise constantly. This implicates a systematic shift of the measurement conditions which can not be quantified, however.

Also the peak pressure of expansion phase varies, as mentioned in section 4.1.4. However, the variation is less than a factor 2. This is deemed negligible compared to the pressure decrease over several magnitudes during exposure phase.

4.2.6 BIXS measurements: calculation of the BIXS count rates, variation of the measurement time, minimum detection limit

The measurement procedure of the BIXS count rates is described in section 4.1.6. Figure 4.4 shows the spectra measured after the initial pressure rise tests of campaigns c1 to c4.1. They deviate only in their intensity while showing the same features otherwise. Therefore,

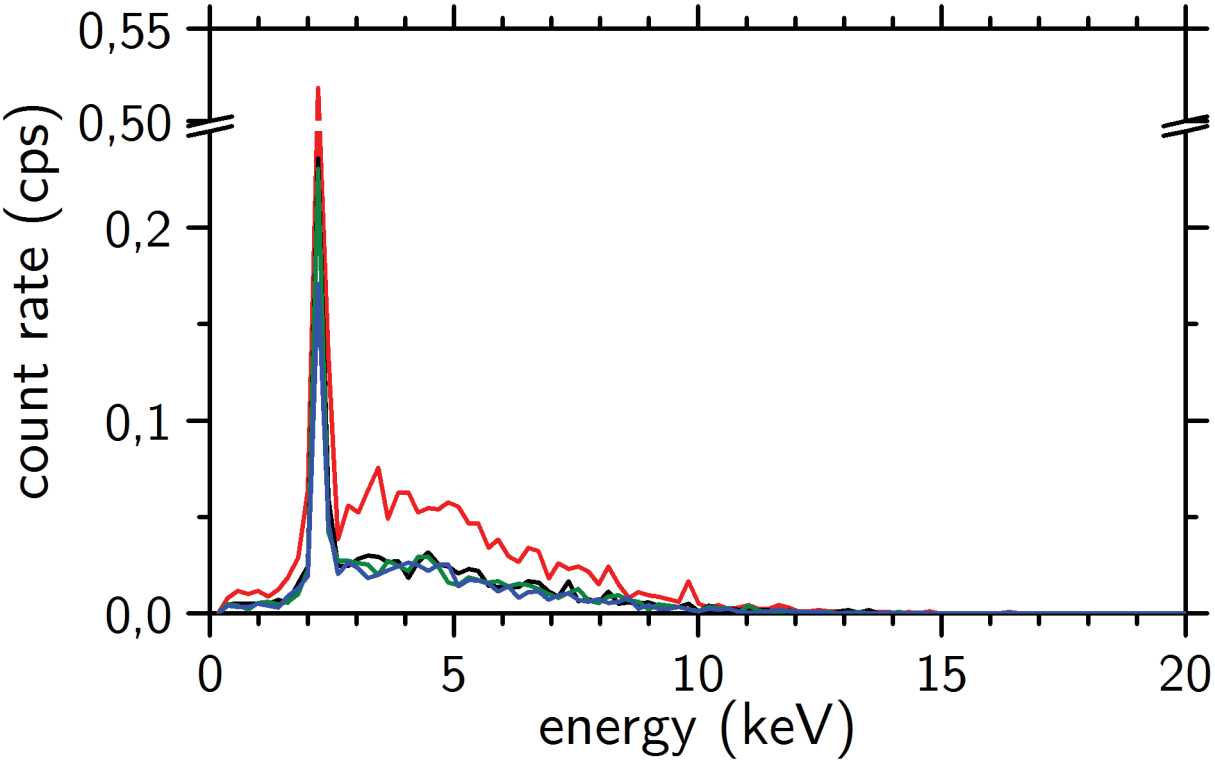

Figure 4.4: BIXS spectra before the start of the measurement campaigns. The spectra were taken during about 30 min after the initial pressure rise tests of c1 (blue), c2 (green), c3 (black) and c4.1 (red). They are normalized to their measurement time and binned to 100 bins.
The spectra show continuous Bremsstrahlung and a characteristic X-ray peak. It is attributed to the gold M5N7 line at 2.1 keV [Sol07] from the gold coating of sample and window. The spectra deviate only in their intensity while showing the same features otherwise. This applies to all BIXS measurements in all campaigns. Therefore, only the total count rate is considered in the evaluation. The total count rate of the displayed spectra is the BIXS background count rate given in table 4.2.

only the integrated number of counts N is considered. With the measurement time t, the BIXS count rate is:

$$\text{count rate} = \frac{N}{t}. \tag{4.4}$$

Although a measurement interval was defined during evacuation phase, the net measurement time varied. This is because spectra not lying completely inside the measurement interval were completely excluded. Also, variations arise from manual regulation of the evacuation phase and measurement time for a single spectrum. Due to operator errors, the measurement time was further reduced in case of c3 run 15, c4.1 run 6 and c4.1 run 11. The actual measurement times are given in table D.1.

During evacuation, the activity of the sample surface decreases as will be estimated in section 4.6.2.2. The decreases are estimated as < 0.055 cps for c1 and < 0.073 cps for c3.

An effect by the unequal distribution of the measurement time inside the measurement interval is therefore deemed negligible.

However, variations of the BIXS measurement time influence the statistical uncertainty of the count rates. The uncertainty of $\Delta N = \sqrt{N}$ is assumed Poisson distributed [Cow98]. The measurement time t is assumed to be known without uncertainty. With Gaussian error propagation from appendix C.2 follows the uncertainty of the count rate cr:

$$\Delta\text{count rate} = \frac{\sqrt{N}}{t}. \tag{4.5}$$

The significance of the BIXS measurements with respect to tritium adsorption can be statistically quantified. A measurement can be excluded at 95% probability to be caused by a fluctuation of the background N_B above a threshold N_D [Kno10]:

$$N_D = 4.65 \cdot \sqrt{N_B} + 2.71. \tag{4.6}$$

As $\Delta N = \sqrt{N}$ is assumed, $\delta_{N_D} = 4.65$ is constant. N_D is calculated for each campaign and divided by the measurement time t for comparison with other count rates. The comparability of the normalised results is approximately fulfilled by the comparable measurement intervals. This returns the minimum detectable increase of the count rate Δ mdl. The value is added to the measured count rate to receive the count rate threshold for the detection of adsorption. The threshold is termed minimum detection limit mdl in this work. The results are displayed in table 4.2. All uncertainties are calculated with Gaussian error propagation according to appendix C.2.

4.2.7 BIXS measurements: detector noise

The X-ray detector used for the BIXS measurements (see section 3.1.2) has a very low noise level. However, a noise edge appears at low energies which is eliminated by an energy threshold. The final threshold was set to 2% of the spectrum. With the calibration given by equation 3.2, this corresponds to an energy of 0.37 ± 0.06 keV. Its influence can be estimated from figure 4.4: only a vanishing fraction of the Bremsstrahlung continuum is expected below the threshold.

However, runaway results were found to be caused by noise appearances even above this threshold. The affected spectra were excluded from evaluation. But aside from those noise appearances, smaller noise events may have stayed unnoticed and unaccounted for. However, noise events are expected to be distributed randomly and to have no systematic influence on the measurement results.

4.3 Evidence for tritium adsorption

The five measurement campaigns described in section 4.1 allow for the investigation of tritium adsorption on gold coated beryllium. Evidence for tritium adsorption on the inner recipient surfaces during exposure phase is stated in section 4.3.1. The desorption of this previously adsorbed tritium is investigated in section 4.3.2. Tritium adsorption on gold coated beryllium is investigated with the BIXS system in section 4.3.3.

4.3.1 Evidence from pressure during exposure phases

The pressure in the recipient during the exposure phase of each run was observed to decrease. Figure 4.2 showed exemplary a logarithmic plot of the pressure during run 1 of campaign c4.1. The observed pressure decrease can only be caused by tritium adsorption on the inner surfaces of the recipient.

Section 1.3 introduced a comprehensive model for the coverage of a surface. It includes adsorption and desorption by the Langmuir-Hinshelwood and Eley-Rideal mechanism. The individual sorption laws were observed experimentally for hydrogen on gold. However, they are supported by basic considerations about sorption in section 1.2.4. The model predicts an approximately exponential increase of the coverage, if the initial coverage lies below the equilibrium value.

A model for the time dependence of the surface coverage θ was introduced for hydrogen on thin gold surfaces in section 1.3. The tritiated gas is expected to adsorb similar to hydrogen. The inner surfaces of the recipient are not exclusively gold coated. However, the model is adopted for an expectation about the time dependence of the pressure in the recipient.

The pressure inside the recipient is proportional to the density of the recipient gas [Dem06] and thus to the number of particles in the gas phase. Adsorption reduces the number of gas particles by increasing the surface coverage. Therefore, the model from section 1.3 for the coverage corresponds to the inverse shape of the observed pressure decreases. Two different slopes indicate the adsorption on the two main surfaces inside the recipient during adsorption phase: gold coated steel and stainless steel.

4.3.2 Evidence from pressure during pressure rise tests before and after the campaigns

Before and after each campaign, a pressure rise was performed to determine the leak rate of the system. For this purpose, the recipient was closed and the pressure development was observed. However, the linear rise expected from a leak to the outside was not observed most of the times. Instead, pressure rises and decreases were observed which

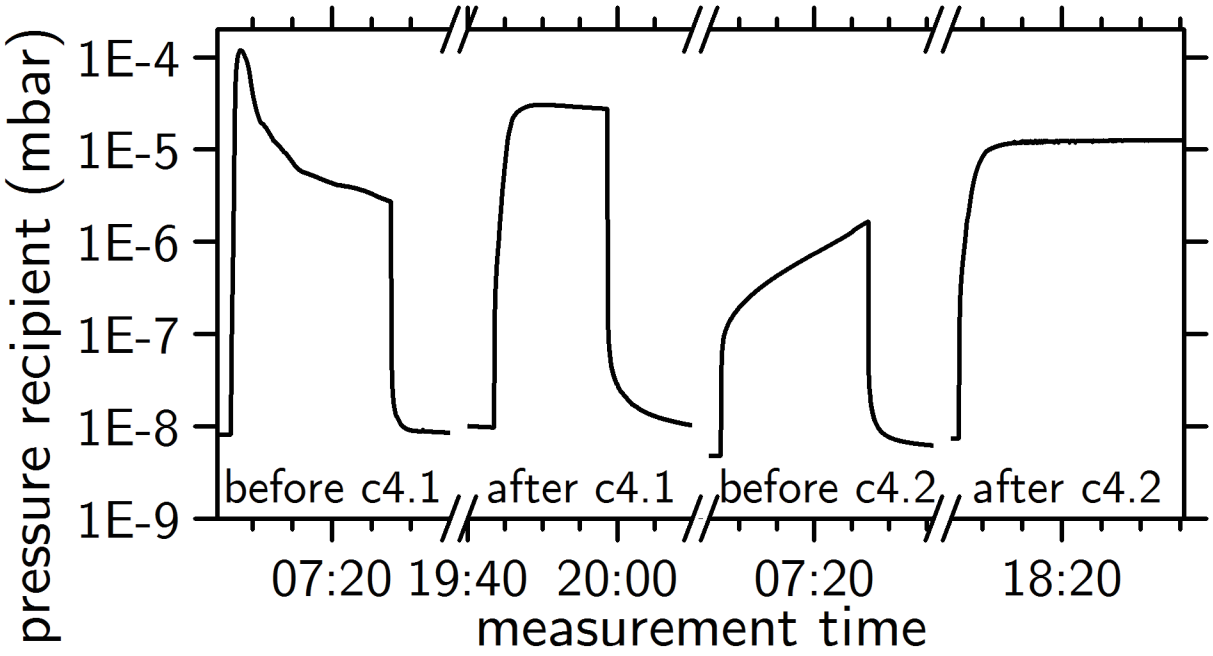

Figure 4.5: Pressure rises during closed recipient before and after campaigns c4.1 and c4.2. Those campaigns were performed on consecutive days. The pressure development was always dominated by adsorption and desorption effects.
Before campaigns, pressure decreased strongly during the tests due to adsorption on the system walls. This was the case before c4.1, too. During the tests after the campaigns, the decrease due to adsorption was much slower. This can be observed for the tests after c4.1 and c4.2. The slower adsorption is reasonable, as the system surfaces are expected to be almost saturated from the campaign. The test before c4.2 was performed after one night of evacuation after c4.1. Correspondingly, it showed much slower exponential pressure increase from desorption. The different slopes of the exponential increase and decrease of pressure can be explained by the model adopted in section 4.3.1.

were attributed to adsorption and desorption effects. The tests from campaigns c1, c2 and c3 are displayed in figures D.1, D.2 and D.3 in the appendix. Figure 4.5 shows the pressure during the tests before and after c4.1 and c4.2.

During the test before c4.1, the pressure rose sharply at the beginning but decreased in the later course of the test. A pressure decrease is only possible due to adsorption on the system walls. The initial increase must then be attributed to desorption from the system surfaces. A leak to the outside could not be compensated by the observed adsorption to the inner recipient surfaces. The tests before c2 and c3 showed a similar pressure development.

The development of the pressure can be understood as follows: The coverage on each surface inside the recipient tends to equilibrium with the gas phase. This equilibrium depends e.g. on the surface material, the surface coverage, the adsorbed gas species and the gas pressure. On different surfaces, different sorption processes occur. Each process has

anther time dependence and intensity. As all surfaces are connected by the same gas phase, the sorption processes lead to a characteristic pressure development.

However, the influence of the surface coverage and the adsorbed gas species are expected to change because of the campaigns. Consequently, different characteristic pressure developments should occur afterwards. This is just what was observed. This, too, indicates the adsorption of tritium on the inner recipient surfaces during the measurement campaigns.

4.3.3 Count rate development during campaigns

The previous sections showed evidence for adsorption of the tritiated gas on the inner surfaces of the TRAIDE setup. The adsorption of tritium on the sample can be investigated with the BIXS system. Those measurements were described in section 4.1.6. Figure 4.6 shows the measured count rates for campaigns c1, c2, c3 and c4.1. The error bars indicate only the statistical uncertainty from the measurement time. For their calculation as well as for systematic influences on the measurement, see section 4.2.

All campaigns displayed in figure 4.6 consist of at least 15 runs and one measurement of the BIXS background count rate. It was measured after the initial pressure rise test (see section 4.1.3) and before the first run. The background rises over the course of the campaigns due to a memory effect discussed in section 4.6.6.

The count rate is observed to rise during all campaigns. This only be caused by adsorption of radioactive tritium in the field of view of the detector. Due to the measurement principle of the TRIADE BIXS setup (see section 3.1.3), this concerns only two surfaces: on the sample and on the X-ray transparent window. Both consist of gold coated beryllium. Hence, tritium adsorption on gold coated beryllium is observed.

Compared to campaigns c1 and c2, the count rate is observed to rise faster in c3 and c4.1. This is attributed to the different nominal exposure pressures (see section 4.1.5): It was $5 \cdot 10^{-5}$ mbar for c1 and c2, but $1 \cdot 10^{-3}$ mbar for c3 and c4.1. This confirms the expected pressure dependence of tritium adsorption on gold coated beryllium.

Those were the first tritium adsorption measurements with TRIADE, allowing first statements about its systematics. The count rates of campaigns c1 and c2 rise around a linear mean with very small deviations. This indicates the stability of the measurements, which is further discussed in section 4.6.2. Also, the count rate development of campaigns at the same measurement pressure coincides very well. Putting aside the memory effect between campaigns, the measurements are found to be reproducible.

Minimum detection limits for the adsorption of tritium were calculated in section 4.2.6. They indicate the count rate at which a measurement can be excluded to be caused by fluctuations at 95% probability. The minimum detection limit for campaigns c1 and c2 are $\mathrm{mdl}_{c1} = 0.90 \pm 0.03$ cps and $\mathrm{mdl}_{c2} = 1.00 \pm 0.02$ cps. In these both campaigns, the

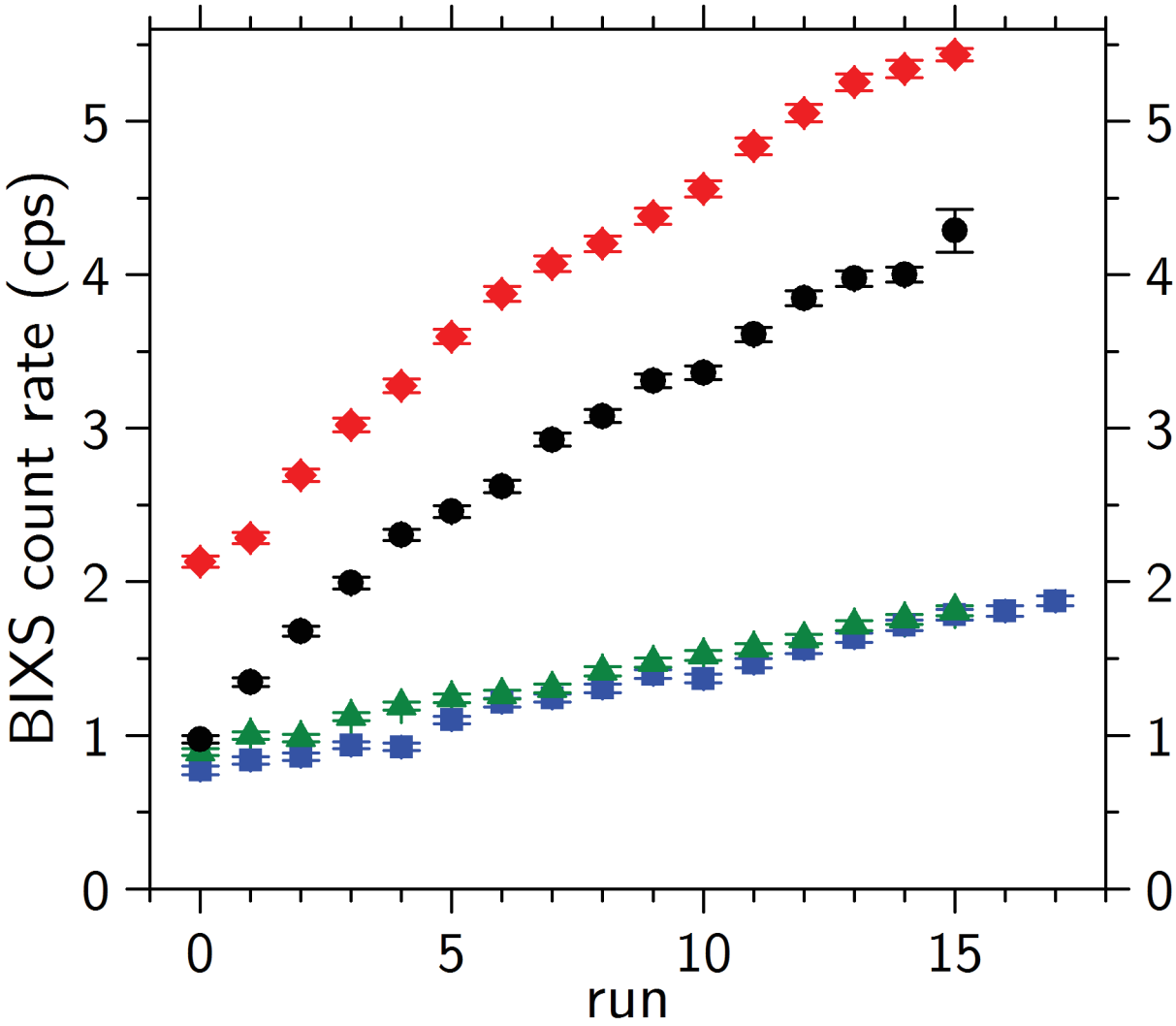

Figure 4.6: BIXS count rate development on a single measurement day. The figure displays campaigns c1 (blue squares), c2 (green triangles), c3 (black dots) and c4.1 (red diamonds).
Run 0 depicts the BIXS background count rate. It rises over the course of the campaigns as a result of a memory effect (see section 4.6.6).
During each run, the sample was exposed to the tritiated gas for about 15 min (see section 4.1.5). In c1 run 8, exposure lasted only about 7 min. The nominal exposure pressure for c1 and c2 was $5 \cdot 10^{-5}$ mbar. For c3 and c4.1, it was $1 \cdot 10^{-3}$ mbar. The count rates were measured during evacuation of the recipient (see section 4.1.6). The error bars indicate only statistical uncertainties (see section 4.2.6). Besides the detector counts, the uncertainty depends on the measurement time which deviates around 1600 s.
The count rate rises stable over the course of each campaign. Aside from the memory effect, the count rate development of c1 and c2 coincide. Also, the count rates of c3 and c4.1 with a higher nominal exposure pressure coincide. Thus, the measurements are reproducible. They further prove tritium adsorption on gold coated beryllium. The sample and X-ray transparent window consist of this window. Due to the measurement principle of the TRIADE BIXS setup, they contribute dominantly to the BIXS count rate (see section 3.1.3).

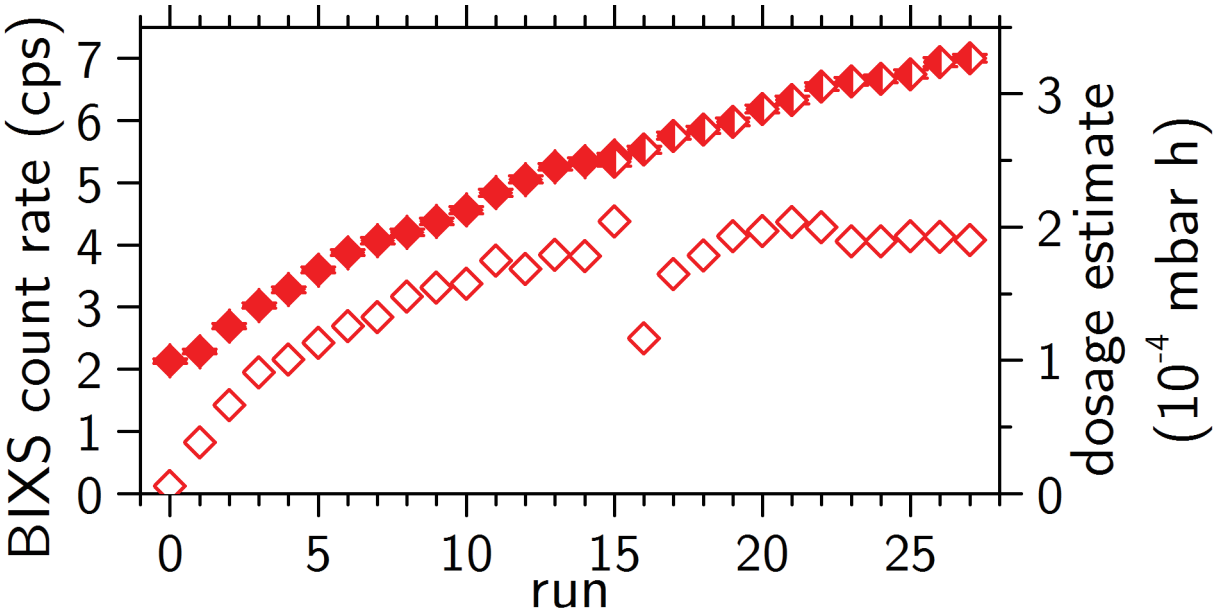

Figure 4.7: BIXS count rate development on consecutive days with estimate of the dosage. The figure displays the BIXS count rates of c4.1 (filled diamonds) and c4.2 (half filled diamonds). The error bars indicate only statistical uncertainties (see section 4.2.6). Run 0 depicts the BIXS background count rate of c4.1. The background of c4.2 is drawn together with run 15. It decreased due to decontamination from evacuation over night (see section 4.6.2.1). Run 16 corresponds to the first run of c4.2. The empty diamonds estimate the dosage, displayed without gas correction factor (see section 4.2.5). An influence of the dosage on the count rate is excluded for run 12 onwards. BIXS count rate and dosage are shown for c3 in figure D.7.

count rates rise to $\mathrm{cr}_{\mathrm{c1}} = 1.88 \pm 0.03$ and $\mathrm{cr}_{\mathrm{c2}} = 1.81 \pm 0.03$. Therefore, tritium adsorption is observed with more than 95% probability. The same can be stated for c3, c4.1 and c4.2 with the minimum detection limits from table 4.2 and figure 4.7.

Figure 4.7 shows the BIXS count rate and an estimate of the dosage for campaigns c4.1 and c4.2. The count rate shows a shift between run 15 of c4.1 and the background determined before c4.2, also drawn at run 15. More striking is its obvious correlation to the dosage which also increases during the campaign. The is due to the increase of the final exposure pressure discussed in the next section. It can not be excluded that the rise of the dosage is the cause for the rise of the count rate at the begin of the one day campaigns. A quantitative analysis is not possible: this would require to know the equilibrium pressure corresponding to each coverage of the sample. However, an influence of the dosage can be neglected for the most of combined campaigns c4.1 and c4.2: although the dosage dropped in run 12 and run 16, the count rate increased. Also, the count rate continued to rise during the last five runs of c4.2 though the dosage was almost stable.

During none of the campaigns the BIXS count rate reached a constant saturation level. A quantitative analysis of saturation effects is investigated in the following.

4.4 Determination of the saturation coverage

Tritium adsorption on gold coated beryllium inside TRIADE was reported in the previous section. Saturation effects are searched in the pressure data in section 4.4.1. For the BIXS count rates, a saturation amplitude is derived in section 4.4.2 based on a model for adsorption.

4.4.1 Saturation of adsorption on the recipient surfaces

Adsorption of the tritiated gas on the surfaces of the recipient was already stated in section 4.3.1. Besides gold coated beryllium, these surfaces consist mainly of stainless steel and gold coated steel. Due to adsorption, the pressure inside the recipient was found to decrease exponentially during exposure phase. It approaches a saturation pressure for each run of every campaign. This suggests the occurrence of a saturation effect also for adsorption on the gold coated beryllium sample.

Searching for a saturation effect over the course of each campaign, the pressure during exposure phases is compared. The pressure decrease at the begin of an exposure phase is always steeper than at the end of the previous one. This is attributed to decontamination of the recipient surfaces because of the evacuation phase (see section 4.6.2.2). This hampers the search for a saturation effect in the development of the exposure pressure over the course of a campaign. As a measure of the equilibrium pressure, the final exposure pressure p_{fep} is considered. As the exposure phase lasted about 15 min, it was chosen as the recipient pressure 850 s after the expansion peak of each run. As the exposure phase of c1 run 8 lasted only about 7 min, its p_{fep} was excluded from this consideration.

Figure 4.8 shows p_{fep} for the runs of c1 and c2 measured at $5 \cdot 10^{-5}$ mbar. No distinct trend over the course of either campaign can be observed. In other words, adsorption during the exposure phase of each run leads always to the same equilibrium pressure. Thus, the evacuation phase almost completely decontaminates the inner recipient surfaces which are dominated by stainless steel and gold coated steel. The BIXS cont rate increases during c1 and c2 though, as shown in figure 4.6. This shows that desorption under evacuation is slower from gold coated beryllium than from other surfaces inside the recipient.

Figure 4.9 shows p_{fep} for the runs of c3 and c4.1 measured at $1 \cdot 10^{-3}$ mbar. The p_{fep} is found to rise almost linearly over the course of both campaigns. Here, the inner surfaces of the recipient of stainless steel and gold coated steel were not completely decontaminated during the 30 min of evacuation. Therefore, an inventory is building up on the recipient surfaces. However, no saturation effect can be observed during the measurements of a single day.

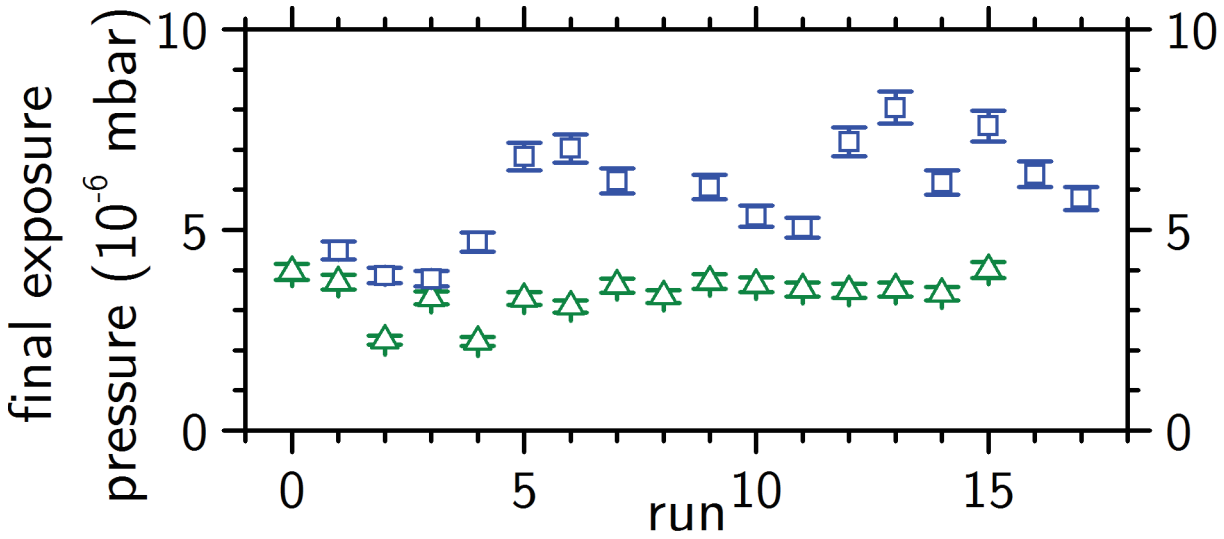

Figure 4.8: Final exposure pressure in the recipient during campaigns c1 (blue squares) and c2 (green triangles). The pressure was measured 850 s after the expansion peak to $5 \cdot 10^{-5}$ mbar. The displayed uncertainty is the repeatability of the pressure sensor. The pressure for run 0 was measured before run 1. No initial pressure rise test was performed before c1. The exposure phase of c1 run 8 lasted less than 850 s. No trend of the final exposure pressures is visible due to decontamination of the recipient during evacuation phase.

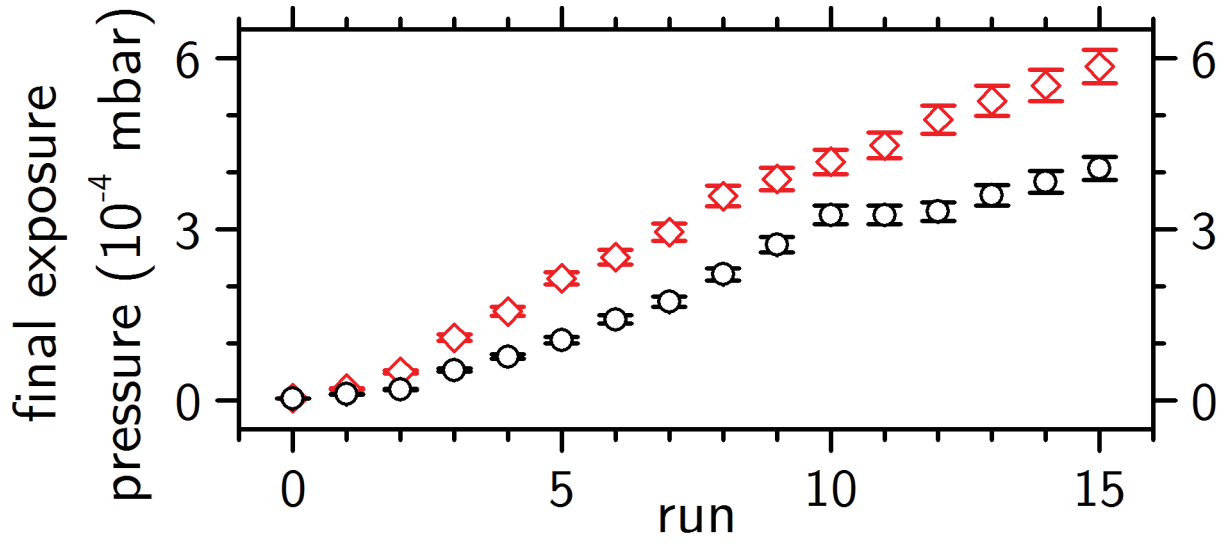

Figure 4.9: Final exposure pressure in the recipient during campaigns c3 (black circles) and c4.1 (red diamonds). The pressure was measured 850 s after the expansion peak to $1 \cdot 10^{-3}$ mbar. The displayed uncertainty is the repeatability of the pressure sensor. The pressure for run 0 was measured before run 1. No physical meaning is attributed to the runaway value in c3 run 10. The final exposure pressure rises during both campaigns. This indicates a saturation in the adsorption process on the inner recipient surfaces.

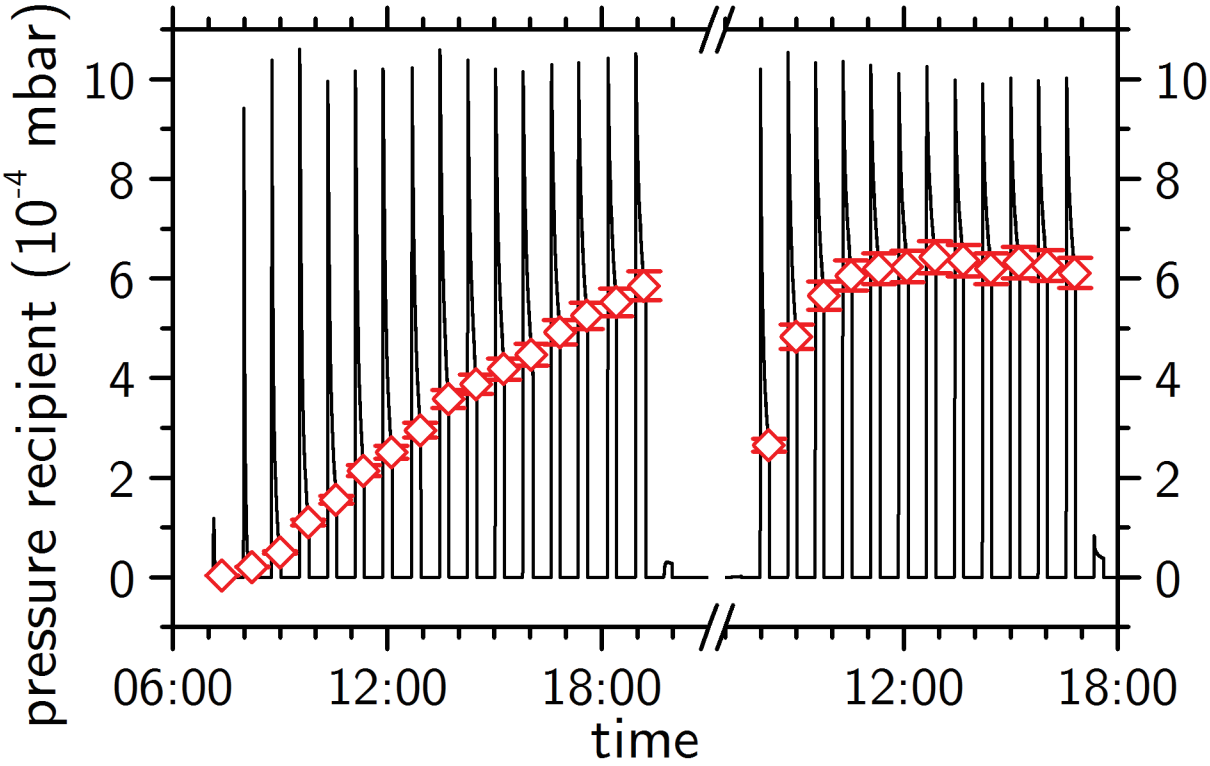

Figure 4.10: Final exposure pressure in the recipient during campaigns c4.1 and c4.2. C4.1 was performed on the first day (left), c4.2 on the following (right). The pressure during the campaigns shows characteristic peak from expansion and exposure during each run (black line). Also visible are the pressure rise test before and after both campaigns. The pressure 850 s after the expansion peak of each run is drawn as red diamonds. It is also drawn for the pressure rise test before c4.1. The uncertainty displayed by the error bars is derived from the repeatability of the pressure sensor. On the second day, the final exposition pressure rises faster and with an exponential shape compared to the linear rise of c4.1. It also reaches a stable limit. This indicates an equilibrium between adsorption and decontamination effects from the run procedure

Figure 4.10 shows p_{fep} for the runs of c4.1 and c4.2 on two consecutive days. The recipient was evacuated over night, decontaminating the recipient surfaces. Accordingly, the final exposure pressure decreased compared to the final run of the previous day. However, the development of p_{fep} on the second day shows two interesting features: First, the p_{fep} reaches the level of the previous day within four runs. The observed rise during c4.2 is much faster and displays an exponential shape, compared to the linear rise during c4.1. Second, the p_{fep} reaches a stable level during c4.2, which lies below the expansion pressure. This indicates an equilibrium between adsorption and decontamination effects from the run procedure. Therefore, no saturation of adsorption is observed on the inner recipient surfaces of stainless steel and gold coated steel.

4.4.2 BIXS count rate development during the campaigns

The BIXS count rates measured during the five campaigns were presented in section 4.3.3. They were observed to rise in all cases, but no saturation level was distinctively observed.

In this section, a quantitative investigation of saturation effects will be performed. For this purpose, the model for the time dependence of hydrogen adsorption on thin gold films from section 1.3.2 is used. The model is described in section 4.4.2.1. It is then compared to the measurements from campaigns c1 and c2 (section 4.4.2.2), as well as for c3 and c4.1 (section 4.4.2.3). Finally, campaigns c4.1 and c4.2 are considered together in section 4.4.2.4.

4.4.2.1 Fit model, method and statistics

Section 1.3.2 provides a model for hydrogen adsorption on thin gold films. It will be adopted in the following for tritium adsorption. Its appropriateness will have to be judged based on the fit results.

The model assumes an initially clean surface. This can safely be assumed for the five measurement campaigns due to the preparation of the sample (see section 4.1.2). Further, only adsorption effects are considered by the model. This limitation is acceptable, as the measurements showed no saturation level yet. Therefore, adsorption is assumed to dominate the change of the surface coverage.

The model is expressed in equation 1.9 for the surface coverage $\theta(t) = N(t)/N_{\max}$. It is related to the number $N(t)$ of adatoms by the maximum number $N_{\max}$ of adsorption sites on the sample. The model introduces the time constant τ of the adsorption process. $N(t)$ is related to the detector signal by a constant amplitude $A' = A/N_{\max}$. With a constant background y_{bg}, the detector signal $y(t)$ is expected to follow:

$$y(t) = y_{\mathrm{bg}} + A \cdot \left(1 - \mathrm{e}^{-t/\tau}\right) \tag{4.7}$$

The fits are applied in Origin[5] using the Levenberg-Marquardt algorithm (see appendix C.3). The reduced chi squared $\bar{\chi}^2$ is calculated as a measure of the goodness-of-fit. It is based on the final χ^2 minimised during the fit and normed with the degrees of freedom $\mathrm{dof} = n - p$. n is the number of measurements and p the number of the fit parameters. The $\bar{\chi}^2$ then turns out as:

$$\bar{\chi}^2 = \frac{\chi^2}{\mathrm{dof}} = \frac{\chi^2}{n-p}. \tag{4.8}$$

[5] OriginLab Corporation: *OriginPro*, Version 9.1 Sr3, 1991-2014

4.4.2.2 Exponential fit of campaigns c1 and c2

The BIXS count rates measured at $5 \cdot 10^{-5}$ mbar during campaigns c1 and c2 in figure 4.6 show linear increase. The model from the previous section predicts an exponential increase, in contrast. Therefore, a fit of the model to the measurement results from c1 and c2 allows no meaningful statements. Tritium adsorption on gold coated beryllium at $5 \cdot 10^{-5}$ mbar is too slow too allow for an investigation of saturation effects.

4.4.2.3 Exponential fit of campaigns c3 and c4.1

The BIXS count rates of campaigns c3 and c4.1 in figure 4.6 increase strongly during the campaigns. The rise slows down at the end of campaigns, but no distinct saturation level can be observed. To extrapolate the saturation count rate, the model from section 4.4.2.1 is fitted to the measurement data. Figure 4.11 shows a good visual agreement between model and data for nominal exposure pressures of $1 \cdot 10^{-3}$ mbar.

The results of the fit parameters can be found in table 4.3. The measurements show a comparable develpoment of the count rates. However, the fitted saturation amplitudes A deviate enough to not coincide within their mutual 1 σ uncertainties: for c3 is $A = 4.6 \pm 0.3$, while for c4.1 it is $A = 5.8 \pm 0.5$. However, the uncertainties of the fitted parameters are based alone on the statistical uncertainties of the count rates. Additional systematic uncertainties as discussed in section 4.2 are not considered. The lower saturation count rate may be due to the smaller tritium concentration in the tritiated gas of c3 (see section 4.2.2). However, this and other systematic influences on both campaigns can not be quantified.

Table 4.3: Results of the exponential fits to the BIXS count rates of all campaigns. The fit model is given in equation 4.7. The offset y_{bg} corresponds to the background count rate at run 0. The amplitude A is the saturation level. Both parameters are discussed in sections 4.4.2.3 and 4.4.2.4. The time constant τ of the fit is treated in section 4.5 for all campaigns. The $\bar{\chi}^2$ is defined in equation 4.8 is an indicator of the goodness-of-fit. It depends on the measurement uncertainty, as described in appendix C.3. However, most of the measurement uncertainties can not be quantified. Therefore, no meaningful statement about the goodness-of-fit can be made from $\bar{\chi}^2$ for the adsorption fits.

campaign	y_{bg}	A	τ	$\bar{\chi}^2$
c3	1.00 ± 0.03	4.6 ± 0.3	12.8 ± 1.3	1.90
c4.1	2.06 ± 0.04	5.8 ± 0.5	16.8 ± 2.2	2.08
c4.2	0.24 ± 1.20	8.2 ± 0.7	15.3 ± 3.8	0.56
c4 corr	2.10 ± 0.03	7.1 ± 0.3	22.7 ± 1.5	1.67

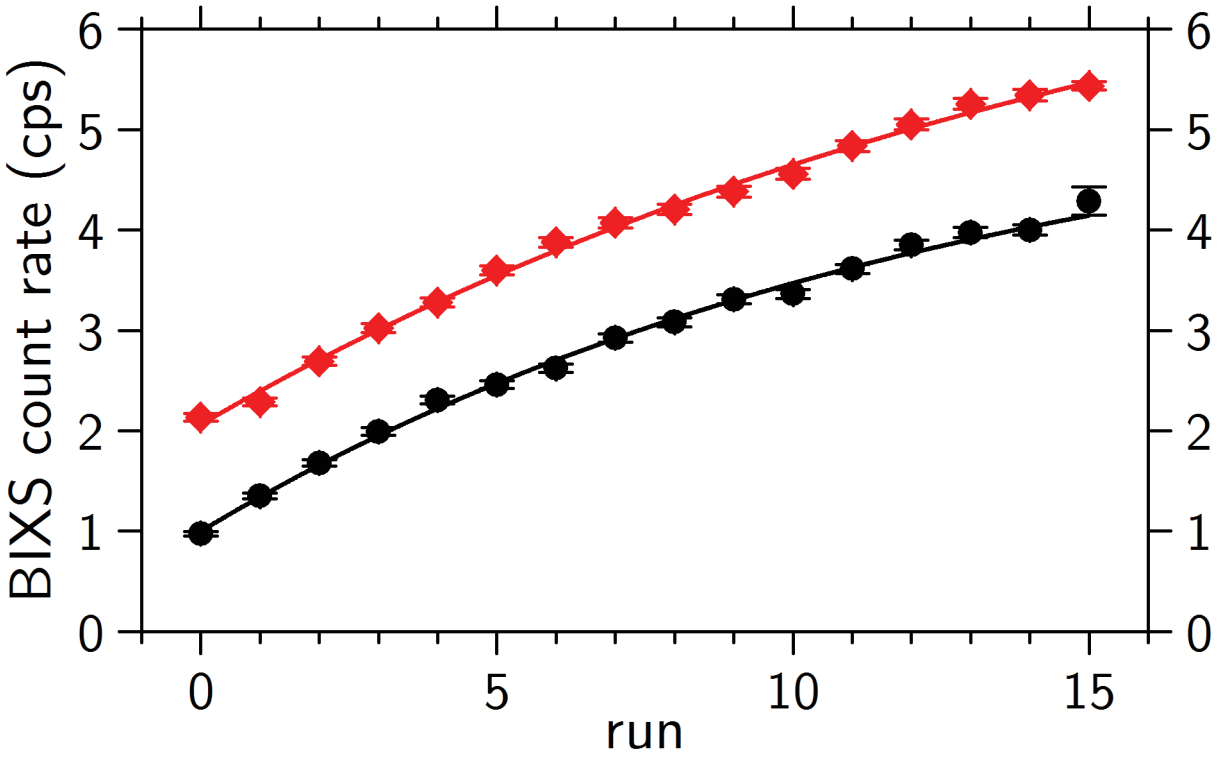

Figure 4.11: BIXS count rates of campaigns c3 and c4.1 fitted with exponential adsorption model. Black dots: c3 with fit (black line). Red diamonds: c4.1 with fit (red line). The error bars indicate only statistical uncertainties. Run 0 designates the background count rate measured before the first run. The measurements were performed at a nominal exposure pressure of $1 \cdot 10^{-3}$ mbar. As predicted by the fit model, the count rates show an exponential increase. But no distinct saturation level is reached.

The results of the saturation amplitude A from both campaigns can be combined by averaging with the arithmetic mean. It is described in appendix C.1 together with the calculation of the statistical uncertainty. The systematic uncertainty is calculated according to appendix C.2. The saturation level $A_{\mathrm{c3,c4.1}} \pm \Delta A_{\mathrm{c3,c4.1;sys}} \pm \Delta A_{\mathrm{c3,c4.1;stat}}$ is then:

$$A_{\mathrm{c3,c4.1}} = (5.2 \pm 0.4_{\,\mathrm{sys}} \pm 0.8_{\,\mathrm{stat}})\ \mathrm{cps}. \tag{4.9}$$

For these results, an influence of the dosage increase during the begin of the campaigns can not be excluded. However, this influence can not be quantified. Therefore, no criterion considering the exclusion of data points from the analysis can be derived. In any way, the influence can be estimated: smaller dosage at the begin of the campaigns could lead to smaller count rates at the begin, too. The exponential increase expected from the model would be dampened. Thus, the saturation amplitude and the time til the saturation is reached would be overestimated. Nevertheless, the fit results can be used to estimate the maximum saturation amplitude and maximum time til saturation.

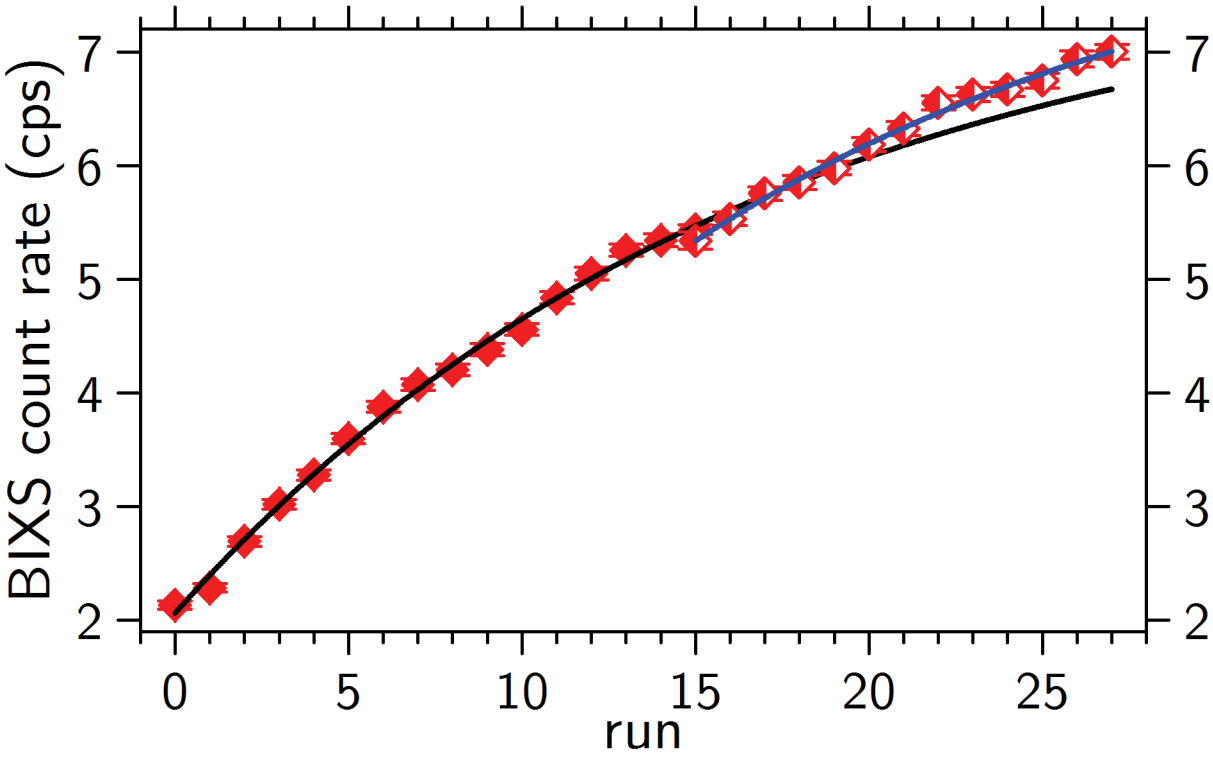

Figure 4.12: BIXS count rates of campaigns c4.1 and c4.2 fitted with exponential adsorption model. Full diamonds: c4.1 from run 0 to run 15. The fit of c4.1 (black line) is drawn extrapolated til the end of c4.2. Half filled diamonds: c4.2 from run 15 to run 27 with fit (blue line). The error bars indicate only statistical uncertainties. Run 0 is the background measured before run 1. The half filled diamond at run 15 indicates the background measurement before run 16. The measurements were performed at a nominal exposure pressure of $1 \cdot 10^{-3}$ mbar. Also on the second measurement day, no saturation level of the count rate is reached during c4.2. The fits show different slopes on both campaign days. This is attributed to diffusion of the adsorbed tritium into the sample bulk over night.

4.4.2.4 Exponential fit of campaigns c4.1 and c4 with corrected c4.2

The final exposure pressures were found to reach a saturation level during the second consecutive campaign day c4.2. This is based on adsorption on all inner recipient surfaces. For tritium adsorption on gold coated beryllium, figure 4.12 shows no saturation level on the second day.

The applied fit model relies on an initially clean sample and neglects desorption effects. The count rate continues to rise on the second day, however. The model is therefore found to be applicable even to two consecutive measurement days.

A BIXS background count rate was measured before c4.2. It had slightly decreased by about 0.1 cps compared to the final run of c4.1. This is attributed to desorption of adsorbed tritium from the sample surface during evacuation of the recipient

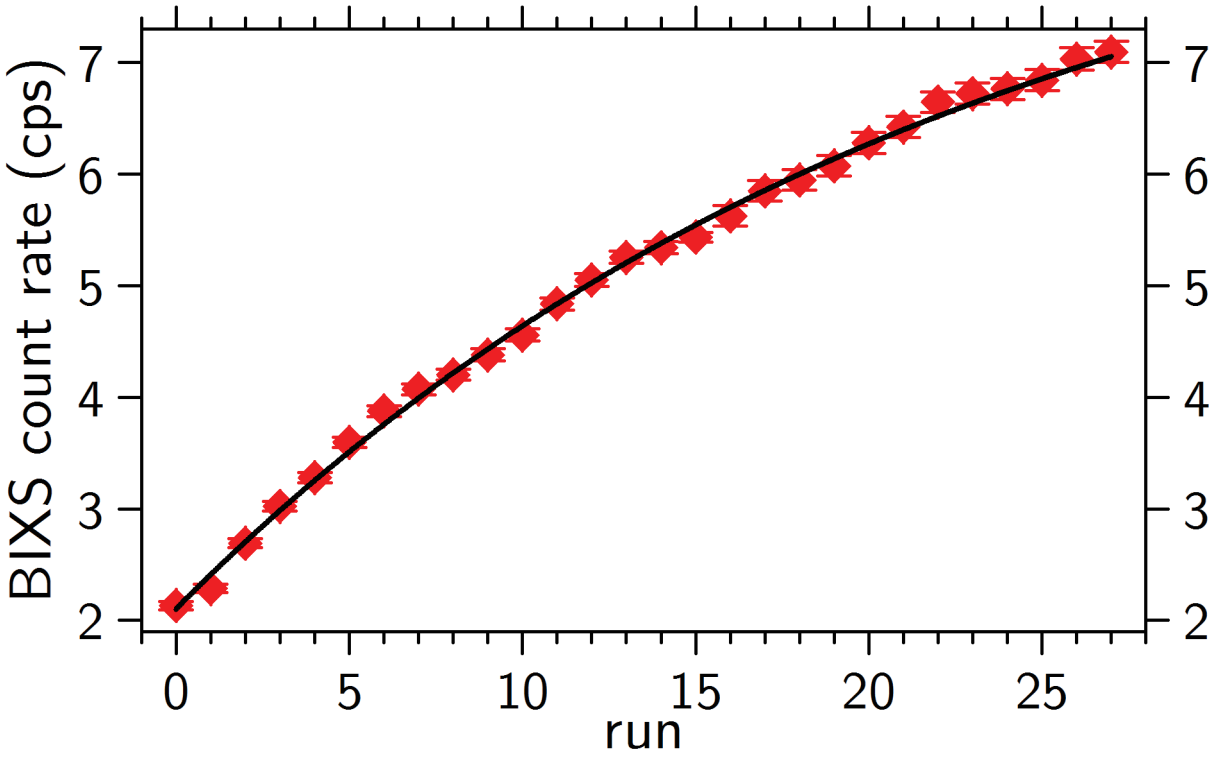

Figure 4.13: BIXS count rates of campaign c4 with corrected c4.2, fitted with exponential adsorption model. Dosage. Diamonds: c4.1 (runs 0 to 15) and c4.2 (runs 16 to 27) with fit (black line). c4.2 was corrected for the difference between c4.1 run 15 and the background measured before c4.2. The error bars indicate only statistical uncertainties. Run 0 is the background measured before run 1 of c4.1. The measurements were performed at a nominal exposure pressure of $1 \cdot 10^{-3}$ mbar. The fit predicts a saturation level that lies between that of the individual campaigns.

over night. The measurement stability over two days is impaired as discussed in section 4.6.2.1.

The fit model was applied to both campaigns individually as showed in figure 4.12. The initial count rate of c4.2 lies below the extrapolated fit from c4.1 but rises above it within three runs. The slope of the increase is steeper on the second day. Table 4.3 shows the fit results. The saturation amplitude is with $A = 8.2 \pm 0.7$ cps higher on the second day than during c4.1. In comparison, the saturation amplitude obtained from c4.1 lies closer to c3 than to c4.2. Also, $y_{\mathrm{bg}} = 0.24 \pm 1.20$ is close to zero and below the background contribution measured before the c4.1.

The small fitted y_{bg} can partially be attributed to a shift of the count rate during c4.2 from desorption over night. However, the measured shift is only about 0.1 cps. Also, the count rate should go to the same saturation amplitude as on the first measurement day. Another influence might be diffusion of tritium into the sample bulk as reported in section 4.6.6. This would decrease the surface coverage while tritium could still contribute

to the BIXS count rate. However, it is unknown if diffusion of the necessary extent can occur over night. A more thorough investigation is not possible as the start conditions of c4.2 are undefined: this is because the recipient was not decontaminated like before the other campaigns.

Nevertheless, the figure 4.12 shows a good visual agreement of the two campaign days. The small y_{bg} and the disagreement of the saturation level with former campaigns might be attributed to measurement fluctuations. In this case, saturation effect might be investigated by a fit of both campaigns over two days. The count rates cr of day c4.2 can be corrected for the shift of 0.1 cps due to tritium desorption over night. It is calculated from final run 15 of c4.1 and the background count rate of c4.2 designated as run 0:

$$\begin{aligned} \mathrm{cr}_{\mathrm{c4.2,corr}} &= \mathrm{cr}_{\mathrm{c4.2}} - \mathrm{cr}_{\mathrm{c4.2}}(\text{run } 0) + \mathrm{cr}_{\mathrm{c4.1}}(\text{run } 15) && (4.10)\\ &= \mathrm{cr}_{\mathrm{c4.2}} + 0.1 \text{ cps} && (4.11) \end{aligned}$$

The uncertainty of the corrected count rate $y_{\mathrm{c4.2,corr}}$ of the second measurement day is calculated according to appendix C.2. This increases the uncertainty of the count rates of c4.2 by about 0.09 cps.

The corrected count rate for c4 and its fit are displayed in figure 4.13. Table 4.3 lists a saturation amplitude $A_{\mathrm{c4,corr}} = 7.1 \pm 0.3$. As expected from a joint fit of c4.1 and c4.2, this lies between the saturation amplitude obtained from the individual fits.

4.5 Time dependence of the tritium surface contamination during the measurement campaigns

In the previous section, the model from section 4.4.2.1 was used to search for saturation effects in tritium adsorption measurements. The model applies to tritium adsorption on an initially clean gold sample and neglects desorption effects.

The model allows a statement about how fast adsorption proceeds: τ is the number of runs after which $1/e$ of the count rate of the saturation level is reached. This time constant is discussed based on the fit results listed in table 4.3.

The count rate during the campaigns c1 and c2 rises linearly. This corresponds to the series expansion of an exponential function to first order for small exponents n/τ. Tritium adsorption on gold coated beryllium is too slow to allow for a fit with the theoretical model. Therefore, no statement about the time til saturation coverage is reached can be made within one day at exposure pressures of $5 \cdot 10^{-5}$ mbar.

At a nominal exposure pressure of $1 \cdot 10^{-3}$ mbar, τ is comparable for c3, c4.1 and for c4.2. While $A_{\mathrm{c4.2}}$ rose above the values from c3 and c4.1, $\tau_{\mathrm{c4.2}}$ lies between the value of c3 and c4.1: $\tau_{\mathrm{c3}} = 12.8 \pm 1.3$ runs, $\tau_{\mathrm{c3}} = 16.8 \pm 2.2$ runs and $\tau_{\mathrm{c3}} = 15.3 \pm 3.8$ runs. This indicates that the same sorption process occurs during all three single day campaigns.

Diffusion of the adsorbed tritium into the sample leads to a shift in the background count rate over night, however. Therefore, $\tau_{\mathrm{c3}} = 22.7 \pm 1.5$ runs of the combined campaigns c4 lies considerably higher than for the single day campaigns. Combined campaign c4 can not be considered as a coherent physical process as are the single day campaigns. Therefore, its result is not considered in the following.

A result for τ can be calculated from all measurement campaigns at a nominal exposure pressure of $1 \cdot 10^{-3}$ mbar. The combined result is calculated by the arithmetic mean and derived with its statistical uncertainty as described by appendix C.1. The uncertainties of the fit parameters are propagated as systematic uncertainties as described in appendix C.2. The result of the time constant is then:

$$\tau_{\mathrm{c3,c4.1,c4.2}} = (15.0 \pm 2.7\,_{\mathrm{sys}} \pm 2.0\,_{\mathrm{stat}})\ \text{runs}. \tag{4.12}$$

This result shows large uncertainties without respecting even all systematic influences discussed in section 4.2. Especially, the pressure decreased during each exposure phase: from the nominal $1 \cdot 10^{-3}$ mbar to $(1 \ldots 60) \cdot 10^{-5}$ mbar, according to figure 4.9. Nevertheless, the result allows an estimation of the adsorption speed of tritium on gold coated beryllium. It indicates that during one standard campaign of 15 runs, the tritium coverage on gold coated beryllium rose to 1/e of its saturation level.

4.6 Comparison of decontamination methods

Subsequent to the previously discussed campaigns, the initial measurement conditions needed to be restored. This demands to decontaminate the surface of the sample and the X-ray transparent window of the BIXS setup. Three decontamination methods were applied: evacuation of the recipient (section 4.6.1), a bake-out of sample and recipient (section 4.6.3) and exposure to atmospheric air (section 4.6.4). The investigation of the decontamination methods allows also a statement about the stability and reproducibility of the measurements: The effect of evacuation on between and during measurement campaigns is investigated in section 4.6.2. Section 4.6.6) explains the memory effect observed in the BIXS background count rates.

4.6.1 Continuous evacuation of the recipient

After the first three campaigns c1, c2 and c3, the recipient was evacuated for at least four days below $8 \cdot 10^{-8}$ mbar. As the BIXs count rates in figure 4.14 show, tritium desorbed from the sample and X-ray transparent window during this time. After campaigns c1 and c2, the count rate dropped about 0.3 cps. After c3, it dropped about 0.5 cps corresponding to a higher initial surface activity. The shape of the decrease can be described with the model from section 1.3.3. It is used in the next section to quantify desorption under evacuation.

4.6.2 Effect of evacuation on the adsorption measurements

Evacuation phases are part of the standardised measurement procedure described in section 4.1. In this section, their influence on the surface coverage is investigated: for evacuation over night in section 4.6.2.1; and for evacuation between the exposure phases of a campaign in section 4.6.2.2.

4.6.2.1 Effect of evacuation over night

Between campaigns c4.1 and c4.2, the recipient was evacuated over night. This affects the measurement conditions in multiple ways. A mass spectrum was measured after the final pressure rise test of c4.1 and the initial test of c4.2: they who a decrease of about one magnitude of the relative intensities of all hydrogen species. The evacuation pressure before c4.2 run 1 is slightly lower than after the last run of c4.1, see figure 4.5. As figure 4.10 shows, the final pressure of the exposure phases on the second measurement day was initially decreased. All this is attributed to desorption from the inner surfaces of the recipient under evacuation over night.

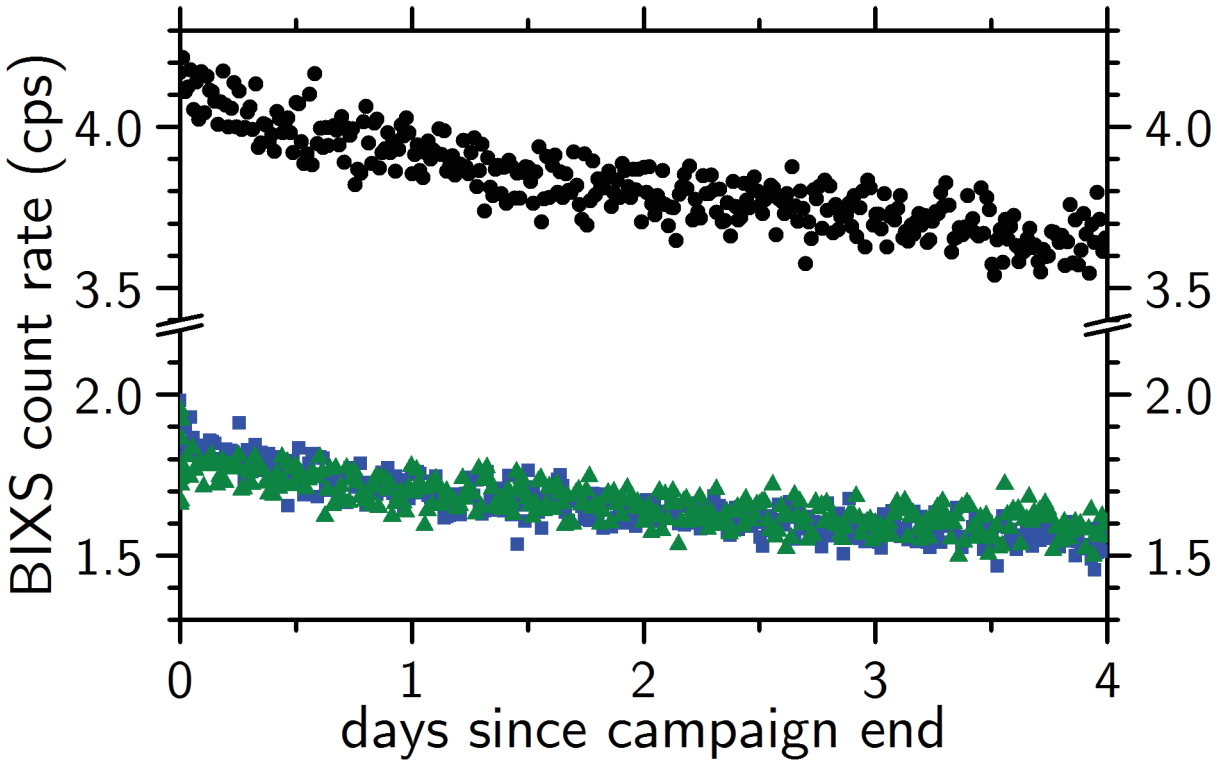

Figure 4.14: BIXS count rates decrease under evacuation of the recipient. The count rates were measured for four days after the final pressure rise test of campaigns c1 (blue squares), c2 (green triangles) and c3 (black dots). The pressure in the recipient was below 10^{-8} mbar during the whole time. From the decay, the effect of evacuation can be estimated with the model of Langmuir-Hinshelwood desorption.

Also due to evacuation over night, tritium desorbed from the surfaces of the sample and X-ray transparent window of the BIXS setup: the BIXS count rate after the last run of c4.1 was above the one measured after the pressure rise test before c4.2. The decrease of 0.10 ± 0.09 cps corresponds to roughly 3% of the surface activity after c4.1.

4.6.2.2 Effect of evacuation during the runs of a campaign

Between the exposure phases of a campaign, the recipient is evacuated to allow for unobstructed measurement of the BIXS count rates. the effect of this procedure can be estimated from the decrease of the count rates after c1, c2 and c3 under evacuation, see figure 4.14. Without impinging gas particles, desorption is only possible by the Langmuir-Hinshelwood mechanism: A model for the time dependence of the coverage under this condition was derived in section 1.3.3. It is based on the proportionality of the desorption rate to the square of the coverage $\theta(t)$. This implies no preconditions to the surface or the adspecies.

The BIXS count rate $y(t)$ is proportional to the $N(t) = \theta(t) \cdot N_{\max}$, where $N_{\max}$ is the maximum number of adsorption sites. This proportionality is accounted for by the amplitude $A = y(t)/N(t)$. A constant background is considered by adding N_{bg}. The start time of evacuation is chosen as t_0. With the constants α and β, the BIXS count rates are expected to follow:

$$y(t) = N_{\mathrm{bg}} + \frac{\alpha}{1 + \beta \cdot t}, \tag{4.13}$$

The fits are displayed in the appendix in figures D.4, D.5 and D.6. Table 4.4 shows the results. With them, the effect of 30 min of evacuation phase can be estimated:

$$\Delta y_{\mathrm{c1}}(30\ \mathrm{min}) = 0.004 \pm 0.028\ \mathrm{cps}, \tag{4.14}$$

$$\Delta y_{\mathrm{c3}}(30\ \mathrm{min}) = 0.005 \pm 0.126\ \mathrm{cps}. \tag{4.15}$$

The uncertainties of the results are derived from the uncertainties of the fit parameters with Gaussian error propagation (see appendix C.2). For the short interval of 30 min, they are considerably larger than the estimates by a factor of about 7 and 25, respectively. Nevertheless, the results will be used to estimate the effect of evacuation phases between exposures: the decrease corresponds to about 0.2% of the initial contamination after c1 and to about 0.1% in case of c3. The effect of evacuation during a 30 min evacuation phase is therefore deemed negligible. The evacuation phases do not affect the growth the surface coverage over the course of the campaigns.

After sufficient time $t \to \infty$, the count rates reach the limit N_{bg} given in table 4.4. They are roughly 50% larger than the background count rates of the subsequent runs given in table 4.2. This is due to the decontamination methods applied after evacuation of the recipient. These methods are described in the following.

Table 4.4: Fit results for the BIXS count rates under evacuation after campaigns c1, c2 and c3. The fit model is given in equation 4.13. N_{bg} is the residual background after long times t. α and β are fit constants. The $\bar{\chi}^2$ was calculated as described in appendix C.3. Due to the underestimation of the systematic unceertainties, it was found no good estimator for the goodness-of-fit (see section 4.4.2.2).

after	fitted days	N_{bg}	α	β	$\bar{\chi}^2$
c1	6,7	1,33 ± 0,02	0,51 ± 0,01	0,35 ± 0,03	0,90
c2	5,5	1,43 ± 0,03	0,36 ± 0,02	0,34 ± 0,07	1,25
c3	4,6	3,19 ± 0,07	0,91 ± 0,06	0,26 ± 0,04	0,96

4.6.3 Bake-out of the sample and the recipient

Before each campaign, the recipient was baked at 200°C for at least five days combined. The decontaminating effect of the bake-out can be compared to evacuation by one example case: during four days of evacuation, the BIXS count rate decreased for about 0.23 cps. The recipient was then baked at 200°C for four days and subsequently evacuated for another seven days. Evacuating the recipient during the whole 11 days, the count rate would have been expected to decrease less than 0.7 cps. This is even more so as the decrease is non-linear, as seen in section 4.6.1. However, the count rate measured after this procedure had decreased by about 1.8 cps. Baking is much more efficient than evacuation over the same period of time.

4.6.4 Exposure of the sample to atmospheric air

Isotope exchange reaction can occur between hydrogen isotopes and water in combination with adsorption [Nis92]. Using the isotope exchange effect for decontamination, the recipient and sample were exposed to atmospheric air. This was done after all campaigns for at least 30 min with at least 40 mbar. It was done systematically after the campaigns c4 for 0.5 h to 2 h at 40 mbar to 230 mbar. Table 4.5 lists all 27 runs.

The BIXS count rates shown in figure 4.15 were measured during 1,000 s to 2,000 s after the air exposure. They show a steep decrease during each measurement day, especially during the first one. A preferential influence of the measurement pressure, duration or

Table 4.5: Overview of the decontamination measurements by air exposure and bake-out. The runs are numbered chronologically. After exposure to atmospheric air at a certain time and pressure, the count rate is measured for 1,000 s to 2,000 s. The table also indicates if a bake-out was performed since the previous run.

run	date	duration	pressure	count rate	bake-out?
1...8	18.11.	30 min	42 mbar	7.2...6.3	no
9...13	19.11.	1 h	43 mbar	6.3...6.1	no
14...16	20.11.	2 h	43 mbar	6.0...5.8	no
17...24	26.11.	30 min	229 mbar	5.7...5.5	no
25...27	27.11.	2 h	228 mbar	5.3...5.3	no
28	1.12.	40 min	225 mbar	5.0	no
29	2.12.	40 min	233 mbar	4.3	yes
30	3.12.	40 min	755 mbar	3.7	yes
31...33	4., 5., 8.12.	40 min	1 bar	3.7...3.4	yes

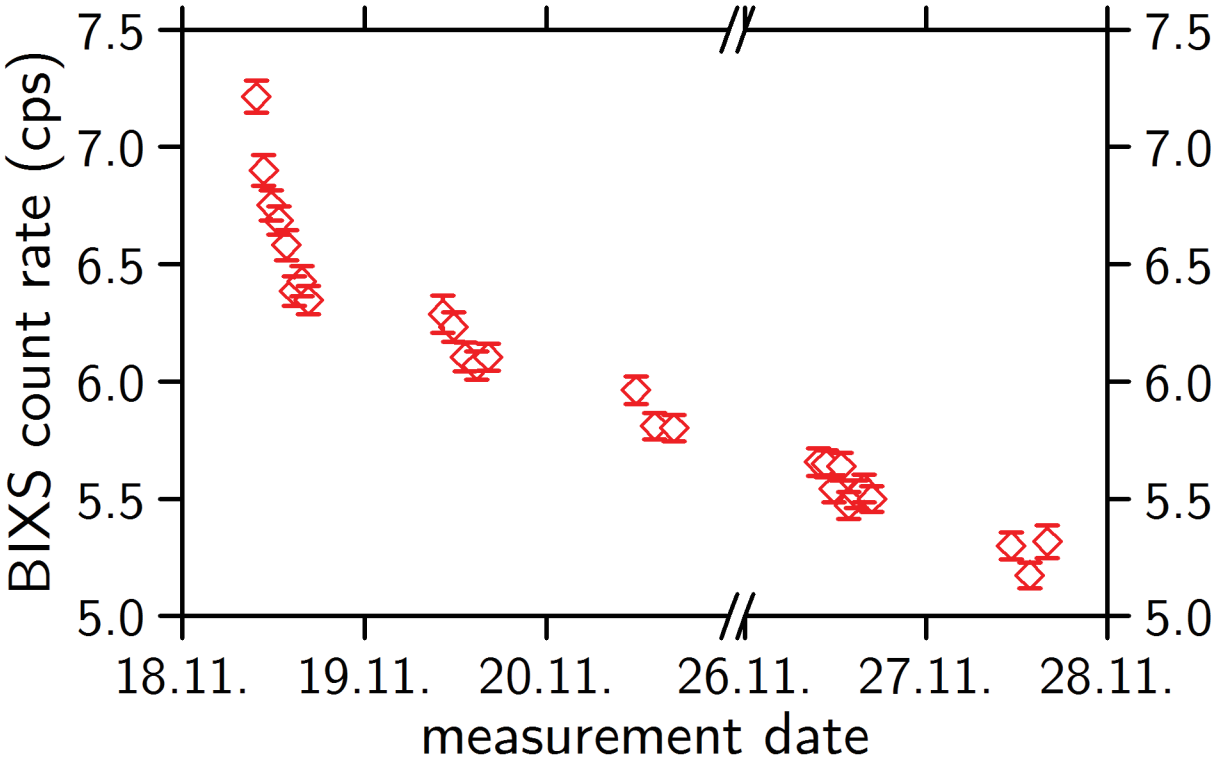

Figure 4.15: BIXS count rate decrease due to exposure of the sample to atmospheric air. The count rates were measured for 1,000 s to 2,000 s seconds. The error bars to the count rates (empty diamonds) indicate only the statistical uncertainties. Exposure of recipient and sample was performed in 27 runs after campaigns c4. The runs are numbered chronologically. The respective exposure times and pressures are listed in table 4.5. The count rates show a steep decrease on each measurement day. In comparison, the decrease from evacuation between the measurement days is negligible.

number of exposures on one day can not be found. The decrease from evacuation between the measurement days is considerably smaller. Quantifically, the count rate decreased for about 1.9 cps after five measurement days. The decrease from evacuation amounted only to 0.5 cps after 4 days after c3, though at smaller surface coverage.

4.6.5 Combination of bake-out and air exposure

A combination of the bake-out and air exposure, described in the two previous sections, was applied to the system. Five more runs were carried out with air exposure at 40 min and pressures of about 250 mbar, 750 mbar and 1,000 bar. Before the air exposure, the recipient was baked out for one day at about 200°C. Before the last run 33, it was even baked for three days. After bake-out and air exposure, the BIXs count rate was measured for 1,700 s to 2,000 s.

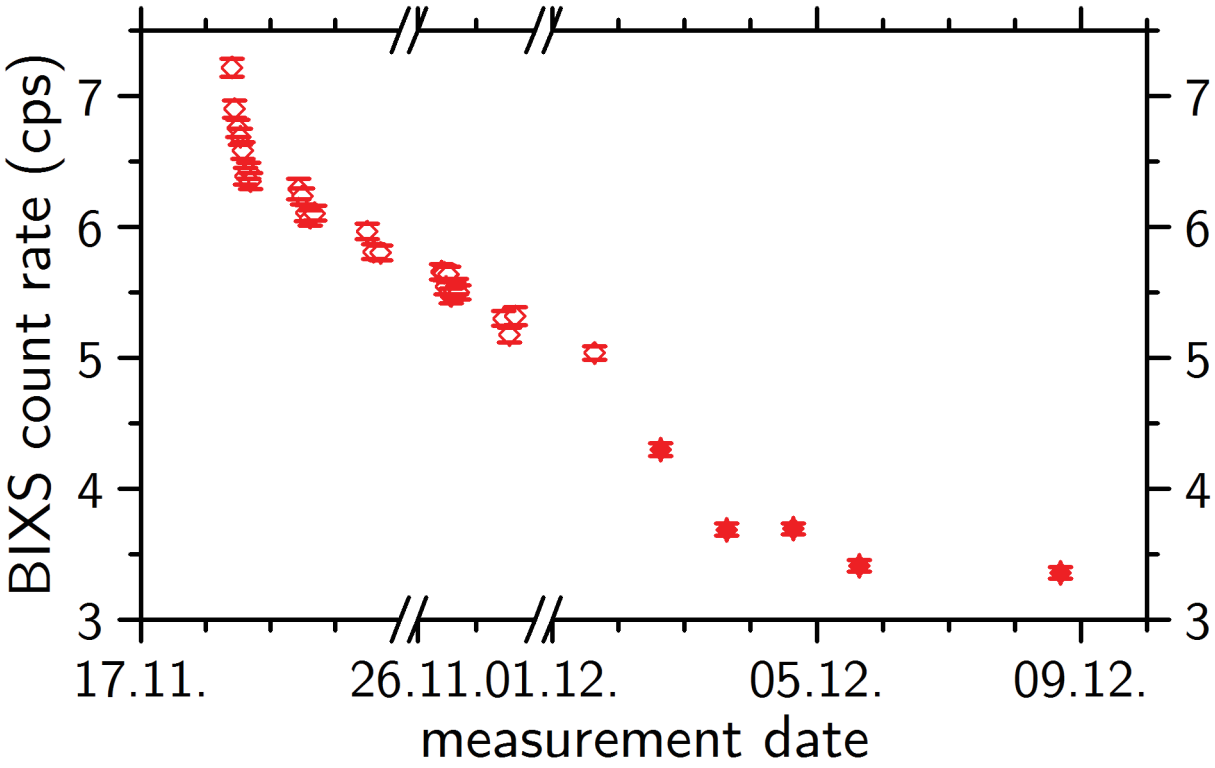

Figure 4.16: BIXS count rate decrease due to bake-out and subsequent exposure to atmospheric air. For the measurements without previous bake-out (empty diamonds) compare figure 4.15. Between the last five exposure runs (full diamonds), the recipient was baked at 200°. The respective exposure times and pressures are listed in table 4.5. The error bars indicate only statistical uncertainties of the BIXS count rates measured for 1,700 s to 2,000 s. The count rate decreases much faster during the first runs after bake-out than without bake-out. This is attributed to diffusion of absorbed tritium back to the bulk surface.

The development of the BIXS count rates are shown in figure 4.16. The effect from evacuation of the recipient between the runs of air exposure alone can be neglected. Then, the trend from air exposure alone is much slower compared to the decrease of the count rate after the first bake-outs. Thus, the decontamination by bake-out is more efficient than air exposure at comparable contamination conditions. The reason for this is discussed in the next section.

4.6.6 Memory effect due to tritium absorption

Bake-out and exposure to atmospheric air were compared to evacuation of the recipient alone: They were found to decrease the BIXS count rates more efficiently and over the extent reachable by evacuation (see sections 4.6.3 and 4.6.4).

Further, system bake-out showed to work more efficiently than air exposure in section 4.6.5. This can only be explained by tritium diffusion into the bulk material. There, the tritium

can not be removed by isotope exchange effect. When baking the recipient, the absorbed tritium receives kinetic energy. It can leave the bulk and fill empty adsorption sites on the surface decontaminated from the bake-out. Subsequent air exposure could then remove surface tritium by isotope exchange.

The observation proves the diffusion of tritium into the bulk of the sample and the X-ray transparent window of the BIXs setup. This explains the memory effect observed as the increase of the background count rate over the course of the campaigns. Before each run, the same decontamination methods were applied to a comparable extent. The background count rate especially rises from campaign c3 to c4.1. This is attributed to the higher surface coverage reached at higher exposure pressures of tritiated gas: the increased number of adatoms is likely to increase the probability for absorption of adatoms into the bulk.

4.7 Discussion of the results

The measurements for the investigation of tritium adsorption on gold coated beryllium were evaluated in the previous sections. This includes five measurement campaigns according to a standardised measurement procedure. Further, the decontamination performed between the campaigns yields valuable information.

As these were the first measurements with the TRIADE setup, its performance is rated based on the results in section 4.7.2. The results allow statements about tritium adsorption on gold coated beryllium in section 4.7.1. They have implications for the KATRIN experiment, as discussed in section 4.7.3.

4.7.1 Performance of the TRIADE setup

Investigation of tritium adsorption on gold coated beryllium is possible with the TRIADE setup. The achieved minimum detection limit of about 10% was shown to be reached for the applied measurement procedure (see section 4.2.6). For tritium adsorption on gold coated beryllium, it was at the most 3.5% of one monolayer. For tritium adsorption on the sample alone, the limit was still less than 8% of one monolayer. These statements are with respect to the expected count rate from simulations (section 3.1.4).

The reproducibility of the measurement conditions can be assured by decontamination of sample and recipient (see section 4.1.2). A bake-out of the recipient is found to be more efficient than exposure to moist atmospheric air (section 4.6.5). The air exposure in turn decontaminates more efficient and to a greater extent than evacuation of the recipient (section 4.6.1). A memory effect of the BIXS count rate is observed by tritium absorption in the sample (section 4.6.6). However, this does not affect the adsorption process, as the good agreement between the campaign results at same pressures shows. The results for the saturation amplitude A and the time constant of adsorption τ still deviate considerably (sections 4.4.2 and 4.5): they show statistical uncertainties of about 15%. This lack in reproducibility is attributed to two reasons: different tritium concentrations of the tritiated gas (section 4.2.2) and the decreasing recipient pressure during exposure phase (section 4.2.5).

The measurement results develop visually stable along the theoretical prediction (section 4.4.2). The stability of the measurement conditions is partially achieved by the standardised procedure of single day measurement campaigns: evacuation of the recipient for BIXS measurements has a negligible effect on the surface coverage (section 4.6.2). However, the recipient pressure decreases during the exposure phase by up to two magnitudes (section 4.2.5). The pressure at the end of exposure phases increases during those campaigns with a nominal exposure pressure of $1 \cdot 10^{-3}$ mbar (section 4.4.1). Due to the pressure decrease, leaked air contributes at least 25% at the end of campaigns at a nominal exposure pressure of $5 \cdot 10^{-5}$ mbar (section 4.2.3). This impairs the stability of the tritium

exposure conditions inside the recipient. Due to the pressure dependence of adsorption, the results can not be attributed to a distinct exposure pressure.

With the measurement results, the tritium coverage on gold coated beryllium can be estimated at any time. This would allow to calculate the background signal from tritium adsorbed on the X-ray transparent window of a BIXS system (see section 1.4.1). Inside TRIADE, this is possible for comparable measurement conditions at the same nominal exposure pressure of $1 \cdot 10^{-3}$ mbar. Especially, measurements with other sample materials could lead to a higher signal contribution from the sample. This reduces the effect of the uncertainties to the measurement interpretation.

4.7.2 Results of tritium adsorption measurements with gold coated beryllium

At a nominal exposure pressure of $5 \cdot 10^{-5}$ mbar, two measurement campaigns have been performed. Tritium adsorption was observed with more than 95% probability. However, no saturation effects were observed. Also, the linear rise of the count rate allowed no comparison to the theoretical expectation for the time dependence of tritium adsorption.

Three more campaigns were performed at a nominal exposure pressure of $1 \cdot 10^{-3}$ mbar. Again, tritium adsorption could be confirmed with more than 95% probability. The development of the count rates showed an exponential increase towards a saturation limit that could not be observed distinctively.

The model from section 1.3.2 was found to apply well to the development of the count rate at $1 \cdot 10^{-3}$ mbar. The model is based on a general expectation for the time dependence of adsorption [Lüt97]. Especially, hydrogen adsorbing on thin gold films was found to apply to it at 78 K, too [Sto92]. Thus, time dependence of tritium adsorption is found in accord with that of hydrogen.

The saturation limit of tritium adsorption was extrapolated by a fit with the model from section 1.3.2:

$$A = (5.2 \pm 0.4_{\,\mathrm{sys}} \pm 0.8_{\,\mathrm{stat}})\ \mathrm{cps}. \tag{4.16}$$

This count rate can be compared to the expectation for one monolayer of adsorbed tritium from simulations, see section 3.1.4. Adding the contributions from the sample and the X-ray transparent window leads to 7.6 ± 0.2 cps[6]. Consequently, the measurement result corresponds to a tritium coverage of about 0.68. This is in accord with the expectation from hydrogen to only chemisorb, thus not reaching more than one monolayer. However, this extrapolation can not exclude formation of multilayers at higher coverages.

[6] the uncertainties were propagated according to appendix C.2

The time after which $1/e$ of the adsorption limit is reached is also obtained by the fit:

$$\tau = (15.0 \pm 2.7_{\text{sys}} \pm 2.0_{\text{stat}}) \text{ runs.} \tag{4.17}$$

The result allows to estimate the tritium coverage on the sample at a given time. As discussed in the previous section, the result can be used to estimate the background on gold coated beryllium windows in other BIXS systems, too. However, different samples exhibit different surface structures, which have an influence on sorption processes [Atk06].

The interpretation of the measurement results is restricted due to the pressure decrease during exposure of the sample to tritiated gas (see section 4.1.5). The pressure dropped by up to two magnitudes during individual exposure phases. Pressure decrease reduced over the course of the campaigns at a nominal exposure pressure of $1 \cdot 10^{-3}$ mbar. However, adsorption is a pressure dependent process [Lüt97]. The changing pressure conditions are sure to have influenced both the obtained results for A and τ.

As a measure of the actual pressure conditions during these three runs, the average dosage [Lüt97] was calculated in section 4.2.5. Taking into account the gas correction factor for the main pressure sensor, it is $(5.1 \pm 3.0) \cdot 10^{-4}$ mbar $\cdot$ h. At 15 min exposure phase, this corresponds to an average pressure of $(2.1 \pm 1.0) \cdot 10^{-3}$ mbar.

4.7.3 Implication of the results for the KATRIN experiment

Two BIXS systems will be installed at the rear wall of the KATRIN tritium source [Bab12] (see section 1.4.3). They will be separated from the tritium plasma by X-ray transparent windows of gold coated beryllium [Bab14]. The detectors are designated to measure the source activity at an expected count rate of 6.6 kcps [Bab12]. Tritium from the source plasma will adsorb on the X-ray transparent window of the BIXS system. This causes an uncertainty that needs to be considered with respect to the 0.1% target presicion of the measurements.

The systematic shift of the BIXS count rate can be estimated with the saturation coverage from equation 4.16 and the simulations in section 3.1.4: the tritium adsorbed on the gold coated beryllium window contributes about 2.9 cps to the measured count rate. This is about half of the allowed total uncertainty. However, this consideration does not take into account a difference in the detection efficiency compared to TRIADE. Such differences, e.g. from differences in the geometry of the BIXS setups, need to be considered by appropriate simulations. Also, the pressure at the rear wall is only $5 \cdot 10^{-5}$ mbar. In contrast, the result in equation 4.16 was measured at an average pressure of about $2 \cdot 10^{-3}$ mbar. As the adsorption rate is proportional to the gas pressure (see section 1.2.4), the actual background activity is estimated to be smaller by an unknown amount. At $5 \cdot 10^{-5}$ mbar, the coverage was observed to rise only linearly. This would cause for the BIXS monitors at the KATRIN rear wall a linear drift.

Especially designed to define the potential of the tritium source, the rear wall consists of a gold coated material, too [Bab12]. This allows to estimate very roughly the time after which stable measurement conditions are reached. For 99% of the saturation coverage, the time constant from equation 4.17 predicts about 69 runs. With the average run dosage and pressure from the previous section, the stability requirement returns (17.3 ± 13.0) h. This uncertainty of 75% does not yet consider the different surface materials. Also, the time constant was measured at tritium pressures more than a magnitude above the rear wall conditions of $5 \cdot 10^{-5}$ mbar. In this pressure range, the tritium coverage was observed to grow much slower. Thus, reaching stable measurement conditions in the KATRIN tritium source is estimated to take at least one day at tritium exposure.

Most of the inner surfaces of the tritium source consist of stainless steel. They are also assumed to have an influence on the source potential[7]. Steel was observed to reach a saturation state faster than the gold coated beryllium sample (see section 4.4). Also, the pressure at the center of the tritium source lies at $1 \cdot 10^{-3}$ mbar. The time estimate for stable measurement conditions deduced above can thus be applied to these surfaces more appropriately. For these surfaces follows a coverage of 0.99 in less than a day.

[7] Nico Werling: *Einflsse von Variationen der Austrittsarbeit innerhalb des WGTS Strahlrohres auf die Neutrinomassen-Sensitivitt des KATRIN-Experiments*, Bachelor's thesis at the KIT, 2015

5 Summary and outlook

First tritium adsorption measurements have been performed with TRIADE on gold coated beryllium surfaces. The sample was repeatedly exposed to a measurement gas with a tritium concentration of at least 80% at room temperature. The surface activity was measured afterwards with a BIXS system under evacuation of the recipient. The development of the count rates was stable and reproducible between the five measurement campaigns.

Tritium adsorption on gold coated beryllium was observed with at least 95% probability during all measurement campaigns. The initial pressure of $5 \cdot 10^{-5}$ mbar and $1 \cdot 10^{-3}$ mbar was observed to decrease during exposure pressure.

Two measurement campaigns were performed with an initial exposure pressure of about $5 \cdot 10^{-5}$ mbar. The surface activity rose linearly during the campaigns. No saturation effect could be observed.

The sample was exposed in three measurement campaigns to an initial pressure of about $1{\cdot}10^{-3}$ mbar. The average dosage of each 15 min exposure phase was $(5.1{\pm}3.0){\cdot}10^{-4}$ mbar·h. The BIXS count rates increased exponentially towards a saturation level that can not be observed distinctively, however. The surface activity development is found to fit a general adsorption model for the surface coverage. From literature, the model is known to apply to the hydrogen coverage on thin gold films at 78 K, too.

The saturation effect of tritium adsorption can be quantified for these three campaigns with the theoretical model. The saturation limit is extrapolated to:

$$A = (5.2 \pm 0.4_{\text{sys}} \pm 0.8_{\text{stat}}) \text{ cps.} \tag{5.1}$$

The saturation limit corresponds to a coverage of $\theta = 0.68$ compared to the simulated activity from one monolayer of adsorbed tritium. This matches the expectation that tritium does not adsorb in multilayers.

The time constant of adsorption, after which $1/e$ of the saturation limit is reached, is estimated with:

$$\tau = (15.0 \pm 2.7_{\text{sys}} \pm 2.0_{\text{stat}}) \text{ runs.} \tag{5.2}$$

At continuous tritium exposure, 99% of the saturation coverage of gold coated beryllium are reached after roughly 17 h. Therefore, the measurement conditions inside the KATRIN

tritium source are expected to stabilise during the first couple of days under tritium conditions.

Future investigation of tritium adsorption with TRIADE requires enhanced reproducibility of the measurement conditions. To expose the sample to tritiated gas at a constant pressure, the measurement procedure needs to be improved. For example, a constant stream of tritiated gas could be established inside the recipient. The signal contribution from gaseous tritium in the recipient can be neglected according to simulations. For a reliable pressure monitoring, the main pressure sensor of TRIADE should be calibrated with a gas species independent pressure sensor.

With stable pressure conditions, the pressure dependence of tritium adsorption can be investigated. The saturation coverage with tritium can be measured as a function of pressure at a given temperature in so called isotherms. Interpolation of the measurement results would allow to calculate the background of BIXS monitoring systems at arbitrary pressures.

A background signal for BIXS systems arises from tritium adsorbed on the X-ray transparent window in front of the detector. The window inside the TRIADE setup is made of gold coated beryllium, as is the sample that was investigated in this work. This allows to determine the background from the sample under the same measurement conditions: from the saturation coverage and the time constant, the activity of tritium adsorbed on the window can be calculated at any time.

With the background from the BIXS window known, the measurement of tritium adsorption on other materials becomes possible, too. For the KATRIN experiment, tritium adsorption on gold coated steel and stainless steel is of interest. As the tritium source of KATRIN is cooled to about 30 K, the temperature dependence of tritium is of specific interest, too. The temperature of the sample inside TRIADE can be regulated between ~ 120 K and ~ 470 K. Therefore, TRIADE also provides the possibility of temperature dependent adsorption measurements in the future.

Appendix A

Solutions of differential equations from adsorption and desorption rates

A simplified model of the surface coverage θ in thermal equilibrium of gas and solid includes adsorption and two desorption effects: Due to Langmuir-Hinshelwood and Eley-Rideal mechanism. All three effects can be descried by differential equations in θ.

The adsorption rate is a differential equation of the surface coverage θ [Sto92]:

$$\left(\frac{\mathrm{d}\theta}{\mathrm{d}t}\right)_{\mathrm{ads}} = a\ (1-\theta)\,. \tag{A.1}$$

Desorption due to Langmuir-Hinshelwood mechanism (LH) fulfills the differential equation [Mil06]:

$$\left(\frac{\mathrm{d}\theta}{\mathrm{d}t}\right)_{\mathrm{LH}} = -b\ \theta^2. \tag{A.2}$$

As LH includes two surface atoms, θ enters the equation in second order.

Desorption due to Eley-Rideal mechanism (ER) was found for hydrogen at $\approx 2.6{\cdot}10^{-3}$ mbar and 78 K to fulfill [Sto92]:

$$\left(\frac{\mathrm{d}\theta}{\mathrm{d}t}\right)_{\mathrm{ER}} = -c\ \theta. \tag{A.3}$$

A.1 Adsorption

Equation A.1 may be solved with an integration ansatz:

$$\int_{\theta_0}^{\theta} \frac{\mathrm{d}\theta'}{1-\theta'} = a \cdot \int_{t_0}^{t} \mathrm{d}t'. \tag{A.4}$$

Integration gives:

$$[-\ln(1-\theta')]_{\theta_0}^{\theta} = [a \cdot t']_{t_0}^{t}\,. \tag{A.5}$$

This yields:

$$\theta(t) = 1 - (1-\theta_0)\ \mathrm{e}^{-a\cdot(t-t_0)}. \tag{A.6}$$

A.2 Langmuir-Hinshelwood desorption

Equation A.2 is a special case of the Bernoulli equation [Bro08]:

$$\dot{y} + P(x)\ y = Q(x)\ y^n, \tag{A.7}$$

with $P(x) = 0$, $Q(x) = -b$ and $n = 2$.

A Bernoulli equation can be reduced to a differential equation of first order: First, the equation is divided by y^n. Then, the substitution $z = y^{-n+1}$ is performed. The result can be solved with an integration ansatz:

$$\int_{z_0}^{z} \mathrm{d}z' = -b \cdot \int_{t_0}^{t} \mathrm{d}t'. \tag{A.8}$$

Integration and resubstitution yields:

$$\theta(t) = \left(\theta_0^{-1} - b\ (t-t_0)\right)^{-1}. \tag{A.9}$$

A.3 Adsorption and desorption

The total change of the coverage is described by the superposition of the individual rates:

$$\left(\frac{\mathrm{d}\theta}{\mathrm{d}t}\right)_{\mathrm{tot}} = \left(\frac{\mathrm{d}\theta}{\mathrm{d}t}\right)_{\mathrm{ads}} + \left(\frac{\mathrm{d}\theta}{\mathrm{d}t}\right)_{\mathrm{LH}} + \left(\frac{\mathrm{d}\theta}{\mathrm{d}t}\right)_{\mathrm{ER}} \tag{A.10}$$

Inserting equations A.1, A.2 and A.3 returns:

$$\left(\frac{\mathrm{d}\theta}{\mathrm{d}t}\right)_{\mathrm{tot}} = a\ (1-\theta) - b\ \theta^2 - c\ \theta. \tag{A.11}$$

This is a non-linear first-order ordinary differential equation or Riccati equation [Bro08] in θ:

$$\dot{\theta} = P(t)\ \theta^2 + Q(t)\ \theta + R(t), \tag{A.12}$$

with the terms:

$$P(t) = -b, \tag{A.13}$$
$$Q(t) = -(a + c), \tag{A.14}$$
$$R(t) = a. \tag{A.15}$$

A Riccati equation may be solved by a substitution of type:

$$\theta = \frac{z}{P(t)} + \beta(t) = -\frac{z}{b} + \beta(t). \tag{A.16}$$

Demanding the coefficient of first order in z to vanish yields:

$$\beta(t) = -\frac{a + c}{2b}, \tag{A.17}$$

and:

$$\dot{z} + \gamma = z^2, \tag{A.18}$$

where:

$$\gamma = \frac{1}{4}(a + c)^2 + ab > 0. \tag{A.19}$$

$\gamma > 0$ is due to physical reasons: a and c consist of the sticking probability and a particle stream, which is positive due to the definition of rates' sign. c consists of an exponential factor and a preexponential factor > 0.

As $\gamma \neq \gamma(t)$, one particular solution to the differential equation in z A.18 is:

$$z_{1/2} = \pm\sqrt{\gamma}. \tag{A.20}$$

Equation A.18 is a Bernoulli equation [Bro08] which may be solved using a second substitution:

$$z = \frac{1}{u} + z_1 = \frac{1}{u} + \sqrt{\gamma}. \tag{A.21}$$

This leads to:

$$\dot{u} + 2\sqrt{\gamma}\, u = -1. \tag{A.22}$$

This is a linear first-order ordinary differential equation [Bro08]. A solution to the homogenous problem is given by:

$$u_{\text{hom}} = u_0\, \mathrm{e}^{-\int P\, \mathrm{d}t} = u_0\, \mathrm{e}^{-2\sqrt{\gamma}\, (t - t_0)}. \tag{A.23}$$

A solution to the inhomogeneous problem can be found by:

$$u_{\text{inh}} = \frac{1}{z_2 - z_1} = -\frac{1}{2\sqrt{\gamma}}. \tag{A.24}$$

The general solution is then given by:

$$u_{\mathrm{tot}} = -\frac{1}{2\sqrt{\gamma}} + u_0 \ \mathrm{e}^{-2\sqrt{\gamma}\ (t-t_0)}. \tag{A.25}$$

With the definitions:

$$A = b^{-1}, \tag{A.26}$$

$$B = \sqrt{\gamma} + \frac{a+c}{2}, \tag{A.27}$$

$$D = 2\sqrt{\gamma}, \tag{A.28}$$

$$C_0 = (b \cdot y_0 + B)^{-1}, \tag{A.29}$$

resubstitution yields the time dependent surface coverage:

$$\theta(t) = -AB - \frac{AD}{u_0 D \ \mathrm{e}^{-D\ (t-t_0)} - 1}. \tag{A.30}$$

The integration constant u_0 can be determined by the requirement:

$$\theta(t = t_0) \stackrel{!}{=} \theta_0. \tag{A.31}$$

This returns:

$$u_0 \ D = 1 - \frac{D}{\theta_0/A + B}. \tag{A.32}$$

The integration constant changes its sign at $\theta_0 = \theta_{\mathrm{eq}}$:

$$\theta_{\mathrm{eq}} = A \ (D - B). \tag{A.33}$$

The equilibrium coverage θ_{eq} is reached for large times t. For $\theta_0 > \theta_{\mathrm{eq}}$, the integration constant has a positive sign and the coverage decreases. For $\theta_0 < \theta_{\mathrm{eq}}$, the integration constant has a negative sign and the coverage increases.

Appendix B

Details of the TRIADE setup

This appendix details several aspects of the TRIADE setup. First, the parameter settings of the Amptek X-123 are detailed. Also, the pumps in the main setup are displayed. Then, a listing of all pressure and temperature sensors of the TRIADE setup is given. All data in this appendix is taken from the diploma thesis of Fabian Schneck[1].

B.1 Pumps in the TRIADE vacuum setup

Table B.1: Overview of pumps in the TRIADE main setup.

Pump	Siemens Interatom	Normetex	Pfeiffer TMU200	Leybold SL80
Designation	VA055	VA054	VA053	VA052
Max. fore vacuum (mbar)	1000	100	$\leq 10^{-1}$	12
Ultimate pressure (mbar)	100	10^{-2}	10^{-8}	$< 2 \cdot 10^{-10}$
Pumping speed	$3\,\mathrm{m}^3/\mathrm{h}$	$12\,\mathrm{m}^3/\mathrm{h}$	180 l/s	65 l/s
Leak rate (mbar l/s)	$\leq 10^{-9}$	$\leq 10^{-9}$		

[1] Fabian Schneck: *Design and setup of the Tritium Adsorption Desorption Experiment (TRIADE)*, Diploma thesis, 2013

B.2 Sensor system of the TRIADE vacuum setup

The quadrupole mass spectrometer used in the TRIADE setup is a MKS Microvision Plus (MKS Instruments, 2 Tech Drive, Suite 201, Andover, MA 01810, USA). The pressure and temperature sensors used are detailed in the following tables:

Table B.2: Overview of TRIADE pressure sensors.

Designation	Measurement range in mbar	Location/description	Type
RP001	10^{-1} ... 10^{3}	detector electronics volume	MKS 902
RP002	10^{-1} ... 666	sampling port	MKS 722B
RP003	10^{-2} ... 20	BV061	Baratron 626B
RP004	$1.3 \cdot 10^{-1}$ ... $1.3 \cdot 10^{3}$	BV061	MKS 902
RP005	10^{-5} ... 10^{-1}	BV061	Baratron 627D
RP006	10^{-10} ... 10^{-3}	BV061	MKS 903
RP007	10^{-1} ... 10^{3}	IF-volume	MKS 902
RP008	10^{-1} ... 10^{3}	BV062	MKS 902
RP009	10^{-1} ... 10^{3}	ZTS connection	MKS 902

Table B.3: Overview of TRIADE temperature sensors.

Designation	Measurement range (°C)	Description	Type
RT011	-30 ... $+70$	heat sink detector electronics	Pt1000
RT012	0 ... $+200$	heating cable BV061	Pt100
RT013	0 ... $+200$	flange heater BV061	Pt100
RT014	0 ... $+200$	high vacuum connection VA052	Pt100
RT015	-200 ... $+200$	heating cable BV062	Pt100
RT016	-200 ... $+200$	heat exchanger BV061	Pt100
RT017	0 ... $+200$	cooling gas flow	Pt100

B.3 Parameter settings of the Amptek X-123

This is a complete listing of the settings for the calibration measurements performed with the Amptek X123. The same settings have been used for the measurements described in this work. The listing is an excerpt from a spectrum file.

RESC=?; Reset Configuration
CLCK=80; 20MHz/80MHz
TPEA=11.200; Peaking Time
GAIF=1.0447;
GAIN=69.115; Total Gain (Analog * Fine)
RESL=204; Detector Reset Lockout
TFLA=0.200; Flat Top
TPFA=100; Fast Channel Peaking Time
PURE=ON; PUR Interval On/Off
RTDE=OFF; RTD On/Off
MCAS=NORM; MCA Source
MCAC=8192; MCA/MCS Channels
SOFF=OFF; Set Spectrum Offset
AINP=POS; Analog Input Pos/Neg
INOF=DEF; Input Offset
GAIA=15;
CUSP=0; Non-Trapezoidal Shaping
PDMD=NORM; Peak Detect Mode
THSL=0.976; Slow Threshold
TLLD=OFF; LLD Threshold
THFA=56.25; Fast Threshold
DACO=SHAPED; DAC Output
DACF=0; DAC Offset
RTDS=0; RTD Sensitivity
RTDT=0.00; RTD Threshold
BLRM=1; BLR Mode
BLRD=3; BLR Down Correction
BLRU=0; BLR Up Correction
GATE=OFF; Gate Control
AUO1=ICR; AUXOUT Selection
PRET=OFF; Preset Time
PRER=OFF; Preset Real Time
PREC=OFF; Preset Counts
PRCL=1; Preset Counts Low Threshold
PRCH=8191; Preset Counts High Threshold
HVSE=-110; HV Set
TECS=220; TEC Set
PAPS=ON; Preamp 8.5/5 (N/A)
SCOE=RI; Scope Trigger Edge
SCOT=12; Scope Trigger Position
SCOG=16; Digital Scope Gain
MCSL=1; MCS Low Threshold
MCSH=8191; MCS High Threshold
MCST=0.00; MCS Timebase
AUO2=ICR; AUXOUT2 Selection
TPMO=OFF; Test Pulser On/Off
GPED=RI; G.P. Counter Edge
GPIN=AUX1; G.P. Counter Input
GPME=ON; G.P. Counter Uses MCAEN?
GPGA=ON; G.P. Counter Uses GATE?
GPMC=ON; G.P. Counter Cleared With MCA Counters?
MCAE=ON; MCA/MCS Enable
BOOT=ON; Turn Supplies On/Off At Power Up
¡¡DP5 CONFIGURATION END¿¿
¡¡DPP STATUS¿¿
Device Type: DP5
Serial Number: 11120
Firmware: 6.06
FPGA: 5.13
Fast Count: 2456482
Slow Count: 2280433
Accumulation Time: 814.394000
Real Time: 816.990000
Dead Time: 7.19%
HV Volt: -112V
TEC Temp: 223K
Board Temp: 44°C

B.4 Gas correction factors of the main pressure sensor

The MKS 903 is the main pressure sensor in the TRIADE setup. It is calibrated on nitrogen. For measurements with other gases, the results must be corrected by dividing through the subsequent gas correction factors. The values are provided by MKS Instruments[2].

Table B.4: Gas correction factors for the MKS 903.

Gas	Symbol	Gas Correction Factor
Acetone	(CH3)2CO	3.60
Air	- - -	1.00
Ammonia	NH3	1.30
Argon	Ar	1.29
Benzene	C6H6	5.90
Bromine	Br2	3.80
Bromomethane	CH3Br	3.70
Carbon Dioxide	CO2	1.42
Carbon Disulfide	CS2	5.00
Carbon Monoxide	CO	1.05
Carbon Tetrachloride	CCl4	6.00
Chlorine	Cl2	0.68
Deuterium	D2	0.35
Helium	He	0.18
Hydrogen	H2	0.46
Hydrogen Bromide	HBr	2.00
Hydrogen Chloride	HCl	1.50
Hydrogen Fluoride	HF	1.40
Isobutylene	C4H8	3.60
Krypton	Kr	1.94
Methane	CH4	1.40
Neon	Ne	0.30
Nitric Oxide	NO	1.30
Nitrogen	N2	1.00
⋮	⋮	⋮

[2]MKS Instruments, 2 Tech Drive, Suite 201, Andover, MA 01810

Appendix C

Statistical methods applied in the evaluation of the tritium adsorption measurements

C.1 Calculation of the arithmetic mean and its statistical uncertainty

This section is based on the *Guide to the expression of Uncertainty in Measurement (GUM)* [08].

The expected value of the quantity q can be estimated from multiple, randomly varying observations with the the arithmetic mean. For n independent observation q_k, the arithmetic mean $\bar{q}$ is:

$$\bar{q} = \frac{1}{n} \sum_{k=1}^{n} q_k. \tag{C.1}$$

Its statistical uncertainty can be estimated based on the experimental variance $s^2(q_k)$ of the individual observations q_k:

$$s^2(q_k) = \frac{1}{n-1} \sum_{j=1}^{n} (q_j - \bar{q})^2 . \tag{C.2}$$

The best estimate of the the variance of the mean value $\bar{q}$ is the experimental standard deviation of the mean $s(\bar{q})$:

$$s^2(\bar{q}) = \frac{s^2(q_k)}{n}. \tag{C.3}$$

For a small number of measurements, a deviation of the arithmetic mean and the expected value occurs. This is taken into account by the Student factor t. For $n = 2$ and a confidence

interval of 1 σ, it is $t = 1.32$. The final estimator for statistical uncertainty of the arithmetic mean is obtained by multiplying the Student factor with $s(\bar{q})$:

$$\Delta\bar{q}_{\text{stat}} = t \cdot s(\bar{q}). \tag{C.4}$$

C.2 Combined uncertainty

This section is based on the *Guide to the expression of Uncertainty in Measurement (GUM)* [08].

Assume measurand Y determined by measuring the values $X_1, X_2, \ldots, X_N$. Then, Y is afflicted by an uncertainty determined by the uncertainty of the values X_i. They are related by the function f:

$$Y = f(X_1, X_2, \ldots, X_N). \tag{C.5}$$

The estimator of Y is denoted y and that of the X_i as x_i. A standard uncertainty $u(x_i)$ is supposed to be known for each x_i. Their combined standard uncertainty $u_c(y)$ is:

$$u_c^2(y) = \sum_{i=1}^{N} \left(\frac{\partial f}{\partial x_i}\right)^2 u^2(x_i). \tag{C.6}$$

C.3 The non-linear curve fit method

The non-linear curve fitting in section 4.4.2.1 is performed with Origin[1] using the χ^2 method. To measure the goodness-of-fit, the coefficient of determination R^2 is calculated. Their subsequent explanations are taken from the Origin handbook.

Basically, any experimental data Y can be described with the model $f(X;\theta)$:

$$Y = f(X, \theta) + \epsilon. \tag{C.7}$$

$X = (x_1, x_2, \ldots, x_k)^T$ are the independent variables of the model. This is the time t in section 4.4.2.1, i.e. $X = t$ and $k = 1$. $\theta = (\theta_1, \theta_2, \ldots, \theta_p)^T$ are the model parameters. ϵ designates the residuals of the fit, i.e. the discrepancy between data Y and model $f(X;\theta)$.

To minimise the discrepancy between data and model, the size χ^2 is minimised:

$$\chi^2 = \sum_{i=1}^{n} \left[\frac{Y_i - f(t_i;\hat{\theta})}{\sigma_i}\right]^2. \tag{C.8}$$

[1] OriginLab Corporation: *OriginPro*, Version 9.1 Sr3, 1991-2014

The sum runs over the whole experimental dataset with entries $i = 1, 2, \ldots, n$. Each entry consists of a value for the time t_i, measured data Y_i and corresponding uncertainty σ_i.

The estimators $\hat{\theta}$ of the model parameters are optimised during the fit. Origin uses the Levenberg-Marquardt algorithm. It combines the methods of Gauss-Newton and the saddle point approximation. The fit converges, when the difference of χ^2 in two subsequent iteration steps falls below a previously defined threshold.

The final χ^2 value can be used to quantify the goodness-of-fit. As χ^2 depends on the size n of the dataset, it needs to be normed to allow for comparison between different datasets. This is done using the degrees of freedom $\mathrm{dof} = n - p$ of the fit, determined by the number of fit parameters p. This returns the reduced $\chi^2 = \bar{\chi}^2$:

$$\bar{\chi}^2 = \frac{\chi^2}{\mathrm{dof}} = \frac{\chi^2}{n - p}. \tag{C.9}$$

Appendix D

Additional results from the investigation of tritium adsorption

Table D.1: Actual measurement time of the BIXS count rates of each run in seconds. measurement inside a 2000 s interval after begin of the evacuation phase only spectra lying fully inside this interval were regarded measurement time 10 s and 100 s change of time resolution cost some time during the measurement interval additional losses from manual mistakes with start of spectrum

run	c1	c2	c3	c4.1	c4.2
0	1000	1740	1730	1610	1698,43
1	1600	1670	1640	1630	1640
2	1610	1670	1640	1640	1630
3	1630	1620	1320	1600	1630
4	1620	1660	1650	1620	1660
5	1650	1670	1630	1649,447	1640
6	1630	1640	1630	220	1615,396
7	1628,889	1660	1630	1590	1659,33
8	1590	1660	1600	1620	1676,413
9	1640	1620,078	1590	1621,005	1662,483
10	1640	1470	1680	1610	1650,342
11	1650	1620	1650	1620	1392,942
12	1630	1660	1630	1610	1815,399
13	1640	1660	1620	1810	
14	1560	1660	1620	1670	
15	1640	1730	220	1580	
16	1600,06				
17	1810				

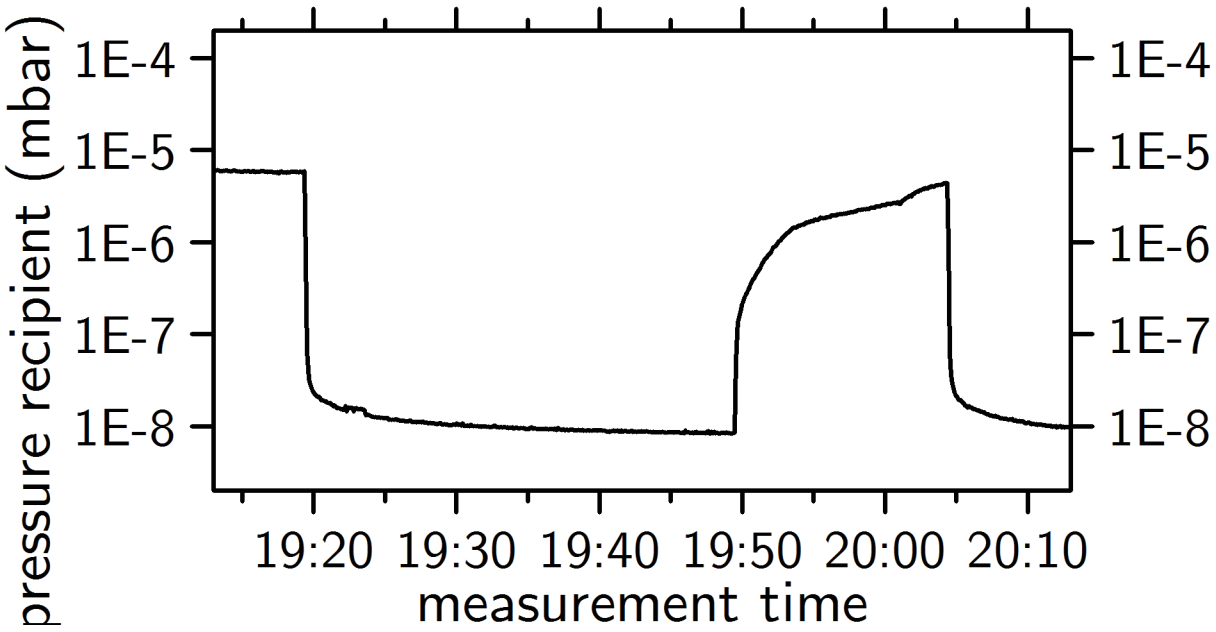

Figure D.1: Pressure rise during closed recipient after campaign c1. The pressure test was performed subsequent to the campaign, see sections 4.1.3 and 4.3.2. The pressure development is caused by adsorption and desorption effects.

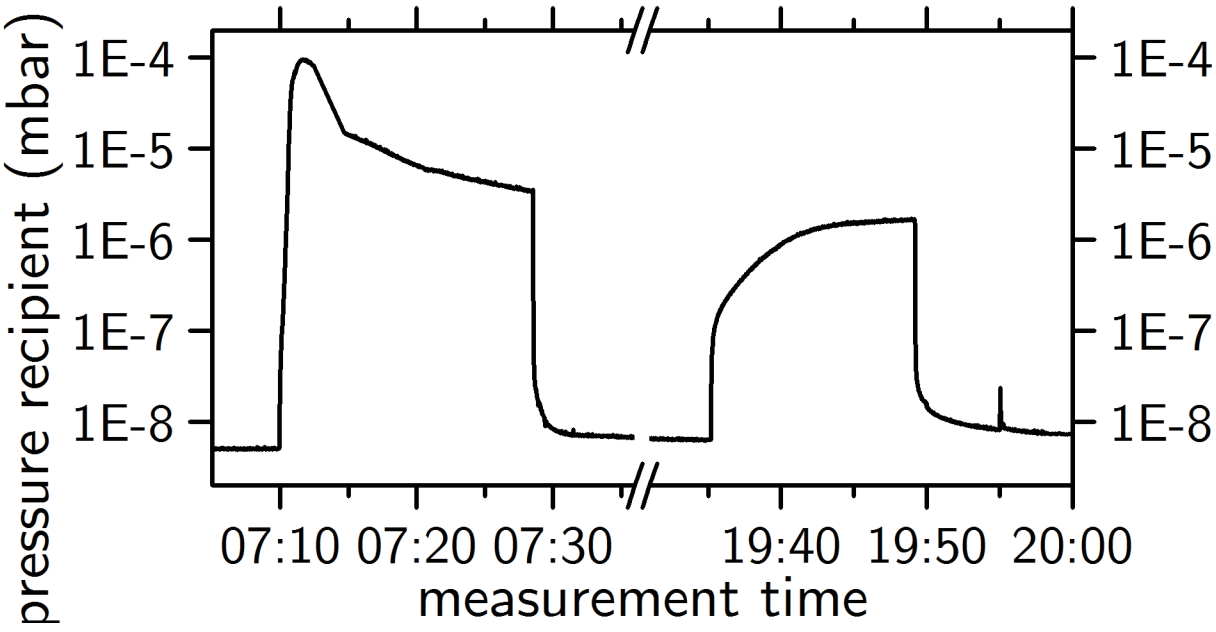

Figure D.2: Pressure rise during closed recipient before and after campaign c2. The pressure tests were performed before and after the campaign, see sections 4.1.3 and 4.3.2. The pressure development is caused by adsorption and desorption effects.

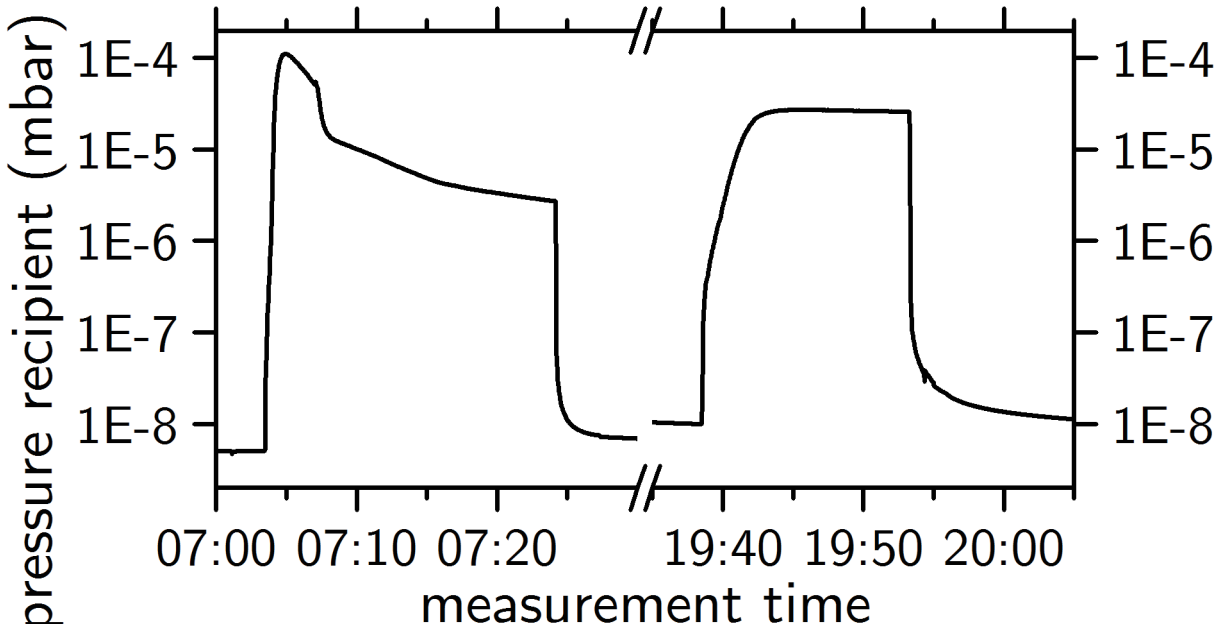

Figure D.3: Pressure rise during closed recipient before and after campaign c3. The pressure tests were performed before and after the campaign, see sections 4.1.3 and 4.3.2. The pressure development is caused by adsorption and desorption effects.

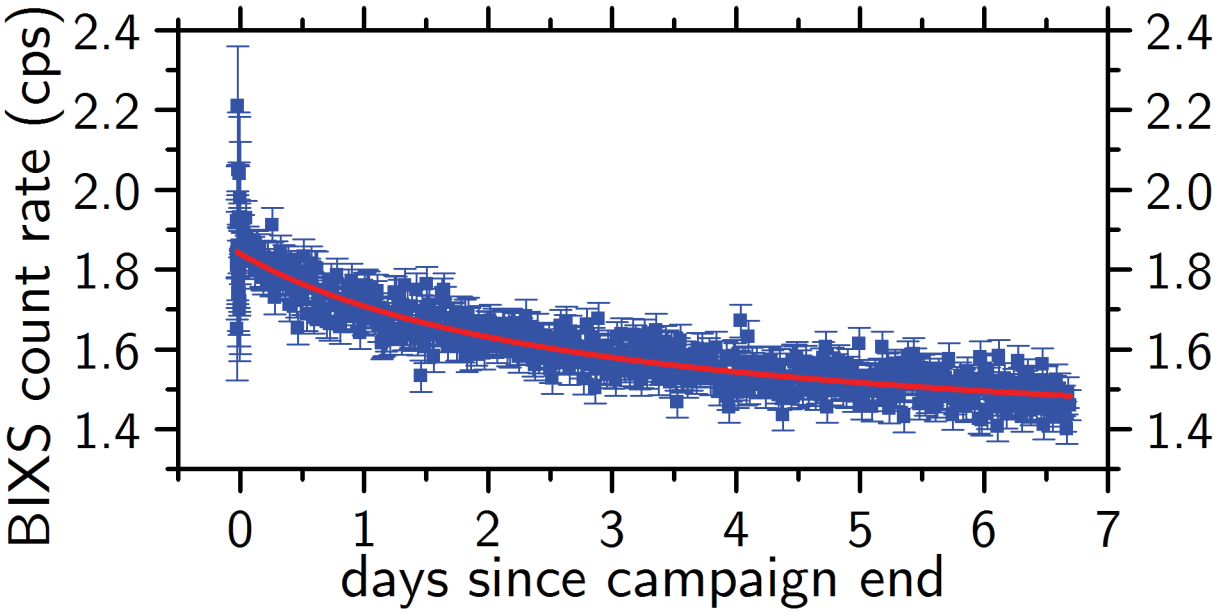

Figure D.4: Fit of the BIXS count rate decreasing under evacuation of the recipient after campaign c1. The count rates (blue squares) are fitted with the model from equation 4.13 (red line). The error bars indicate only statical uncertainty.

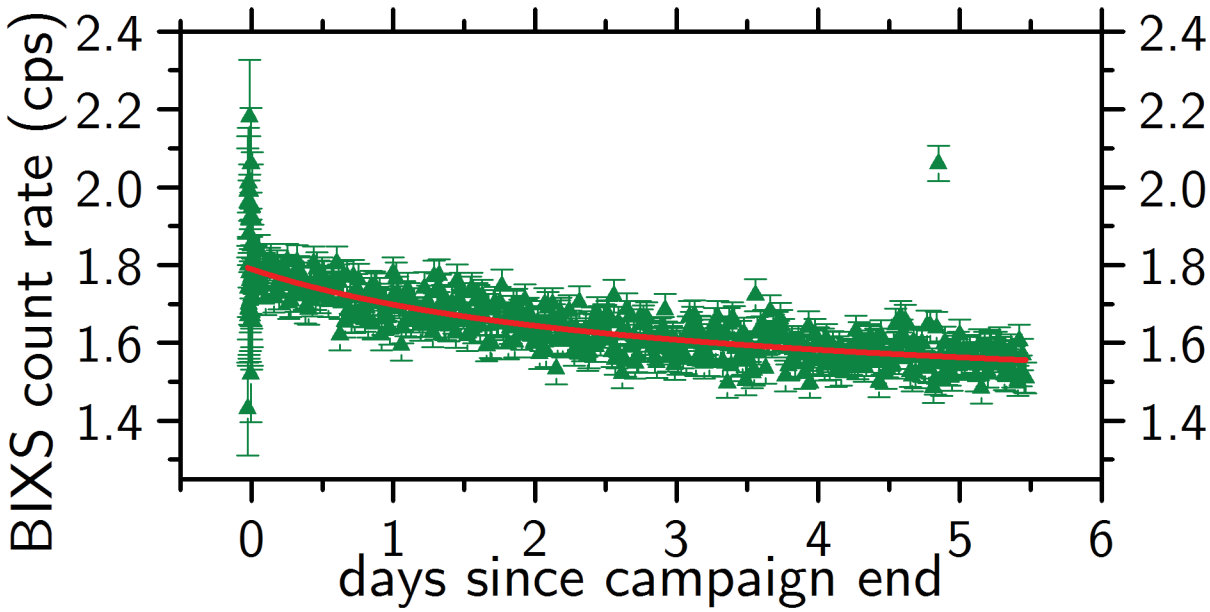

Figure D.5: Fit of the BIXS count rate decreasing under evacuation of the recipient after campaign c2. The count rates (green triangles) are fitted with the model from equation 4.13 (red line). The error bars indicate only statical uncertainty.

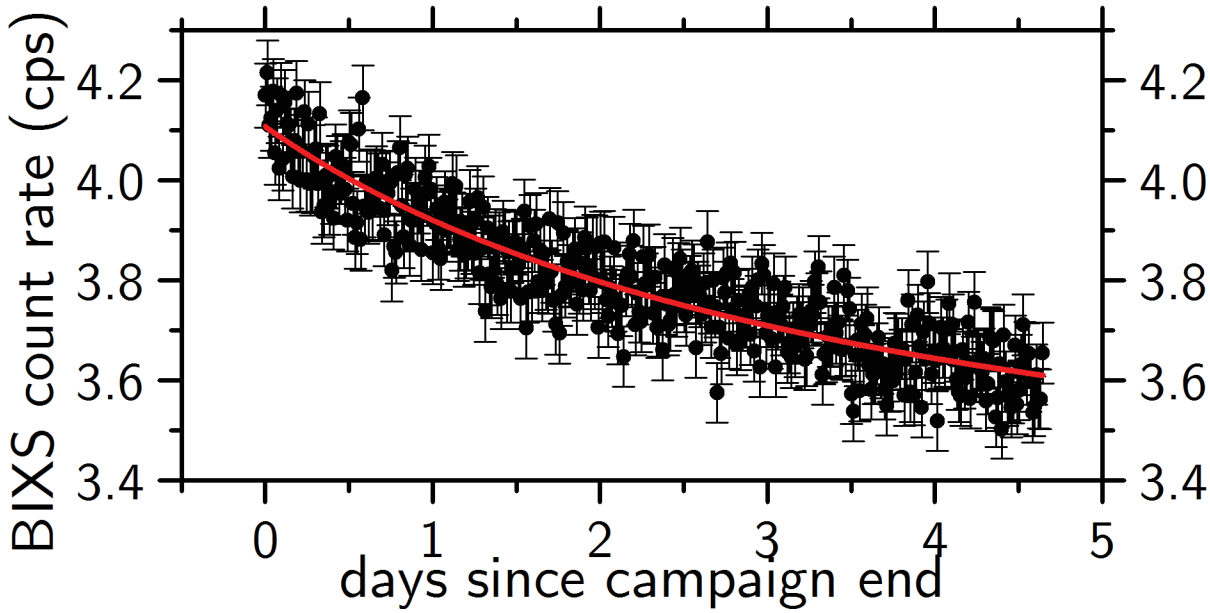

Figure D.6: Fit of the BIXS count rate decreasing under evacuation of the recipient after campaign c3. The count rates (black dots) are fitted with the model from equation 4.13 (red line). The error bars indicate only statical uncertainty.

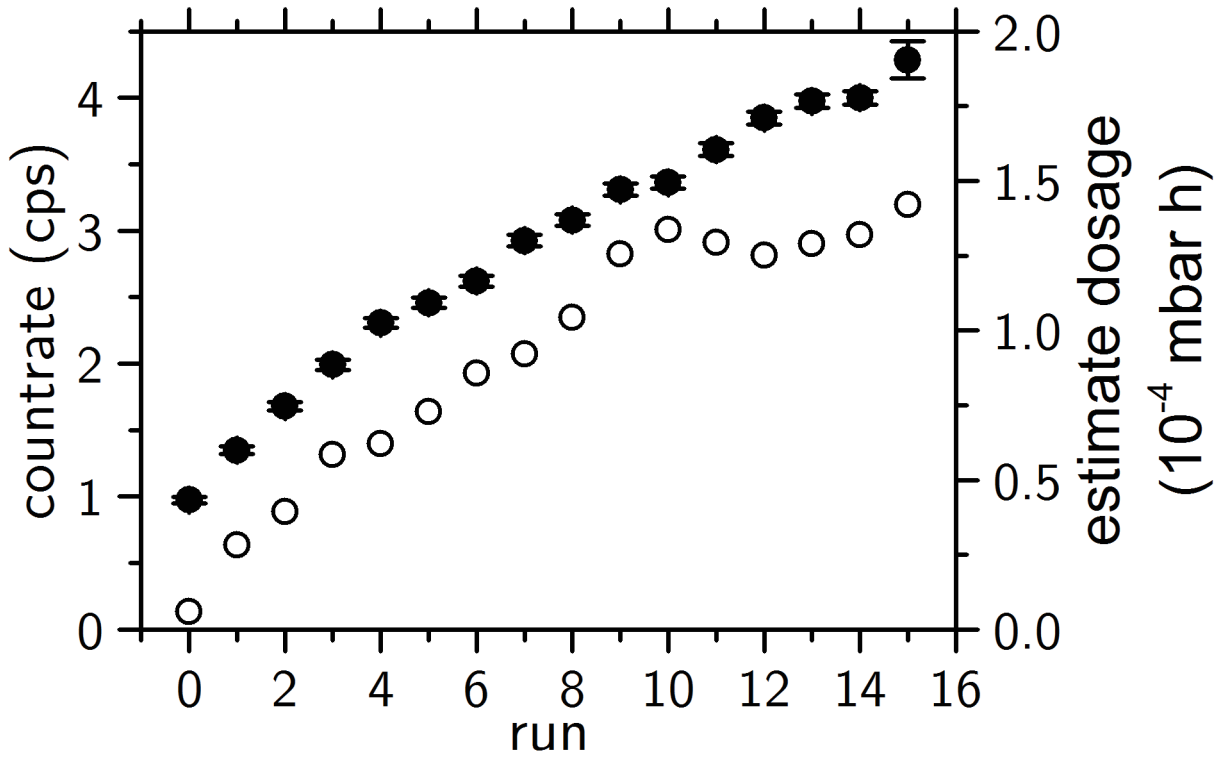

Figure D.7: BIXS count rate development (full dots) of campaign c3 with estimate of the dosage (empty circles). The error bars indicate only statistical uncertainties (see section 4.2.6). Run 0 depicts the BIXS background count rate. The estimate the dosage might deviate by a factor of about 2.5 (see section 4.2.5) from the real value. The dosage and count rate are correlated at the begin of the campaign. However, they are clearly anti correlated in runs 10, 11 and 12.

Appendix E

Measurement protocols: tritium concentration of the tritiated gas

The tritiated gas used in the adsorption measurements was received from the CAPER[1] facility at the TLK. The determination of the tritium concentration was carried out by CAPER. Two measurements were performed each before campaigns c1, c3 and c4. In this order, their protocols are presented in the following. The tritiated gas used for c2 was the same as for c1.

[1] abbreviation: CAPRICE PermCat, with CAPRICE: Catalytic Purification Experiment

MEASUREMENT PROTOCOL FOR TRITIATED GAS ANALYSIS BY CAPER-GC

Measured by:	E.F.		**Sample:**		
	Injection date:	15.07.2014			
	Injection time:	14:07	**BD001 nach Reinigung; IK1+IK2: nA**		
	File Name:	150714,1			
	Injection pressure [mbar]:	29,4			
	Template updated:	01.07.2014			
TCD-A / WLD-A	E.F.	01.07.2008			
Gas	**Retention**	**Area counts**	**Calibration factor**	**Partial pressure**	**Concentration**
	[min]	**[mV·min]**	**[mbar·mV^{-1}·min^{-1}]**	**[mbar]**	**[%]**
CQ_4	1,49	0,000	1,82	0,000	0,000%
CO_2	2,33	0,000	1,88	0,000	0,000%
C_2Q_6	6,39	0,000	1,18	0,000	0,000%
C_3Q_8	16,20	0,000		0,000	0,000%
				$c_{Q,eq}$ [%] (as Q_2 equivalent in C_xQ_y) =	**0,000%**
IC-1 / IK-1	Calibrated on:	01.07.2014			
Gas	**Retention**	**Area counts**	**Partial pressure** (as T_2 equivalent)	**Specific activity** (STP)	**Conc. T equivalent**
	[min]	**[mV·min]**	**[mbar]**	**[Ci·Nm^{-3}]**	**[%]**
CQ4	1,74	0,065	*0,01*	957,855	0,037%
C_2Q_6	6,40	0,000	*0,00*	0,000	0,000%
C_3Q_8	30,73	0,000	*0,00*	0,000	0,000%
Q_2O			*0,00*	0,000	0,000%
Calibration factors	***a*=**	**0**	**$\Sigma A_{sp,Q}$ [Ci·Nm^{-3}] =**	**957,855**	**(STP)**
	***b*=**	**0,15**	**$\Sigma A_{sp,Q}$ [Ci·m^{-3}] =**	**866,063**	**(1bar, 25°C)**
	***c*=**	**0,96**			
				$c_{T,eq}$ [%] (as T_2 equivalent in C_xQ_y and Q_2O) =	**0,037%**
TCD-B / WLD-B	Calibrated on:	15.02.2014			
Gas	**Retention**	**Area counts**	**Calibration factor**	**Partial pressure**	**Concentration**
	[min]	**[mV·min]**	**[mbar·mV^{-1}·min^{-1}]**	**[mbar]**	**[%]**
He-3	2,52	0,000	42,23	0,000	0,000%
H_2	13,46	0,000	106,38	0,000	0,000%
HD	18,08	0,000	23,75	0,000	0,000%
HT	23,03	0,106		Calculated from IC-2 / IK-2	
D_2	26,87	0,000	20,55	0,000	0,000%
DT	31,42	0,082		Calculated from IC-2 / IK-2	
T_2	34,53	1,958		Calculated from IC-2 / IK-2	
IC-2 / IK-2	Calibrated on:	01.07.2014			
Gas	**Retention**	**Area counts**	**Partial pressure**	**Specific activity** (STP)	**Concentration**
	[min]	**[mV·min]**	**[mbar]**	**[Ci·Nm^{-3}]**	**[%]**
HT	23,10	1,841000	1,76	77382,626	5,977%
DT	31,68	2,690000	2,50	109937,545	8,492%
T_2	34,91	70,563000	25,71	2264158,451	87,448%
Calibration factors	***a*=**	**0,49935**	**$\Sigma A_{sp,Q2}$ [Ci·Nm^{-3}]=**	**2451478,622**	**(STP)**
		0,92595	**$\Sigma A_{sp,Q2}$ [Ci·m^{-3}] =**	**2216551,821**	**(1bar, 25°C)**
				$c_{T,Q2}$ [%] (as Q_2) =	**94,682%**
				$c_{Q,Q2}$ [%] (as Q_2) =	**101,917%**
TCD-C / WLD-C	Calibrated on:				
Gas	**Retention**	**Area counts**	**Calibration factor**	**Partial pressure**	**Concentration**
	[min]	**[mV·min]**	**[mbar·mV^{-1}·min^{-1}]**	**[mbar]**	**[%]**
O2	1,89	0,100			
N_2	2,77	0,044	0,44	0,019	0,066%
CO	6,11	0,000	0,54	0,000	0,000%
			$A_{sp,total}$ [Ci·Nm^{-3}] =	**2452436,478**	**(STP)**
			$A_{sp,total}$ [Ci·m^{-3}] =	**2217417,884**	**(1bar, 25°C)**
			$c_{T,total}$ [%] (as C_xQ_y, Q_2O and Q_2) =		**94,719%**

MEASUREMENT PROTOCOL FOR TRITIATED GAS ANALYSIS BY CAPER-GC

Measured by:	E.F.		**Sample:**		
	Injection date:	15.07.2014			
	Injection time:	15:25	**BD001 nach Reinigung; IK1+IK2: nA**		
	File Name:	150714,2			
	Injection pressure [mbar]:	44,9			
	Template updated:	01.07.2014			
TCD-A / WLD-A	E.F.	01.07.2008			
Gas	**Retention**	**Area counts**	**Calibration factor**	**Partial pressure**	**Concentration**
	[min]	**[mV·min]**	**[mbar·mV^{-1}·min^{-1}]**	**[mbar]**	**[%]**
CQ_4	1,49	0,000	1,82	0,000	0,000%
CO_2	2,33	0,000	1,88	0,000	0,000%
C_2Q_6	6,39	0,000	1,18	0,000	0,000%
C_3Q_8	16,20	0,000		0,000	0,000%
				$c_{Q,eq}$ [%] (as Q_2 equivalent in C_xQ_y) =	**0,000%**
IC-1 / IK-1	Calibrated on:	01.07.2014			
Gas	**Retention**	**Area counts**	**Partial pressure** (as T_2 equivalent)	**Specific activity** (STP)	**Conc. T equivalent**
	[min]	**[mV·min]**	**[mbar]**	**[Ci·Nm^{-3}]**	**[%]**
CQ4	1,70	0,096	*0,02*	911,978	0,035%
C_2Q_6	6,40	0,000	*0,00*	0,000	0,000%
C_3Q_8	30,73	0,000	*0,00*	0,000	0,000%
Q_2O			*0,00*	0,000	0,000%
Calibration factors	***a*=**	**0**	**$\Sigma A_{sp,Q}$ [Ci·Nm^{-3}] =**	**911,978**	**(STP)**
	***b*=**	**0,15**	**$\Sigma A_{sp,Q}$ [Ci·m^{-3}] =**	**824,583**	**(1bar, 25°C)**
	***c*=**	**0,96**			
				$c_{T,eq}$ [%] (as T_2 equivalent in C_xQ_y and Q_2O) =	**0,035%**
TCD-B / WLD-B	Calibrated on:	15.02.2014			
Gas	**Retention**	**Area counts**	**Calibration factor**	**Partial pressure**	**Concentration**
	[min]	**[mV·min]**	**[mbar·mV^{-1}·min^{-1}]**	**[mbar]**	**[%]**
He-3	2,52	0,000	42,23	0,000	0,000%
H_2	13,46	0,000	106,38	0,000	0,000%
HD	18,08	0,000	23,75	0,000	0,000%
HT	22,45	0,114		Calculated from IC-2 / IK-2	
D_2	26,87	0,000	20,55	0,000	0,000%
DT	30,65	0,219		Calculated from IC-2 / IK-2	
T_2	33,33	3,524		Calculated from IC-2 / IK-2	
IC-2 / IK-2	Calibrated on:	01.07.2014			
Gas	**Retention**	**Area counts**	**Partial pressure**	**Specific activity** (STP)	**Concentration**
	[min]	**[mV·min]**	**[mbar]**	**[Ci·Nm^{-3}]**	**[%]**
HT	22,71	2,824000	2,61	75300,188	5,817%
DT	30,89	4,111000	3,70	106611,135	8,235%
T_2	33,70	109,882000	38,74	2234157,793	86,289%
Calibration factors	***a*=**	**0,49935**	**$\Sigma A_{sp,Q2}$ [Ci·Nm^{-3}]=**	**2416069,116**	**(STP)**
		0,92595	**$\Sigma A_{sp,Q2}$ [Ci·m^{-3}] =**	**2184535,631**	**(1bar, 25°C)**
				$c_{T,Q2}$ [%] (as Q_2) =	**93,315%**
				$c_{Q,Q2}$ [%] (as Q_2) =	**100,341%**
TCD-C / WLD-C	Calibrated on:				
Gas	**Retention**	**Area counts**	**Calibration factor**	**Partial pressure**	**Concentration**
	[min]	**[mV·min]**	**[mbar·mV^{-1}·min^{-1}]**	**[mbar]**	**[%]**
O2	1,89	0,013			
N_2	2,80	0,064	0,44	0,028	0,063%
CO	6,11	0,000	0,54	0,000	0,000%
			$A_{sp,total}$ [Ci·Nm^{-3}] =	**2416981,094**	**(STP)**
			$A_{sp,total}$ [Ci·m^{-3}] =	**2185360,213**	**(1bar, 25°C)**
			$c_{T,total}$ [%] (as C_xQ_y, Q_2O and Q_2) =		**93,350%**

MEASUREMENT PROTOCOL FOR TRITIATED GAS ANALYSIS BY CAPER-GC

Measured by:	E.F.	**Sample:**	
Injection date:	09.09.2014		
Injection time:	08:53		
File Name:	090914,1	**Gas aus BD001 (ungereinigt); IK1+IK2: nA**	
Injection pressure [mbar]:	11,3		
Template updated:	15.02.2014		

TCD-A / WLD-A E.F. 01.07.2014

Gas	Retention	Area counts	Calibration factor	Partial pressure	Concentration
	[min]	[mV·min]	[mbar·mV^{-1}·min^{-1}]	[mbar]	[%]
CQ_4			1,82	0,000	0,000%
CO_2	3,83	0,009	1,88	0,017	0,150%
C_2Q_6			1,18	0,000	0,000%
C_3Q_8				0,000	0,000%
			$c_{Q,eq}$ [%] (as Q_2 equivalent in C_xQ_y) =		**0,000%**

IC-1 / IK-1 Calibrated on: 01.07.2014

Gas	Retention	Area counts	Partial pressure (as T_2 equivalent)	Specific activity (STP)	Conc. T equivalent
	[min]	[mV·min]	[mbar]	[Ci·Nm^{-3}]	[%]
CQ4	1,75	0,023	*0,00*	1012,547	0,039%
C_2Q_6			*0,00*	0,000	0,000%
C_3Q_8			*0,00*	0,000	0,000%
Q_2O			*0,00*	0,000	0,000%
Calibration factors ***a=***		**0,15977**	**$\Sigma A_{sp,Q}$ [Ci·Nm^{-3}] =**	**1012,547**	**(STP)**
b=		**0,9511**	**$\Sigma A_{sp,Q}$ [Ci·m^{-3}] =**	**915,514**	**(1bar, 25°C)**
			$c_{T,eq}$ [%] (as T_2 equivalent in C_xQ_y and Q_2O) =		**0,039%**

TCD-B / WLD-B Calibrated on: 15.02.2014

Gas	Retention	Area counts	Calibration factor	Partial pressure	Concentration
	[min]	[mV·min]	[mbar·mV^{-1}·min^{-1}]	[mbar]	[%]
He-3	2,55	0,003	42,23	0,127	1,121%
H_2			106,83	0,000	0,000%
HD			23,75	0,000	0,000%
HT				Calculated from IC-2 / IK-2	
D_2	28,13	0,145	20,55	2,980	26,369%
DT				Calculated from IC-2 / IK-2	
T_2	37,44	0,703		Calculated from IC-2 / IK-2	

IC-2 / IK-2 Calibrated on: 01.07.2014

Gas	Retention	Area counts	Partial pressure	Specific activity (STP)	Concentration
	[min]	[mV·min]	[mbar]	[Ci·Nm^{-3}]	[%]
HT	23,60	0,500000	0,53	60220,876	4,652%
DT	33,53	0,884000	0,89	102071,212	7,884%
T_2	37,84	19,012000	7,63	1749047,456	67,553%
Calibration factors ***a=***		**0,49935**	**$\Sigma A_{sp,Q2}$ [Ci·Nm^{-3}]=**	**1911339,544**	**(STP)**
b=		**0,92595**	**$\Sigma A_{sp,Q2}$ [Ci·m^{-3}] =**	**1728174,624**	**(1bar, 25°C)**
			$c_{T,Q2}$ [%] (as Q_2) =		**73,821%**
			$c_{Q,Q2}$ [%] (as Q_2) =		**106,458%**

TCD-C / WLD-C Calibrated on: 15.02.2014

Gas	Retention	Area counts	Calibration factor	Partial pressure	Concentration
	[min]	[mV·min]	[mbar·mV^{-1}·min^{-1}]	[mbar]	[%]
O2	1,90	0,020			
N_2	2,85	0,592	0,44	0,260	2,305%
CO			0,54	0,000	0,000%
			$A_{sp,total}$ [Ci·Nm^{-3}] =	**1912352,091**	**(STP)**
			$A_{sp,total}$ [Ci·m^{-3}] =	**1729090,138**	**(1bar, 25°C)**
			$c_{T,total}$ [%] (as C_xQ_y, Q_2O and Q_2) =		**73,860%**

MEASUREMENT PROTOCOL FOR TRITIATED GAS ANALYSIS BY CAPER-GC

Measured by:	E.F.		**Sample:**		
	Injection date:	09.09.2014			
	Injection time:	11:37			
	File Name:	090914,2	**Gas aus BD001 (ungereinigt); IK1+IK2: nA**		
	Injection pressure [mbar]:	27,5			
	Template updated:	15.02.2014			
TCD-A / WLD-A	E.F.	01.07.2014			
Gas	**Retention**	**Area counts**	**Calibration factor**	**Partial pressure**	**Concentration**
	[min]	**[mV·min]**	**[mbar·mV^{-1}·min^{-1}]**	**[mbar]**	**[%]**
CQ_4	1,68	0,004	1,82	0,007	0,026%
CO_2	3,83	0,015	1,88	0,028	0,103%
C_2Q_6			1,18	0,000	0,000%
C_3Q_8				0,000	0,000%
			$c_{Q,eq}$ [%] (as Q_2 equivalent in C_xQ_y) =		**0,053%**
IC-1 / IK-1	Calibrated on:	01.07.2014			
Gas	**Retention**	**Area counts**	**Partial pressure** (as T_2 equivalent)	**Specific activity** (STP)	**Conc. T equivalent**
	[min]	**[mV·min]**	**[mbar]**	**[Ci·Nm^{-3}]**	**[%]**
CQ4	1,83	0,090	*0,02*	1523,007	0,059%
C_2Q_6			*0,00*	0,000	0,000%
C_3Q_8			*0,00*	0,000	0,000%
Q_2O			*0,00*	0,000	0,000%
Calibration factors	***a*=**	**0,15977**	**$\Sigma A_{sp,Q}$ [Ci·Nm^{-3}] =**	**1523,007**	**(STP)**
	***b*=**	**0,9511**	**$\Sigma A_{sp,Q}$ [Ci·m^{-3}] =**	**1377,056**	**(1bar, 25°C)**
			$c_{T,eq}$ [%] (as T_2 equivalent in C_xQ_y and Q_2O) =		**0,059%**
TCD-B / WLD-B	Calibrated on:	15.02.2014			
Gas	**Retention**	**Area counts**	**Calibration factor**	**Partial pressure**	**Concentration**
	[min]	**[mV·min]**	**[mbar·mV^{-1}·min^{-1}]**	**[mbar]**	**[%]**
He-3	2,55	0,006	42,23	0,253	0,921%
H_2			106,83	0,000	0,000%
HD			23,75	0,000	0,000%
HT	22,74	0,080		Calculated from IC-2 / IK-2	
D_2	27,05	0,200	20,55	4,110	14,945%
DT	31,87	0,179		Calculated from IC-2 / IK-2	
T_2	35,28	1,850		Calculated from IC-2 / IK-2	
IC-2 / IK-2	Calibrated on:	01.07.2014			
Gas	**Retention**	**Area counts**	**Partial pressure**	**Specific activity** (STP)	**Concentration**
	[min]	**[mV·min]**	**[mbar]**	**[Ci·Nm^{-3}]**	**[%]**
HT	23,12	1,213000	1,19	56218,914	4,343%
DT	32,07	2,659000	2,47	116278,519	8,982%
T_2	35,68	54,037000	20,08	1890675,474	73,023%
Calibration factors	***a*=**	**0,49935**	**$\Sigma A_{sp,Q2}$ [Ci·Nm^{-3}]=**	**2063172,907**	**(STP)**
	***b*=**	**0,92595**	**$\Sigma A_{sp,Q2}$ [Ci·m^{-3}] =**	**1865457,697**	**(1bar, 25°C)**
				$c_{T,Q2}$ [%] (as Q_2) =	**79,685%**
				$c_{Q,Q2}$ [%] (as Q_2) =	**101,293%**
TCD-C / WLD-C	Calibrated on:	15.02.2014			
Gas	**Retention**	**Area counts**	**Calibration factor**	**Partial pressure**	**Concentration**
	[min]	**[mV·min]**	**[mbar·mV^{-1}·min^{-1}]**	**[mbar]**	**[%]**
O2	1,89	0,017			
N_2	2,87	0,635	0,44	0,279	1,016%
CO			0,54	0,000	0,000%
			$A_{sp,total}$ [Ci·Nm^{-3}] =	**2064695,914**	**(STP)**
			$A_{sp,total}$ [Ci·m^{-3}] =	**1866834,753**	**(1bar, 25°C)**
			$c_{T,total}$ [%] (as C_xQ_y, Q_2O and Q_2) =		**79,744%**

MEASUREMENT PROTOCOL FOR TRITIATED GAS ANALYSIS BY CAPER-GC

Measured by:	E.F.	**Sample:**	
Injection date:	29.09.2014		
Injection time:	14:02		
File Name:	290914,1	**GM221 Gas aus BD001 nach Reinigung; IK1+IK2: nA**	
Injection pressure [mbar]:	298,9		
Template updated:	15.02.2014		

TCD-A / WLD-A E.F. 01.07.2014

Gas	Retention	Area counts	Calibration factor	Partial pressure	Concentration
	[min]	[mV·min]	[mbar·mV^{-1}·min^{-1}]	[mbar]	[%]
CQ_4			1,82	0,000	0,000%
CO_2			1,88	0,000	0,000%
C_2Q_6			1,18	0,000	0,000%
C_3Q_8				0,000	0,000%
				$c_{Q,eq}$ [%] (as Q_2 equivalent in C_xQ_y) =	**0,000%**

IC-1 / IK-1 Calibrated on: 01.07.2014

Gas	Retention	Area counts	Partial pressure (as T_2 equivalent)	Specific activity (STP)	Conc. T equivalent
	[min]	[mV·min]	[mbar]	[Ci·Nm^{-3}]	[%]
CQ4	1,84	0,897	*0,14*	1248,043	0,048%
C_2Q_6			*0,00*	0,000	0,000%
C_3Q_8			*0,00*	0,000	0,000%
Q_2O			*0,00*	0,000	0,000%
Calibration factors	***a*=**	**0,15977**	$\Sigma A_{sp,Q}$ [Ci·Nm^{-3}] =	**1248,043**	(STP)
	***b*=**	**0,9511**	$\Sigma A_{sp,Q}$ [Ci·m^{-3}] =	1128,442	(1bar, 25°C)
			$c_{T,eq}$ [%] (as T_2 equivalent in C_xQ_y and Q_2O) =		**0,048%**

TCD-B / WLD-B Calibrated on: 15.02.2014

Gas	Retention	Area counts	Calibration factor	Partial pressure	Concentration
	[min]	[mV·min]	[mbar·mV^{-1}·min^{-1}]	[mbar]	[%]
He-3			42,23	0,000	0,000%
H_2			106,83	0,000	0,000%
HD			23,75	0,000	0,000%
HT	19,74	0,703		Calculated from IC-2 / IK-2	
D_2			20,55	0,000	0,000%
DT	24,86	0,945		Calculated from IC-2 / IK-2	
T_2	25,70	26,726		Calculated from IC-2 / IK-2	

IC-2 / IK-2 Calibrated on: 01.07.2014

Gas	Retention	Area counts	Partial pressure	Specific activity (STP)	Concentration
	[min]	[mV·min]	[mbar]	[Ci·Nm^{-3}]	[%]
HT	20,01	18,243000	14,69	63642,965	4,916%
DT	25,20	14,897000	12,18	52755,674	4,075%
T_2	26,24	922,529000	277,86	2406919,587	92,961%
Calibration factors	***a*=**	**0,49935**	$\Sigma A_{sp,Q2}$ [Ci·Nm^{-3}]=	**2523318,226**	(STP)
	***b*=**	**0,92595**	$\Sigma A_{sp,Q2}$ [Ci·m^{-3}] =	2281506,988	(1bar, 25°C)
			$c_{T,Q2}$ [%] (as Q_2) =		**97,457%**
			$c_{Q,Q2}$ [%] (as Q_2) =		**101,953%**

TCD-C / WLD-C Calibrated on: 15.02.2014

Gas	Retention	Area counts	Calibration factor	Partial pressure	Concentration
	[min]	[mV·min]	[mbar·mV^{-1}·min^{-1}]	[mbar]	[%]
O2	2,00	0,041			
N_2	3,46	0,155	0,44	0,068	0,023%
CO			0,54	0,000	0,000%
			$A_{sp,total}$ [Ci·Nm^{-3}] =	**2524566,268**	(STP)
			$A_{sp,total}$ [Ci·m^{-3}] =	2282635,430	(1bar, 25°C)
			$c_{T,total}$ [%] (as C_xQ_y, Q_2O and Q_2) =		**97,505%**

MEASUREMENT PROTOCOL FOR TRITIATED GAS ANALYSIS BY CAPER-GC

Measured by:	E.F.	**Sample:**	
Injection date:	29.09.2014	**GM221 Gas aus BD001 nach Reinigung; IK1+IK2: nA**	
Injection time:	15:46		
File Name:	290914,2		
Injection pressure [mbar]:	138,6		
Template updated:	15.02.2014		

TCD-A / WLD-A E.F. 01.07.2014

Gas	Retention	Area counts	Calibration factor	Partial pressure	Concentration
	[min]	[mV·min]	[mbar·mV^{-1}·min^{-1}]	[mbar]	[%]
CQ_4			1,82	0,000	0,000%
CO_2			1,88	0,000	0,000%
C_2Q_6			1,18	0,000	0,000%
C_3Q_8				0,000	0,000%
				$c_{Q,eq}$ [%] (as Q_2 equivalent in C_xQ_y) =	**0,000%**

IC-1 / IK-1 Calibrated on: 01.07.2014

Gas	Retention	Area counts	Partial pressure (as T_2 equivalent)	Specific activity (STP)	Conc. T equivalent
	[min]	[mV·min]	[mbar]	[Ci·Nm^{-3}]	[%]
CQ4	1,82	0,463	*0,08*	1434,912	0,055%
C_2Q_6			*0,00*	0,000	0,000%
C_3Q_8			*0,00*	0,000	0,000%
Q_2O			*0,00*	0,000	0,000%
Calibration factors ***a=***		**0,15977**	$\Sigma A_{sp,Q}$ [Ci·Nm^{-3}] =	**1434,912**	(STP)
b=		**0,9511**	$\Sigma A_{sp,Q}$ [Ci·m^{-3}] =	1297,403	(1bar, 25°C)
			$c_{T,eq}$ [%] (as T_2 equivalent in C_xQ_y and Q_2O) =		**0,055%**

TCD-B / WLD-B Calibrated on: 15.02.2014

Gas	Retention	Area counts	Calibration factor	Partial pressure	Concentration
	[min]	[mV·min]	[mbar·mV^{-1}·min^{-1}]	[mbar]	[%]
He-3			42,23	0,000	0,000%
H_2			106,83	0,000	0,000%
HD			23,75	0,000	0,000%
HT	20,99	0,341		Calculated from IC-2 / IK-2	
D_2			20,55	0,000	0,000%
DT	27,58	0,464		Calculated from IC-2 / IK-2	
T_2	28,90	11,623		Calculated from IC-2 / IK-2	

IC-2 / IK-2 Calibrated on: 01.07.2014

Gas	Retention	Area counts	Partial pressure	Specific activity (STP)	Concentration
	[min]	[mV·min]	[mbar]	[Ci·Nm^{-3}]	[%]
HT	21,23	8,178000	6,99	65292,996	5,044%
DT	27,83	8,081000	6,91	64575,581	4,988%
T_2	29,39	404,422000	129,48	2418798,370	93,420%
Calibration factors ***a=***		**0,49935**	$\Sigma A_{sp,Q2}$ [Ci·Nm^{-3}]=	**2548666,948**	(STP)
b=		**0,92595**	$\Sigma A_{sp,Q2}$ [Ci·m^{-3}] =	2304426,526	(1bar, 25°C)
			$c_{T,Q2}$ [%] (as Q_2) =		**98,436%**
			$c_{Q,Q2}$ [%] (as Q_2) =		**103,452%**

TCD-C / WLD-C Calibrated on: 15.02.2014

Gas	Retention	Area counts	Calibration factor	Partial pressure	Concentration
	[min]	[mV·min]	[mbar·mV^{-1}·min^{-1}]	[mbar]	[%]
O2	1,97	0,031			
N_2	3,41	0,188	0,44	0,083	0,060%
CO			0,54	0,000	0,000%
			$A_{sp,total}$ [Ci·Nm^{-3}] =	**2550101,860**	(STP)
			$A_{sp,total}$ [Ci·m^{-3}] =	2305723,929	(1bar, 25°C)
			$c_{T,total}$ [%] (as C_xQ_y, Q_2O and Q_2) =		**98,491%**

Bibliography

[08] *Guide to the expression of uncertainty in measurement*. Joint Committee for Guides in Metrology (JCGM), Sept. 2008.

[Ang05] J. Angrik et al.: "KATRIN design report 2004". In *Wissenschaftliche Berichte FZKA 7090* (2005), vol.

[Atk06] P. W. Atkins: *Physikalische Chemie*. 4., vollst. überarb. Aufl. Vol. [Hauptbd.]: Weinheim: Wiley-VCH, 2006.

[Bab12] M. Babutzka, M. Bahr, J. Bonn, B. Bornschein, A. Dieter, G. Drexlin, K. Eitel, et al.: "Monitoring of the operating parameters of the KATRIN Windowless Gaseous Tritium Source". In *New Journal of Physics* (Oct. 2012), vol. 14.

[Bab14] M. Babutzka: "Design and development for the Rearsection of the KATRIN experiment". PhD thesis. Karlsruhe Institute of Technology (KIT), 2014.

[Bar11] G. Barnes and I. Gentle: *Interfacial science : an introduction*. 2. ed. Oxford: Oxford University Press, 2011.

[Ber10] M. Berger, J. Hubbell, S. Seltzer, J. Chang, J. Coursey, R. Sukumar, D. Zucker, et al.: *XCOM: Photon Cross Sections Database, NIST Standard Reference Database 8 (XGAM)*. Radiation Physics Division, Nov. 2010.

[Bro08] I. N. Bronstejn, K. A. Semendjaev, G. Musiol, and H. Mühlig: *Taschenbuch der Mathematik*. 7., vollst. überarb. und erg. Aufl. Frankfurt am Main: Deutsch, 2008.

[Cow98] G. Cowan: *Statistical Data Analysis*. Oxford Science Publications, 1998.

[Dem06] W. Demtröder: *Experimentalphysik 1: Mechanik und Wärme*. Springer Berlin Heidelberg, 2006.

[Dem10] W. Demtröder: *Experimentalphysik 4 : Kern-, Teilchen- und Astrophysik*. Springer-LehrbuchSpringerLink : Bücher. Berlin, Heidelberg: Springer Berlin Heidelberg, 2010.

[Egg04] T. Eggert, O. Boslau, P. Goldstrass, and J. Kemmer: "Silicon drift detectors with enlarged sensitive areas". In *X-ray spectrometry* (Jan. 2004), vol. 33: pp. 246–252.

[Fer12] P. Ferrin, S. Kandoi, A. U. Nilekar, and M. Mavrikakis: "Hydrogen adsorption, absorption and diffusion on and in transition metal surfaces: A DFT study". In*Surface Science* (2012), vol. (606): 679fffdfffdfffd689.

[Foi86] S. M. Foiles, M. I. Baskes, and M. S. Daw: "Embedded-atom-method functions for the fcc metals Cu, Ag, Au, Ni, Pd, Pt, and their alloys". In*Physical Review B* (1986), vol. 3(12): p. 7983.

[Gru08] C. Grupen and B. A. Shwartz: *Particle detectors*. 2. ed. Cambridge monographs on particle physics, nuclear physics, and cosmology ; 26. New York, NY: Cambridge University Press, 2008.

[Hof13] P. Hofmann: *Einführung in die Festkörperphysik*. Lehrbuch Physik. Wiley-VCH, 2013.

[Hol95] G. Hollenberg, E. Simonen, G. Kalinin, and A. Terlain: "Tritium/hydrogen barrier development". In*Fusion Engineering and Design* (Mar. 1995), vol. 28: pp. 190–208.

[Iba06] H. Ibach: *Physics of surfaces and interfaces*. Berlin: Springer, 2006.

[Ich84] K. Ichimura, N. Inoue, K. Watanabe, and T. Takeuchi: "Absorption and desorption of hydrogen, deuterium, and tritium for Zr-V-Fe getter". In*Journal of Vacuum Science & Technology, A: Vacuum, Surfaces, and Films* (1984), vol. 2.

[Jou08] K. Jousten: *Handbook of Vacuum Technology*. Wiley-VCH, 2008.

[Kno10] G. F. Knoll: *Radiation detection and measurement*. 4th ed. Wiley, 2010.

[Kos02] Y. Kosaku, Y. Yanagi, M. Enoeda, and M. Akiba: "Evaluation of Tritium Permeation in Solid Breeder Blanket Cooled by Supercritical Water". In*Fusion Science and Technology* (May 2002), vol. 41(3P2): pp. 958–961.

[Kra23] H. A. Kramers: "XCIII. On the theory of X-ray absorption and of the continuous X-ray spectrum". In*The London, Edinburgh, and Dublin Philosophical Magazine and Journal of Science* (1923), vol. 46(275): pp. 836–871.

[Kri12] H. Krieger: *Grundlagen der Strahlungsphysik und des Strahlenschutzes*. 4. Aufl. 2012. überarb. u. erw. SpringerLink : Bücher. Wiesbaden: Vieweg+Teubner Verlag, 2012.

[Lis87] E. Lisowski, L. Stobinski, and R. Dus: "On the influence of the way of thin gold films preparation on the character of hydrogen adsorption". In*Surface Science* (Oct. 1987), vol. 188(3): pp. L735–L741.

[Lou75] M. R. Louthan, J. A. D. Jr., and J. G. R. Caskey: "Tritium Absorption in Type 304L Stainless Steel". In*Nuclear Technology* (June 1975), vol. 26(2): pp. 192–200.

[Lüt97] H. Lüth: *Surfaces and interfaces of solid materials*. 3. ed., upd. print. Springer study edition. Berlin: Springer, 1997.

[Mat02] M. Matsuyama, T. Murai, and K. Watanabe: "Quantitative Measurement of Surface Tritium by β-Ray-Induced X-Ray Spectrometry (BIXS)". In*Fusion Science and Technology* (May 2002), vol. 41(3P2): pp. 505–509.

[Mat85] M. Matsuyama, K. Ichimura, K. Ashida, K. Watanabe, and H. Sato: "Contamination of Ionization Chamber Due to Tritium Exposure". In*Fusion Science and Technology* (Sept. 1985), vol. 8(2P2): pp. 2461–2466.

[Mat98] M. Matsuyama, K. Watanabe, and K. Hasegawa: "Tritium assay in materials by the bremsstrahlung counting method". In*Fusion Engineering and Design* (Sept. 1998), vol. 39-40: pp. 929–936.

[Mil06] B. Mildner, E. Hasselbrink, and D. Diesing: "Electronic excitations induced by surface reactions of H and D on gold". In*Chemical Physics Letters* (Dec. 2006), vol. 432(1-3): pp. 133–138.

[Nag06] S. Nagy at el.: "On the Q-value of the tritium β-decay". In*EPL (Europhysics Letters)* (May 2006), vol. 74(3): pp. 404–410.

[Nak98] N. Nakashio and M. Nishikawa: "Study on Quantification of the System Effects of Tritium". In*Fusion Science and Technology* (May 1998), vol. 33(3): pp. 287–297.

[Nis06] M. Nishi, T. Yamanishi, T. Hayashi, and D. P. D. Team: "Study on tritium accountancy in fusion DEMO plant at JAERI". In*Fusion Engineering and Design* (745-751 2006), vol. 81(1-7): p. 2006.

[Nis92] M. Nishikawa, T. Takeishi, Y. Kawamura, Y. Takagi, and Y. Matsumoto: "Tritium Mass Balance in the Piping System of a Fusion Reactor". In*Fusion Science and Technology* (Mar. 1992), vol. 21(2P2): pp. 878–882.

[Ott08] E. Otten and C. Weinheimer: "Neutrino mass limit from tritium beta decay". In*Reports on Progress in Physics* (2008), vol. 71(8).

[Pri13] F. Priester and B. Bornschein: "TriToP - A compatibility experiment with turbomolecular pumps under tritium atmosphere". In*14th Joint Vacuum Conference/12th European Vacuum Conference/11th Annual Meeting of the Deutsche Vakuum Gesellschaft/ 19th Croatian-Slovenian Vacuum Meeting, 04-08 June 2012, Dubrovnik, Croatia*. Vol. 98. Dec. 2013: pp. 22–28.

[Roe15a] M. Roellig, S. Ebenhoech, S. Niemes, F. Priester, and M. Sturm: "Development of a compact tritium activity monitor and first tritium measurements". In*in preparation* (2015), vol.

[Roe15b] M. Roellig: "Unpublished PhD thesis". PhD thesis. Karlsruhe Institute of Technology (KIT), 2015.

[Röh76] H. Röhrig, P. Fischer, and R. Hecker: "Tritium Balance in High-Temperature Gas-Cooled Reactors". In*Journal of the American Ceramic Society* (July 1976), vol. 59(7-8): pp. 316–320.

[Röl13] M. Röllig et al.: "Activity monitoring of a gaseous tritium source by beta induced X-ray spectrometry". In*Fusion Engineering and Design* (Dec. 2013), vol. 88(6): pp. 1263–1266.

[Sal06] F. Salvat, J. M. Fernandez-Varea, and J. Sempau: "PENELOPE 2008: A Code System for Monte Carlo Simulation of Electron and Photon Transport". In*Workshop Proceedings* (2006), vol. 4: p. 7.

[Sch13] F. Schneck: "Design and setup of the Tritium Adsorption Desorption Experiment (TRIADE)". MA thesis. Karlsruhe Institute of Technology, 2013.

[Sch91] P. Schira, E. Hutter, G. Jourdan, and R.-D. Penzhorn: "The Tritium Laboratory Karlsruhe: Laboratory design and equipment". In*Fusion Engineering and Design* (Dec. 1991), vol. 18: pp. 19–26.

[Sol07] V. Solea, E. Papillona, M. Cottea, P. Walterb, and J. Susinia: "A multiplatform code for the analysis of energy-dispersive X-ray fluorescence spectra". In*Spectrochimica Acta Part B: Atomic Spectroscopy* (Jan. 2007), vol. 62(1): pp. 63–68.

[Sto92] L. Stobinski: "Atomic hydrogen adsorption on thin gold films". In*Surface Science* (May 1992), vol. 269-270: pp. 383–388.

[Sto94] L. Stobinski and R. Dus: "Model of atomic hydrogen adsorption on thin gold film surface". In*Vacuum* (Feb. 1994), vol. 45(2-3): pp. 299–301.

[Sto96] L. Stobinski: "Molecular and atomic deuterium chemisorption on thin gold films at 78 K: an isotope effect". In*Applied Surface Science* (Dec. 1996), vol. 103(4): pp. 503–508.

[Wes60] T. Westermark, L. Devell, and N. Ghanem: "On the use of bremsstrahlung for the determination of tritium in aqueous and organic systems". In*Nuclear Instruments and Methods* (Nov. 1960), vol. 9(2): pp. 141–144.

[Zan88] A. Zangwill: *Physics at surfaces*. 1. publ. Cambridge: Cambridge Univ. Pr., 1988.

[Zhe12] X. B. Zheng, M. Matsuyama, Y. R. Niu, Y. Zeng, H. Ji, and L. P. Huang: "Tritium Adsorption on Tungsten and Boron Carbide Coatings Deposited by Vacuum Plasma Spraying". In*Fusion Science and Technology* (July 2012), vol. 62(1): pp. 46–49.

Erklärung

Hiermit versichere ich, die vorliegende Arbeit selbstständig verfasst zu haben. Ich habe keine anderen als die angegebenen Quellen und Hilfsmittel benutzt. Wörtlich oder inhaltlich übernommene Stellen habe ich durch einen Verweis kenntlich gemacht. Die Satzung der Universität Karlsruhe zur Sicherung guter wissenschaftlicher Praxis habe ich beachtet.

Manuel Klein
Karlsruhe, den 31. März 2015